The Impact of Pathological Ventilation on Aerosol Deposition: Imaging, Insight and Intervention

by

Elliot Greenblatt
M.S. Mechanical Engineering, Columbia University 2009
B.S. Mechanical Engineering, Columbia University 2007
B.A., Physics, Queens College 2007

Submitted to the Department of Mechanical Engineering
in partial fulfillment of the requirements for the degree of
Doctor of Philosophy in Mechanical Engineering at the
Massachusetts Institute of Technology
February 2015

Signature of Author: _____

Department of Mechanical Engineering
December 15, 2014

Certified by: _____

Jose Venegas
Associate Professor of Anesthesia (MGH-HMS), Thesis Supervisor

Certified by: _____

Roger Kamm
Professor of Biological and Mechanical Engineering, Internal Thesis Supervisor

Accepted by:_____

David Hardt
Professor of Mechanical Engineering, Chairman, Committee for Graduate Students

-blank-

for my loves,

and for my losses.

Table of Contents

The Impact of Pathological Ventilation on Aerosol Deposition: Imaging, Insight and Intervention

by
Elliot Greenblatt

Submitted to the Department of Mechanical Engineering
in partial fulfillment of the requirements for the degree of
Doctor of Philosophy in Mechanical Engineering at the
Massachusetts Institute of Technology
on December 15th 2014

Abstract

Aerosol therapies are often used to treat lung diseases in which ventilation is distributed heterogeneously throughout the lung. As therapeutic aerosols are transported by the inhaled air, it is likely that deposition is diminished within poorly ventilated regions of the lung. These regions are often the most in need of therapy.

We measured the effects of heterogeneous ventilation on aerosol deposition in a group of bronchoconstricted asthmatic subjects. We then developed a new image processing technique which allowed us to identify the anatomical location of aerosol deposition. This technique accounted for blurring due to limited resolution of the PET image, motion artifacts due to breathing, and registration uncertainty.

We introduced a theoretical framework to characterize four mechanisms of variability in deposition between peripheral regions of the lung. This framework added insight into the interaction between ventilation and deposition, and will permit the future comparison of the experimental data with computational models. Together, the imaging data and theoretical framework suggested that more than a third of the observed variability in the deposition per unit volume among lung lobes was due to heterogeneous ventilation.

Using helium-oxygen as a carrier gas for aerosol has been considered as a potential intervention to homogenize deposition in the lung periphery. To investigate this, we repeated the PET-CT measurements in a second group of bronchoconstricted asthmatic subjects breathing helium-oxygen, and compared the results to those of the group breathing room air. We did not find systematic differences in the deposition patterns of the two groups, although the relationship

between ventilation and aerosol deposition tended to be stronger in the group that used helium-oxygen as the carrier gas.

Finally, we used analytical tools and an in-silico model of bronchoconstriction to illustrate the emergence of pendelluft gas transport between parallel regions of the lung. We found that though pendelluft may emerge in asthma, the overall volume passed between parallel regions of the lung is likely less than 2% of the tidal volume, and thus is not likely to substantially influence aerosol deposition.

Thesis Committee:

Jose Venegas (Thesis Advisor), MGH-HMS Department of Anesthesia

Roger Kamm (Chair), MIT MechE

Alexander Slocum, MIT MechE

Scott Harris, MGH-HMS Department of Medicine

Tilo Winkler, MGH-HMS Department of Anesthesia

Acknowledgements

Dearest reader, colleague, teacher, friend, or critic, before we begin, I would very much like to express that the present work is a labor of great care and immense love. However, only a small fraction of this care and love arrive at this thesis from endogenous sources; most of it was sourced from people who have guided me, argued with me, provided for me, nursed my wounds, and engaged in mental wrestling long after they had already tired. This work is built on and of other peoples love, insight, care and patience.

My advisor, Jose Gabriel Venegas Torres has taught me the ins and outs of science, and the wonders of the logarithm. He has tolerated my eternal irreverence, and I hope the intensity of our process (which strongly resembles a murder trial taking place in nitroglycerine loaded pressure cooker) has yielded a precious stone or two, harder and more enduring because of the heat we were able to face together.

I have learned so much from my teacher, guru, friend, and sparring partner, Tilo Winkler. With endless compassion, and more strangely, time, Tilo has guided me, argued with me, drank coffee with me, and married me off. Though I will never admit it, he has convinced me of the middle path, of the balanced argument, and the virtue of being at the center of the wheel.

Robert Scott Harris, in the immensity of his consciousness, has forgiven my delinquency far more times that is reasonable (or even safe). He has provided funds, time, resources, and the occasional cocktail to my continued survival and existence. Vanessa Jane Kelly has taught me what great friends can be, and has provided careful (but in no way softened) advice regarding most of this manuscript. Together with the other folks at the Pulmonary Imaging and Bioengineering Laboratory at MGH, we have built a real sense of camaraderie, community and cookies. Ira Katz has been a champion of great science from within the ranks of Air Liquide, and in addition to his scientific guidance, has helped obtain some of the immense funding that made this thesis possible.

Roger Dale Kamm, out of kindness and his friendship with Jose, has put his illustrious neck out on the line to provide me with guidance and support from within MIT. Alexander Slocum, one of the main reasons that I came to MIT, has gracefully accepted the nuisance of serving on my thesis committee, and I am grateful for this.

Over the last 33 years I have been granted great freedom to pursuit a rich set of interests and ideas. This work is the culmination of those pursuits. Without the support of my family, and without the heart and spit that they imbued in me, I would neither have had these opportunities, nor had the courage to seize them. I am thankful for the Jim Joseph Family Trust, whose support greatly reduced the quantity of ramen noodles that I would have otherwise had to consume.

Above all others, I would like to thank my partner and accomplice in life, liberty and the pursuit of happiness, Shirley Marie Immacula Poyau. There are no words to describe her support, patience and care. So let the remaining 39,000 or so words of this thesis stand as a testament of her undying love. With this said, let us begin.

Introduction

Overview

During an asthma exacerbation, some airways constrict while others dilate leading to differences in ventilation throughout the lung [1, 2]. Asthma exacerbations are often treated with inhaled bronchodilators. What is the terminal destination within the lung of such treatments? This question leads to the aim of Chapter I in this thesis: **to measure the pattern of heterogeneous deposition and ventilation in asthma using PET-CT.**

Variability in peripheral aerosol deposition among lobes, sublobes, or any set of peripheral lung regions, can be traced to four distinct factors: 1) differences in regional ventilation, 2) differences in how the aerosol and air distribute between branches in the series of bifurcations along the pathway feeding the region 3) variability in the amount of the aerosol that escapes the series of airways along that pathway, and 4) variability in the amount of aerosol that reaches the periphery and is not exhaled. The aim of the second chapter of this thesis is **to understand the sources of heterogeneous aerosol deposition in bronchoconstricted asthmatic subjects**

During severe bronchoconstriction bronchodilators are sometimes administered in a mixture of 80% helium and 20% oxygen (He-O_2) in an effort reduce the resistance in the central airways and improve delivery of the aerosol to the lung periphery [3-6]. Does He-O_2 lead to a more homogeneous deposition in bronchoconstricted asthmatics? Answering this is the objective of the third chapter of this thesis: **to determine if He-O_2 homogenizes the deposition in bronchoconstricted asthmatics.**

The heterogeneous mechanical properties or different regions of the lung in asthma could lead to air and aerosol being passed back and forth between regions of the lung in a process known as pendelluft. The final chapter of this thesis uses analytical tools and a numerical model of the bronchoconstricted lung **to access whether or not significant pendelluft airflows emerge in asthma.**

Each of these four aims is explored in more detail below. Each chapter in this thesis has been prepared for independent publication, and each follow the traditional scientific paper format. Chapters 1 and 4 have already been published[7, 8], and the other two chapters have been submitted for publication at the time of submission of this thesis. A final chapter synthesizes summarizes the key findings and contributions of this thesis.

Aim 1: To image aerosol deposition in asthma using PET-CT

While many factors affect total and regional deposition, the underlying disease process in the lung is a major determinant of the final deposition pattern [9]. Many diseased lungs have heterogeneous ventilation which may contribute to heterogeneous deposition. It has been shown that aerosol bolus dispersion and recovery (measured at the mouth) are both influenced by heterogeneous ventilation [10]. While it is likely that the heterogeneous ventilation contributes to heterogeneous deposition, other features of the pathology also modulate the deposition pattern. For example, during bronchoconstriction the fraction of inhaled particles that pass the narrowed airways and reach the periphery distal to the narrowed airways is reduced [11, 12].

The relationship between regional ventilation and deposition depends on the state of health of the lung. Given the convective nature of aerosol transport, in health the distribution of small particles follows the distribution of ventilation throughout the lung. In fact, experimental and clinical methods of assessing regional ventilation distribution measure the distribution of inhaled 1μm microspheres [13]. This is supported by a recent numerical simulation of particle transport in an airway model of the human lung taken from CT [14]. This simulation found that (when air was the carrier gas) the peripheral deposition distribution of 2.5μm particles was strongly correlated with regional ventilation. However, in diseased lungs the presence of constricted airways and airway obstructions can be expected to interfere with the relationship between ventilation and deposition; while narrowed airways might both collect aerosol deposition (limiting distal deposition) and interfere with the subtended ventilation, these two effects do not necessarily happen in proportion to each other. Indeed, no relationship between ventilation and deposition was found in 10 subjects with HIV infections using a 2D gamma-scintigraphy [15].

In some pathologies a *negative* relationship between ventilation and deposition within the airways has been measured [16]. This may happen when an obstruction in an airway (such as in cystic fibrosis) both collects aerosol particles and interferes with the ventilation of subtended regions of the lung. Other factors such as a longer settling time in poorly ventilated regions can lead to paradoxical increases in deposition [17]; within these regions suspended particles may have more time to sediment than in well ventilated regions. All in all, the degree to which ventilation guides deposition during pathological breathing is not presently certain.

As part of the work presented in this thesis, we imaged subjects at MGH to evaluate the extent to which the deposition of aerosols is related to the heterogeneous ventilation of bronchoconstricted asthmatics. 14 asthmatic subjects were imaged with PET-CT in the supine

position. High resolution computed tomography [HRCT] images of the chest anatomy were obtained at total lung capacity [TLC] and after induced bronchoconstriction at mean lung volume [MLV]. Deposition of aerosol was imaged with dynamic PET during and after the inhalation of ~4.5μm $^{13}NH_3$ labeled saline aerosol. Regional ventilation was then imaged using a bolus injection of ^{13}NN tracer in saline solution (the tracer is transported by the pulmonary blood flow to the capillary where it diffuses into the alveoli and ventilation is estimated from the subsequent washout of the tracer).

This wealth of information provides us with a unique 4D perspective on aerosol deposition. It allows us to distinguish deposition between different lobes of the lung, and to evaluate the deposition inside of the central airways visible with CT. However, an anatomical description of aerosol deposition requires synthesis of the CT and PET images. This analysis is fraught with challenges, these include:

1) PET and CT images are acquired at different resolutions. The limited resolution of PET results in PET voxels that contain information influenced by multiple regions of interest [ROIs] (e.g. central airways and the parenchyma).
2) The images, although acquired by the same camera, are taken at different times. Occasionally, the subject position may change between the images, or may be in a different lung volume during the deposition image than either of the CT images.
3) The CT images are taken during a breath hold, whereas the PET deposition image is taken during breathing. This leads to motion artifacts in the image that need to be considered.

In addition, there are open questions and possibilities that emerge when using PET-CT for deposition:

4) Different degrees of the airtree can be segmented from different subjects. How do we choose an airway ROI that will allow us to compare deposition across subjects?
5) While the CT image at TLC can resolve more of the airways, the deposition images are taken at a volume closer to MLV. How can we use the improved information of the TLC image to interpret the deposition image?
6) Can we characterize the deposition in pharmacologically relevant terms, such as the deposition per unit area of airway surface, or the deposition per gram of parenchymal tissue?

=Over the past years I have worked to address several of these questions. These original contributions are the topic of the first chapter in this PhD thesis. With these methods we were able to determine the deposition within each of the five lung lobes and the stratification of deposition within each of the lobes.

Aim 2: To understand the sources of heterogeneous aerosol deposition in bronchoconstricted asthmatic subjects

The success of an inhaled therapy depends upon its location and concentration in the respiratory tract; regional deposition needs to be known to predict therapeutic effectiveness [18, 19]. The PET-CT measurements describe in Chapter I showed that deposition of inhaled aerosol in bronchoconstricted asthmatic subjects is heterogeneous. The pattern of deposition that we observed included both serial differences in the fraction of aerosol retained by the central airways feeding each lobe as well as parallel differences in the aerosol that reached beyond these airways[7]. In the present chapter we seek to understand how serial differences in airway retention couple with other factors to achieve the parallel heterogeneity in deposition of aerosol among lobes.

We postulate that the variability in peripheral aerosol deposition among lobes, sublobes, or any set of peripheral lung regions, can be traced to four distinct factors: 1) differences in regional ventilation, 2) differences in how the aerosol and air distribute between branches in the series of bifurcations along the pathway feeding the region 3) variability in the amount of the aerosol that escapes the series of airways along that pathway, and 4) variability in the amount of aerosol that reaches the periphery and is not exhaled.

In Chapter II we integrate these four factors into a theoretical framework that describes the processes of transport and deposition of an inhaled aerosol along the airway tree to the periphery. Using this framework we evaluate the influence of each factor based on PET-CT imaging data of lung anatomy, aerosol deposition, and ventilation in bronchoconstricted asthmatic subjects. The framework presented in this chapter provides lobar indices of the sources of variability that can be used to validate the clinical applicability of patient specific numerical models of aerosol deposition.

Aim 3: To explore the benefits of using He-O_2 to deliver therapy in bronchoconstricted asthmatics.

Changing the carrier gas from air to He-O_2 results in higher overall deposition [20, 21], is more likely to deposit in the lung periphery [12, 22], and reduces the central deposition due to bronchoconstriction [12]. Most studies point to the lower Reynolds number of He-O_2 ($Re_{air}/Re_{He\text{-}O2}$ = 2.9) as a likely cause. The lower Re leads to less turbulent flow and more readily develops a steady

flow profile after each bifurcation [20, 23]. This should carry the aerosol front deeper into pulmonary alveolar spaces and produces a larger interface between tidal and reserve air leading to greater deposition [20].

An important factor in determining aerosol impaction is the Stokes number [Stk] [24]. Particles with small (Stk «1) follow streamlines, while particles with large Stk (≥1) do not follow rapid changes in streamline direction [14]. However, despite the 3 times higher drag force that the He-0_2 exerts on an aerosol particle compared to air, both gasses have nearly identical Stokes numbers during physiological breathing in the lung; the inertia of the He-O_2 gas around the particle is small and easily overwhelmed by viscous forces leading to greater drag on the particle, at the same time the inertia of the particle overwhelms the inertia of the He-O_2 causing the terms to cancel. Other studies have used combinations of the Stokes and Reynolds numbers to organize deposition in the lung (e.g. [25]), and these could indicate differences in the expected deposition between air and He-O_2.

Where the laminar profiles may help the aerosol move deeper into the lung and even past bronchoconstricted airways, the laminar flows expected in He-O_2 may also inhibit mixing of the aerosol across the cross section of the airways. A recent CFD study [14] concluded that in laminar flow the distribution of 2.5-μm particles in the central airways depends on the particle release location at the mouthpiece inlet, whereas in the turbulent flow the particles are well mixed before reaching the first bifurcation and their distribution is strongly correlated with regional ventilation.

We sought to measure these effects of He-O_2 using PET-CT and to better understand how it can influence both deposition and the ventilation-deposition relationship during bronchoconstriction. In a second arm to the previously mentioned ventilation-deposition study at MGH, we repeated the method in 10 additional asthmatics. This time we provided them He-O_2 after the induced bronchoconstriction and continued to provide the gas during aerosol inhalation and during the ventilation PET scan. We wondered if this would lead to more homogeneous deposition by allowing aerosols to pass beyond the constricted airways. Or might it cause more heterogeneous deposition because of the reduced turbulent mixing?

Using the same techniques to analyze the image as in the room air arm of the study we seek to identify whether or not there is a marked difference in the deposition while breathing He-O_2. Is it more uniform between lobes? Is the stratification within lobes more even? Is the deposition more peripheral? And is the relationship between deposition and ventilation changed while breathing He-O_2? These questions are answered in Chapter III.

Aim 4: To understand the emergence of pendelluft airflows in asthma

Inspiratory and expiratory airflows in healthy lungs are relatively uniform throughout the bronchial tree. However, in pulmonary diseases or under abnormal conditions, this uniform pattern can be disturbed; inhomogeneous inflation or deflation of the lungs can cause dynamic pressure differences between different regions which in turn lead to interregional airflows. This effect is referred to as pendelluft ('Swinging Air') because gas is passed back and forth between the different regions of the lungs. When pendelluft is present, it can modify aerosol deposition in the diseased lung. We asked, does pendelluft emerge in the asthmatic lung?

Chapter IV has two distinct aims that are mutually supportive. First, to clarify the definition, causes, and magnitude of pendelluft. To this end, we use analytical tools to define a generalized quantitative definition of pendelluft, identify its limits, and evaluate its magnitude using analytical methods. We then extend this definition to include pendelluft throughout a bronchial tree. The second aim of the chapter is to provide an example of local and regional effects of pendelluft on airflow and ventilation in a realistic context using an in-silico model of bronchoconstriction. We then use the numerical simulation to explore the frequency dependence of global pendelluft volume and the conditions for which the inertance inertia of the airways becomes important.

Chapter I: Analysis of Three Dimensional Aerosol Deposition in Pharmacologically Relevant Terms: Beyond Black or White ROIs

Elliot Eliyahu Greenblatt[1,2]*, Tilo Winkler PhD[2], Robert Scott Harris MD[2], Vanessa Jane Kelly PhD [2], Mamary Kone MD[2], Jose Venegas PhD [2]

[1]Massachusetts Institute of Technology, BOSTON, MA, USA

[2]Massachusetts General Hospital and Harvard Medical School, BOSTON, MA, USA

This chapter has been published in the Journal of Aerosol Medicine and Pulmonary Drug Delivery[7], and the text and figures are reproduced here with the permission of the publisher.

Abstract

Background: This chapter presents a novel methodological approach to evaluate images of aerosol deposition taken with PET-CT cameras. Traditionally, Black-or-White [BW] Regions of Interest [ROIs] are created to cover Anatomical Regions [ARs] segmented from the high-resolution CT. Such ROIs don't usually consider blurring effects due to limited spatial resolution or breathing motion, and do not consider uncertainty in the AR position within the PET image. The new methodology presented here [Grayscale] addresses these issues, allows estimates of aerosol deposition within ARs, and expresses the deposition in terms of Tissue Dosing (in the lung periphery) and Inner Surface Concentration (in the larger airways).

Methods: Imaging data included a PET deposition image acquired during breathing and two CT scans acquired during breath holds at different lung volumes. The lungs were segmented into anatomically consistent ARs to allow unbiased comparisons across subjects and across lobes. The Grayscale method involves defining Voxel Influence Matrices [VIMs] to consider how average activity within each AR influences the measured activity within each voxel. The BW and Grayscale methods were used to analyze aerosol deposition in 14 bronchoconstricted asthmatics.

Results: Grayscale resulted in a closer description of the PET image than BW ($P<0.0001$) and exposed a seven-fold underestimation in measures of specific deposition. The average Tissue Dosing was 2.11×10^{-6} Total Lung Dose/mg. The average Inner Surface Concentration was 45×10^{-6} Total Lung Dose/mm^2, with the left lower lobe having a lower ISC than lobes of the right lung ($P<0.05$). There was a strong lobar heterogeneity in these measures (COV = 0.3).

Conclusion: The Grayscale approach is an improvement over the BW approach and provides a closer description of the PET image. It can be used to characterize heterogeneous concentrations throughout the lung and may be important in translational research and in the evaluation of aerosol delivery systems.

Keywords: PET-CT, ROIs, partial volume effect, spillover effect, motion correction, tissue dosing, surface concentration, mucocilliary transport, heterogeneity

Nomenclature

AR: An **A**natomical **R**egion is the physical volume of interest independently of how it shows up in any of the imaging modalities.

BINT: Bronchus **Int**ermedius AR.

BW: Black or White method for interpreting regional information in image using binary ROIs.

COV: The **C**oefficient **O**f **V**ariation is the standard deviation normalized by the mean of a distribution.

D : The aerosol deposition image with units of specific deposition.

FEV_1: The Forced Expiratory Volume in 1 second for a given subject in an effort from TLC.

FWHM: Full **W**idth **H**alf **M**aximum of a distribution is a measure of a distribution. For a Gaussian distribution FWHM is 2.4 times the standard deviation.

Grayscale: A method of interpreting regional information in an image using VIMs with values that range from zero to one.

HRCT, CT: High **R**esolution **C**omputed **T**omography images use X-rays to create clear pictures of the anatomy with a typical resolution of 0.3mm**.**

ISC: The **I**nner **S**urface **C**oncentration is the dose delivered to an airway per unit surface area.

LUL, LLL, RUL, RML, RLL: **L**eft **U**pper **L**obe, **L**eft **L**ower **L**obe, **R**ight **U**pper **L**obe, **R**ight **M**iddle **L**obe, and **R**ight **L**ower **L**obe respectively.

LUL CA, LLL CA, RUL CA, RML CA, RLL CA: The **C**entral **A**irways of each lobe defined as the lobar through subsegmental airways.

MLV: Mean **L**ung **V**olume is the average volume during tidal breathing.

MMAD: Mass **M**edian **A**erodynamic **D**iameter is a measure of the median aerosol diameter.

^{13}N-NH3: Ammonia labeled with radioactive nitrogen with a half-life of 10 minutes used in this study to follow nebulized aerosols.

PC_{20}: The dose of Methacholine that results in a 20% reduction in FEV_1 in a given subject.

PI: The **P**enetration **I**ndex is the periphery-to-airway ratio of specific deposition.

PET: Positron **E**mission **T**omography follows radiolabeled tracers in the body with a typical resolution of 6.0mm.

PET-CT, SPECT-CT: Imaging device that can sequentially take both HRCT and PET or SPECT images without repositioning the subject on the gantry.

ROI: A **R**egion **O**f **I**nterest is a subset of voxels within an image that cover an AR used in Black or White analysis of radiolabeled images.

RMB, LMB: Right and **L**eft **M**ain **B**ronchus ARs.

Specific Deposition: The deposition within a region normalized by its volume.

$R_i, \Re$: The ith AR's three dimensional VIM, and a 2D matrix with all VIMs arranged in column vectors;

SPECT: Single-**P**hoton **E**mission **C**omputed **T**omography follows radiolabeled tracers within the body with a typical resolution of 15mm.

TD: The **T**issue **D**osing is the dose delivered to a region normalized by the local tissue volume.

TLC: Total Lung Capacity is the maximal volume of the lung.

TLD: The **T**otal **L**ung **D**ose is the cumulative deposition in all lobes and lobar central airways.

TRC: The **Tr**a**c**hea AR.

VIM: A **V**oxel **I**nfluence **M**atrix considers how average activity within each AR influences the measured activity within each voxel in a radiolabeled image. VIMs are used in the Grayscale approach.

VMD: Volume **M**edian **D**iameter.

GSD: Geometric **S**tandard **D**eviation.

X **:** A vector of each AR's specific deposition.

Introduction

Estimation of local dosing in terms of the pharmacologically relevant parameters is necessary to bridge in vitro and animal model experiments to the human scale. Additionally, evaluation of local dose is important to understand the regional and global effectiveness of an inhaled drug. Accurate assessment of aerosol deposition along the airway tree and the concentration of deposition on the airway surface are also useful to evaluate airway functional features, such as mucocilliary clearance rate, and to test *in-vivo* the validity of computational models of aerosol delivery. The deposition of radioactive aerosol particles in the lung can be assessed in three dimensions (3D) with limited spatial resolutions using Positron Emission Tomography [PET] [26, 27] and Single Photon Emission Computed Tomography [SPECT] [28]. Co-registered High Resolution Computed Tomography [HRCT] images, obtained from PET-CT and SPECT-CT instruments, provide anatomical detail that could be used to localize the observed radioactivity within specific Anatomical Regions [ARs] and thus, to evaluate regional dosing of inhaled pharmacological agents.

The standard approach to evaluate local concentration of a radio labeled substance is to measure the average activity per unit volume within defined Regions of Interest [ROIs]. ROIs are binary black or white [BW] masks that serve to group voxels corresponding to specific ARs. These ROIs are either defined based on generalizations of the anatomy [26, 27, 29, 30] , or are segmented from detailed HRCT [28, 31] scans, when available. In the lungs, it is helpful to segment the lungs into ARs that encompass a portion of the central airway tree and the lung periphery. However, the number, size and location of airways that can be accurately segmented from HRCT images can vary substantially among subjects and within lobes, and may depend (among other factors) on the lung volume at which the CT images are acquired. Therefore a method to segment the lungs into *consistent* ARs is required to compare aerosol deposition across subjects and among lobes.

Even after defining consistent ARs, other challenges need to be confronted before aerosol deposition can be accurately evaluated; Regional deposition quantification with BW ROIs may be inaccurate due to partial volume and spill-over effects[32-34]. These inaccuracies are caused by image blurring due to the limited spatial resolution of the nuclear imaging methods (~6 and ~15 mm, for PET and SPECT respectively) and by the breathing motion of the lung during imaging. Also, although PET (or SPECT) images are automatically co-registered with the CT images in combined imaging instruments (i.e. PET-CT or SPECT-CT), shifts in patient position, or differences in average

lung volume between the PET and CT images, often require additional co-registration. The co-registration process includes errors that need to be considered when estimating regional activity.

Here we present a method to evaluate aerosol deposition that accounts for the effects described above by expanding the concept of BW ROIs into the Grayscale domain. To accomplish this, a Voxel Influence Matrix [VIM] is defined to describe how activity originating from an AR is sampled in each image voxel. VIMs include the combined effect of sources of blurring such as breathing motion, limited spatial resolution, registration and model uncertainties, and allows quantification of activity from airways within ARs with dimensions smaller than the spatial resolution of the nuclear medicine method.

Applied together, these methods leverage the high anatomical detail provided by HRCT to *consistently* estimate the distribution of aerosol among specified ARs, to more *accurately* describe the deposition image, and to describe such a distribution in pharmacologically relevant terms such as airway inner surface concentration (ISC), and peripheral tissue dosing (TD). These new concepts and algorithms were implemented and used to analyze the heterogeneity of ISC and TD at a lobar level within the lungs of bronchoconstricted asthmatic subjects.

Methods

The methods are separated into sections that describe portions of the process required to leverage information within the HRCTs to interpret PET deposition images.

Imaging Material and Methods

This section describes the methods of acquiring the PET and CT images. The protocol was approved by the Massachusetts General Hospital Internal Review Board (Application No. 2007P000493).

Image Acquisition: 14 mild-to-moderate asthmatic subjects were imaged the supine position with a PET-CT (Biograph 64; Siemens AG). The subjects were young (average 20.1 years), and predominantly female (4 male and 10 female) with BMI's less than 32. All subjects were mild intermittent or mild persistent asthmatics as defined by the NIH Global Initiative for Asthma [35] with FEV1 and FVC ≥ 80% predicted, less than daily symptoms, and peak flow or FEV1 variability of less than 30%. All subjects demonstrated reversible obstruction (≥ 12% on previous PFT's).

Bronchoconstriction was induced with five deep breaths of aerosolized methacholine via a DeVilbiss nebulizer and Rosenthal dosimeter (model 646, DeVilbiss Healthcare, Somerset, PA) while in the scanner. Methacholine concentration was equal to the subject's previously-determined PC_{20} (the dose causing a 20% reduction in FEV_1). Two HRCT images were obtained during breath

hold: one at total lung capacity before bronchoconstriction [TLC], and a second at mean lung volume after constriction [MLV]. MLV was estimated as the average lung volume during quiet breathing in a 30 second window prior to image collection. A signal proportional to instantaneous lung volume was acquired with an inductance plethysmograph (SomnoStar PT, SensorMedics Corp, Yorba Linda, CA). A trace of the instantaneous volume signal was presented to the subject on video goggles who, following a breath to TLC, was instructed to stop breathing and hold his/her breath when the trace reached a line defining his/her MLV.

An aerosol of ^{13}N-NH3 labeled isotonic saline was generated with a vibrating mesh nebulizer (Aeroneb Solo, Aerogen , Galway, Ireland) and delivered via an Idehaler holding chamber (Aerodrug, Cedex, France) into a mouthpiece. The aerosol reaching the mouthpiece was previously characterized by laser diffraction as having a 4.9 μm VMD with a GSD of 1.8[36] . Intrapulmonary aerosol deposition was imaged with dynamic PET during a period of 2 minute inhalation, and the next 8 minutes, while they lay supine in the PET-CT camera gantry. During the study the subjects wore a mouthpiece and a nose clip, and were allowed to breath freely at their chosen tidal volume, breathing frequency, and average lung volume.

CT Settings: Full chest HRCT scans were acquired in the supine position during a short breath hold (~12 s) at the specified lung volumes (MLV and TLC). The scanner was used in a helical mode to acquire 64 slices per rotation with 0.6 mm collimation, and a pitch of 1 mm. The energy settings were 120 kV peak, and 80 mA. Image reconstruction was done using the B31F kernel with a 0.75mm slice thickness (0.5mm slice increment and 0.25mm overlap). The kernel was recommended by the developers of the Apollo segmentation software used to identify the Anatomical Regions [ARs]. Each HRCT results in approximately 3.2 mSv of radiation exposure. Reconstruction of the image with a reduced field of view resulted in typical voxel dimensions of 0.6 x 0.6 x 0.5 mm.

PET Settings: The PET images were acquired in list mode and reconstructed using filtered back projection. Attenuation correction was performed using the CT image acquired at MLV. The subject was positioned on the scanner such that the PET imaging field covered 16 cm above the dome of the diaphragm. The PET imaging field covered 83±8% of the lung volume, with 4±3% missing from the apex, and 13±7% missing from the base. A deposition image was constructed by averaging the regional activity acquired for 7.5 min, starting 30 seconds after the end of the aerosol inhalation. The NH_3 PET image results in less than 1 mSv of radiation exposure, and typical reconstruction voxels are 5 x 5 x 2 mm.

Segmentation Methods

To identify consistent ARs from the HRCT images the following methods were used.

Lobe and Airway Segmentation: For each of the two HRCT scans, the lobes and the central airway tree were segmented and airways (up to the sub-segmental airways) were labeled automatically using Apollo™ software (Vida Diagnostics, Mountain View, CA). The segmentations and airway labeling were visually validated and manually corrected when required. The location of airway bifurcations and the airway dimensions were extracted from the software output.

Isolating a Consistent Portion of the Airway Tree: The number of airway generations that could be segmented within a lobe varied between subjects and between lobes. In order to avoid bias in analysis across subjects and among regions of the lung, it was important to define a set of airways that could be quantified systematically in all lobes in every subject and in every lobe. Though all sub-segmental airways were visible at TLC in all subjects, it was not always possible to identify with certainty their distal bifurcation (the feature needed for defining the end of an airway). Therefore sub-segmental airways were trimmed to a length equal to a fixed fraction of the average length of the segmental airways of that subject. This fraction (0.74) was calculated by averaging the daughter to parent length ratios between generations 3-4, 4-5, and 5-6 taken from a symmetric model [37], which correspond to the generations of sub-segmental to segmental airways in different lobes (Figure 1A).

Defining Airway and Peripheral ARs: To define airway ARs, the trimmed airway trees were segmented into 9 ARs. Of these, 5 lobar portions were defined as all airways distal to and including the corresponding lobar bronchi: Left Upper Lobe (LUL), Left Lower Lobe (LLL), Right Upper Lobe (RUL), Right Middle Lobe (RML) and Right Lower Lobe (RLL). The remaining airway tree was segmented into 4 additional ARs: the Intermediate Bronchus (BINT), the Right Main Bronchus (RMB), the Left Main Bronchus (LMB) and the Trachea (TRC). Five peripheral ARs were defined from each of the segmented lobes by excluding intra-parenchyma airway ARs (Figure 1E).

Methods to Transform the Airway Tree

Information from the two HRCT images was used to estimate the motion of the airway tree and its location within the PET imaging field.

Co-registering HRCT Images: Though the subjects were imaged in a single session and were instructed to remain still on the table throughout the course of the study, in some cases motion between the two HRCT scans (taken between 30-60 minutes apart) was visually apparent. This

motion is not related to breathing and needs to be isolated before a model of airway motion can be extracted from the images. To correct for differences in subject positioning, the upper spines in both images were segmented and co-registered using custom software (Matlab, Natick, MA). The co-registration algorithm sought to maximize overlap of the upper spines (using the Tanimoto Similarity Coefficient [38]) as the images were shifted relative to each other along the horizontal plane of the camera table without rotation (Figure 1F); rotation was unnecessary since the narrowness of the gantry table prevents significant rotation.

Mapping TLC to MLV: The airways move and expand with lung inflation. Due to the fixed spatial resolution of HRCT a greater extent of the airway tree can be reliably segmented from the TLC image compared with that from the MLV image. However, aerosol imaging with PET or SPECT is done during tidal breathing at a volume that varies around MLV. As a result, ROI's derived from the image at TLC cannot be directly used to analyze PET deposition images. To resolve this issue, the more detailed TLC airway tree was mapped to that at MLV by fitting an affine transformation to the positions of common anatomical bifurcations between the two scans. Mathematical details of this transformation are covered in Appendix I.

Co-registering the PET and HRCT Images: Even though in the PET-CT scanner PET and CT voxels are physically co-registered, in 12 of 14 subjects it was necessary shift the images relative to each other in order to overlay the deposition within the airway tree (visible as hot-spots in the PET image) with the airways rendered from the CT scan. In 9 cases shifting alone could not match the deposition pattern; the deposition image appeared to have been collected at a different average lung volume than that of MLV HRCT. In these cases a parametric function that allowed estimation of the airway position as a function of lung volume was used. The function was chosen so that the volume of the airways scaled linearly with lung volume, and is described in Appendix II. The parameterized transformation was used to identify the lung volume that resulted in the best visual overlay between PET and HRCT images. The simplest registration was employed when no evident improvement was gained by adding complexity to the co-registration (in order of preference: no added co-registration, shifting only co-registration, shifting plus volume co-registration).

Accounting for Sources of Blurring

This section introduces the use of Voxel Influence Matrices [VIMs] to model the sources of blurring and uncertainty in the PET images. Whereas the HRCT images are collected during a breath-hold, the PET or SPECT images are normally collected during breathing. Depending on the isotope and method, imaging times typically range from 10-60 minutes. The limited spatial resolutions of PET

(~6mm FWHM) and of SPECT (~15mm FWHM) create partial volume and spill-over effects that further exaggerate the blurring. Blurring causes activity within an airway to be spread over a region that is significantly larger than the physical airway. When activity from a central airway, or peripheral region, does not include spill-over effects from other sources the total activity from the region may be assessed by considering a large ROI that covers the entire blurred region [28]. However, when the counts from a region are affected by multiple sources (such as two neighboring airways) the activity within an enlarged ROI cannot be assigned to a single source. An additional blurring of the data comes from the discrete voxel representation of continuous data.

VIMs: Blurring, uncertainty and discretization cause activity originating within an AR to be sampled in regions outside of it. Careful consideration of each of these effects permits the estimation of how activity within each AR contributes to activity within any voxel of the image. A VIM captures this measure for each AR. The sum of an AR's VIM is equal to its volume (in number of voxels); the VIM essentially redistributes the volume of the ARs to match their expected appearance in a PET image (Figures 1C, 1G). VIMs are therefore a model of the apparent distribution of the AR volume as seen with PET divided by the voxel volume, and its units are this dimensionless fraction

Modeling Airway Blur Due To Breathing Motion: The PET image was taken during spontaneous tidal breathing that spanned a range of lung volumes around MLV. Using the parameterized transformation of the airway tree with lung volume, a model imitating airway motion during breathing was created. The function spreads the airway over the voxels through which airways moved during a tidal breath of 500 ml centered on the average lung volume during deposition imaging.

Limited PET Resolution: The spatial resolution in PET (6mm FWHM) is substantially lower than that of HRCT (0.3mm). This leads to blurring by detecting activity originating within the central airways in voxels outside of the airways border. Thus, if ROIs were simply defined by following airway boundaries from HRCT, this would lead to substantial underestimation of the aerosol deposition within a given airway. A convolution with the point-spread function defined for the PET camera and reconstruction algorithm was utilized to further blur the motion-blurred ROI's.

Accounting for Transformation and Registration Error: Even after co-registration, imperfections in the overlay between the CT airway mask and the high activity regions in the PET image were occasionally observed. These could arise from error in the TLC to MLV mapping (characterized by the root mean square error of the affine transformation (4mm FWHM) or from

limitations in the visual-guided registration described above (empirically estimated to be ~5mm FWHM). To account for these sources of uncertainty, the motion-blurred airway tree was further blurred by convolution with a single 3D Gaussian function that considered the effects of the PET point spread function, volume mapping and co-registration error. The FWHM of this Gaussian function was defined as root sum of squares of the FWHM of each of the blurring effects (Figure 1B).

Estimating Airway and Peripheral VIMs: To estimate airway VIMs, each of the 9 airway ARs was blurred to model the effects of motion, PET resolution and registration uncertainty (Figure 1C). To estimate peripheral VIMs, each segmented lobe was first blurred for PET resolution and uncertainty and then the sum of all airway VIMs was removed from each element of the peripheral VIM (Figure 1G).

Methods to Evaluate Deposition from the PET Image

Two different methods to identify the aerosol distribution were implemented and applied to the same imaging data sets.

Black or White Method: Here, the standard approach was used where ROIs were defined at PET resolution from their corresponding ARs segmented at CT resolution. Each voxel of the image was assigned to a single AR to avoid counting activity more than once. When a PET voxel included voxels from more than one AR an algorithm was used to choose one of them. One algorithm considered for resolving this conflict was to assign PET voxels to the AR that has the largest fraction of the voxel volume. However, this algorithm did not include voxels with smaller but still visible airways (that rarely occupy the majority of a voxel) into the airway ROIs. For this reason the selection of ROI voxels was biased toward the airway ARs with a weighting factor of 100. Once the imaging field was divided into non-overlapping BW ROIs, the average specific activity (activity per unit volume) within each ROI was estimated by dividing the total activity sampled within the ROI by its volume.

Grayscale Method: Here, a new approach was used where VIMs, and not ROIs, were defined for each of the ARs. As described above, VIMs simultaneously considered the influence of activity within all ARs on every voxel. In the contrast to the BW Approach, activity within any voxel could be contributed to multiple ARs. Thus, VIMs describe the effect of blurring, uncertainty, as well as the contribution of small airways (without the addition of an arbitrary factor to bias the small airways). Formally, considering m number of VIMs [R_i], of the same size as a PET deposition image [D] we

seek to estimate the average specific activity within each AR [x_i] that, after blurring, results in the best approximation of D, or:

$$\sum_{i=1}^{m} R_i x_i = D \qquad (1)$$

This can be rewritten as a 2D linear algebra equation by reshaping the 3D VIMs and the deposition into 1D column vectors. Using Matlab notation (where R(:) is the column vector of any dimensional R):

$$\begin{bmatrix} | & | & & | \\ R_1(:) & R_2(:) & \dots & R_m(:) \\ | & | & & | \end{bmatrix} \begin{bmatrix} x_1 \\ x_2 \\ \vdots \\ x_m \end{bmatrix} = \Re X = D(:) \qquad (2)$$

Nonphysical negative solutions of X were avoided using the Matlab's lsqnonneg($\Re, D(:)$) function. Once X has been solved for, $\Re X$ is the deposition pattern based on average depositions within the ARs that is closest to D. This type of deposition pattern is also used for BW ROIs to generate the images in Figure 2A.

Comparison of the BW and Grayscale Approaches

To understand how the analysis method affected the quantification of the PET deposition images, they were applied to the same imaging data sets. Results from both methods where compared to each other and on how well they represented the PET images they were derived from.

Comparisons with the PET Images: Analysis of the PET deposition images using either of the methods reduced imaging data from an average of 50,000 voxels to 14 degrees of freedom. Using these regional values and the 3D information from the ROIs or the VIMs, synthetic 3D images were created and compared to the original PET images. The goodness of fit was captured using the coefficient of determination [R^2] value. The R^2 was evaluated within the regions covered by BW ROIs excluding the large central airway ROIs to avoid the errors caused by activity in the esophagus, a region that was not accounted for in the ARs analysis. The statistical difference in R^2 between the two methods was evaluated using a paired t-test.

Inter-Regional Heterogeneity in Aerosol Deposition: For each AR, the values of aerosol deposition obtained with both methods were assessed for each in terms of the volume-normalized

regional depositions (specific depositions). For BW method, regional specific deposition was estimated as the total activity within the ROI divided by the ROI volume. For the Grayscale method the regional specific activity was the total activity assigned to the AR divided by the AR volume. The spatial heterogeneity of the distributions was characterized by a penetration index [PI] defined as the periphery-to-airway ratio of specific activities for each lobe. The variability of the PI values was characterized by the inter-subject variation in Lung Averages and by their inter-lobar COV (the standard deviation divided by the mean). The Lung Average was the average PI of the whole lung (without separating lobes) and its variability was characterized as the COV across subjects. The inter-lobar variability was the average of the COV of lobar values for each subject. The null hypothesis that all lobes behaved identically was tested using ANOVA with repeated measures. When differences were evident at the 5% alpha level a Holm-Sidak test for multiple comparisons was used to test for individual differences between lobes [39].

Pharmacologically Relevant Units

From the data derived using the Grayscale method, the regional deposition could be described in terms of the Tissue Dosing [TD] and the Inner Surface Concentration [ISC]. Evaluating this parameters required extraction of additional information from the HRCTs as follows.

TD: In the peripheral ARs, TD was defined as the fraction of the total lung dose per unit of tissue mass. To exclude the volume occupied by blood, the regional "tissue mass" was estimated as the mass of water occupying half of the non-air volume if each lobar AR provided by the Apollo ™ software.

ISC: In airway ARs, ISC was defined to quantify the concentration of the aerosol per unit of airway surface. To calculate the ISC it was necessary to estimate the surface area of each within each of the airway ARs using the method described in Appendix III.

Individual values of TD and ISC were characterized by the Lung Average and the Lobar COV, and differences between lobes were tested in the same manner as the PI [39].

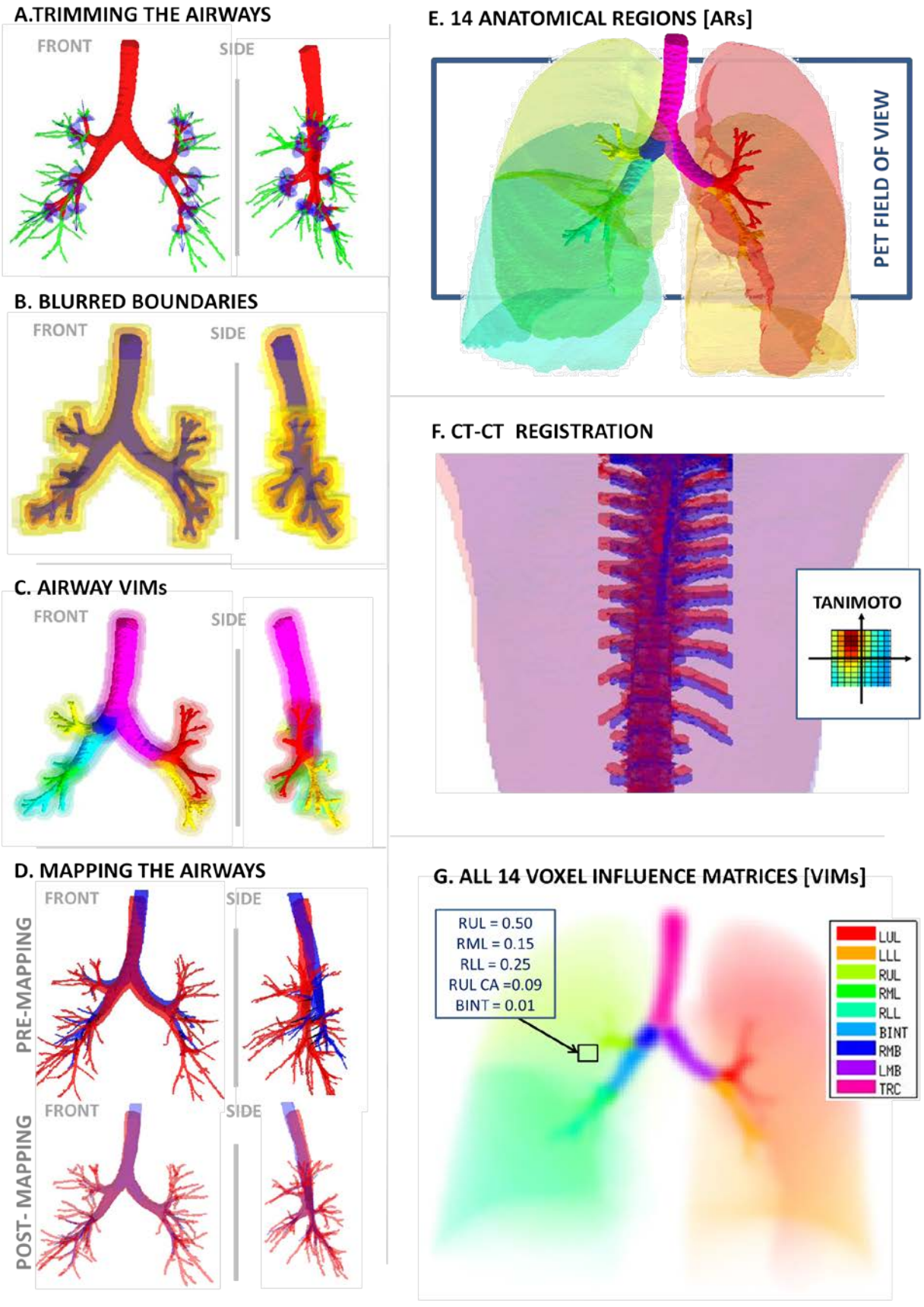
A.TRIMMING THE AIRWAYS
FRONT
SIDE
B. BLURRED BOUNDARIES
FRONT
SIDE
C. AIRWAY VIMs
FRONT
SIDE
D. MAPPING THE AIRWAYS
PRE-MAPPING
POST- MAPPING
FRONT
SIDE
E. 14 ANATOMICAL REGIONS [ARs]
PET FIELD OF VIEW
F. CT-CT REGISTRATION
TANIMOTO
G. ALL 14 VOXEL INFLUENCE MATRICES [VIMs]
RUL = 0.50
RML = 0.15
RLL = 0.25
RUL CA =0.09
BINT = 0.01
LUL
LLL
RUL
RML
RLL
BINT
RMB
LMB
TRC

Figure 1: Panels illustrate the methods. A: The TLC airway tree is trimmed to the sub-segmental generation to obtain a central airway tree ROI that is consistent across subjects. In light blue are umbrella shaped cutting elements oriented with the segmental airways. In green are the trimmed portions of the tree. B: The boundaries of the airways before and after the addition of sequential sources of blurring; the trimmed TLC @ MLV airway tree (purple), motion blur (light purple), PET blur (orange), including transformation and registration error (darker yellow), and the final PET mask discretized to the PET deposition image (light yellow). The boundaries represent the point where the voxel VI >0.1%. C: The nine airway tree ARs (shown in saturated colors), and iso-contours of their corresponding VIMs in matching colors representing 10%, 1%, and 0.1% VI are drawn for each AR (the color legend is shown in panel G). D: Effect of mapping airway tree from TLC to MLV: Front and lateral projections of the airway tree (Top) rendered from a CT acquired at TLC (red) and one at MLV (Blue). (Bottom) The same as above, but with the TLC tree mapped to the MLV. E: A Rendering of the 14 Anatomical Regions (ARs). The color legend is shown in panel G. The lobar central airways are color matched to the lobes that they feed. The 16cm PET field of view and the typical placement of the PET image are shown with the rectangle. The lung volume for this subject was 4.7 L at MLV (average volume at MLV was 3.2 L). F: The co-registration of the TLC (red) and MLV (blue) spines. The inset shows the variability in the Tanimoto Similarity Coefficient of the upper spines as the images are shifted relative to each other. The dark spot shows that the HRCT images are best co-registered when the blue spine is shifted up and to the left. G: A visualization of the VIMs. Each color indicates the VIM of a single AR. VIMs estimate of how homogenous activity within an AR appears in the radionuclear image. Where in a conventional black or while ROI each voxel is assigned to a specific AR, the rectangle shows how the voxel is influences by many ARs.

Results

Affine Transformation: The affine transformation mapped the TLC airway tree to the MLV airway tree and reduced the average distance between locations of bifurcations by 92 ± 4% from 21.5mm to 1.5mm. The difference between the mapped bifurcations and the bifurcations locations at MLV had a FWHM of 4mm. One example of this transformation is shown in Figure 1D.

Comparison of regional predictions: Anterior-posterior (A-P) projections of the deposition images of 3 of the subjects are compared with A-P projections of the synthetic images generated from the results for each of the two methods Figure 2A. Note that if the method captured all information from the original image, its synthetic image would be identical to the original PET image; discrepancies between the two indicate loss of information in the description of the data. The coefficient of determination of the Grayscale method was higher than the BW method for all subjects ($P < 0.0001$). This suggests that the Grayscale method is a better model to represent deposition observed in the PET image than with the BW method Figure 2B.

Penetration Index: The Grayscale method yielded lung average values of PI that were in average 7.0 ± 1.5 times those estimated using the BW method. At a lobar level the factor ranged from 4 to more than 17 times. The relative variability in PI derived from the Grayscale method was higher among lobes and among subjects than the BW method (Table 1). Figure 2C shows how the Grayscale method uses VIMs to localize the blurred PET image in to the Anatomical Regions [ARs]. The rest of the results presented below used exclusively the Grayscale method.

Lobar Variability of Specific Deposition: There was high variability between in the total specific deposition among the lobes (Total Specific Deposition Lobar COV = 0.33 ± 0.12). The variability was similar when the lobes were divided into central (Central Airways Specific Deposition Lobar COV = 0.33 ± 0.15) and peripheral regions (Peripheral Specific Deposition Lobar COV = 0.34 ± 0.14).

Heterogeneity of deposition in Pharmacological Terms: The Total Lung Dose [TLD] was 14.2 ± 5.6 % of the total administered dose. The Lung Average of Tissue Dosing [TD] was 2.11 ± 0.40 x 10^{-6} TLD/mg and the TD Lobar COV was 0.30 ± 0.14. No systematic difference was observed between TD of lobes. The Lung Average of Inner Surface Concentration [ISC] was 45 ± 14 x 10^{-6} TLD/mm^2, and the ISC Lobar COV was 0.31 ± 0.15. The LLL had a systematically lower ISC than the RUL ($P<0.001$), the RLL ($P< 0.01$) and the RML ($P<0.05$). The data are shown in Figure 2D.

Figure 2: Panels illustrate the results. A: PET deposition images for 3 subjects (1st column) contrasted with images of activity estimated with the two methods: BW and Grayscale. The estimated images are created by multiplying the ROIs used in each method by the estimated regional specific activities. The color scale within each row is kept constant with the darkest red corresponding to the point with highest activity. Both methods assume uniform deposition within the AR, which tends to diffuse hotspots in the estimated images. However, the Grayscale method tends to reproduce location and magnitude of hotspots better than the BW method. Note that the activity on the esophagus (present in the lower two PET images) is not represented in the projections since it was not defined as an AR (see discussion). B: The coefficient of determination of the two methods. In all subjects the description of deposition with the Grayscale method is closer to the PET image ($P < 0.0001$) than with the BW method. C: (Left) Projections of the ARs (at CT resolution) in blue overlaid with a projection of the deposition image (at PET resolution) in red. (Right) Projection of the estimated activity within the ARs (at CT resolution) using the Grayscale method. D: The PI, TD, and ISC using Grayscale across lobes. Individual subject data are connected with dashed lines. The solid line is the average lobar values. No statistical difference was observed between a given lobe's TD. The LLL showed lower ISC than the lobes of the right lung (the strength of the line between the lobes under STATS indicates the strength of the P value).

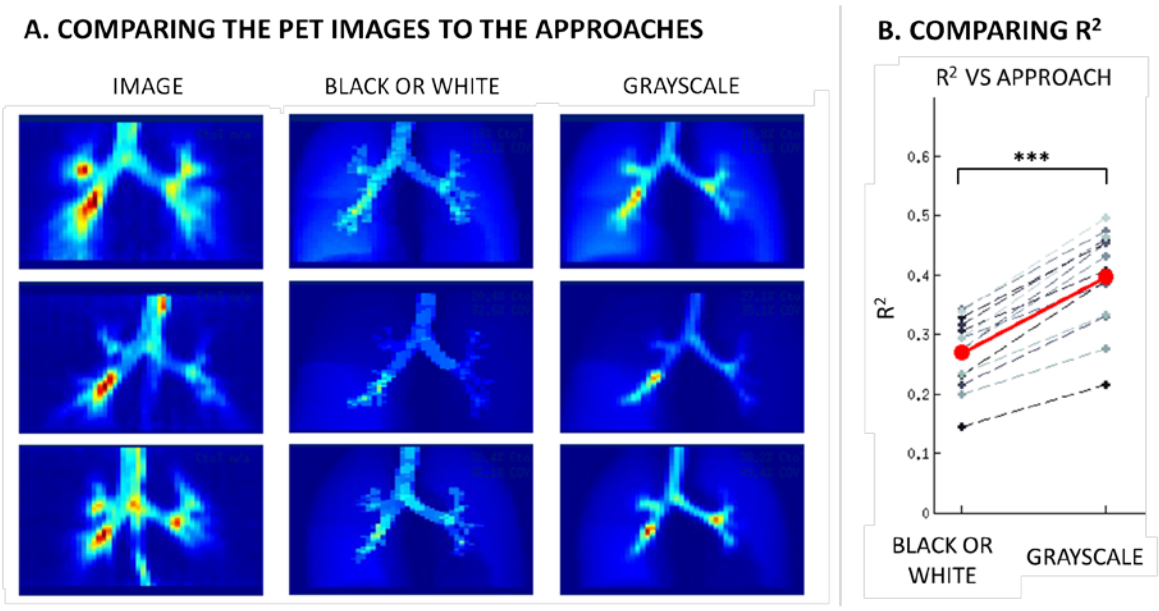
A. COMPARING THE PET IMAGES TO THE APPROACHES
IMAGE
BLACK OR WHITE
GRAYSCALE
B. COMPARING R²
R² VS APPROACH
***
R²
BLACK OR WHITE
GRAYSCALE

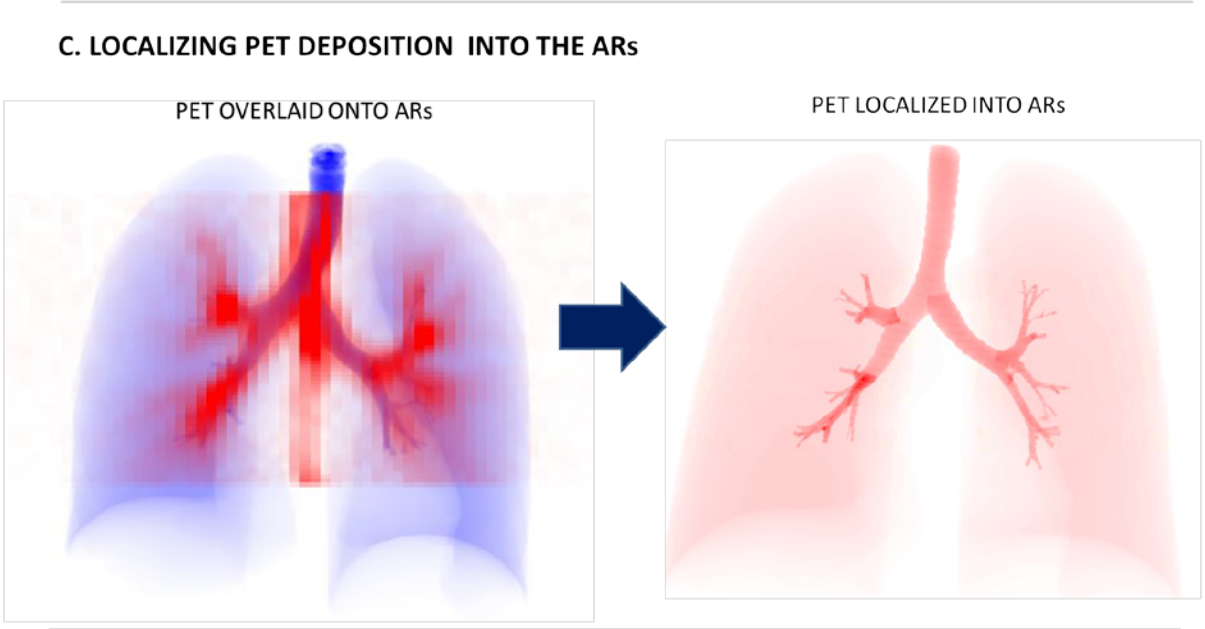
C. LOCALIZING PET DEPOSITION INTO THE ARs
PET OVERLAID ONTO ARs
PET LOCALIZED INTO ARs

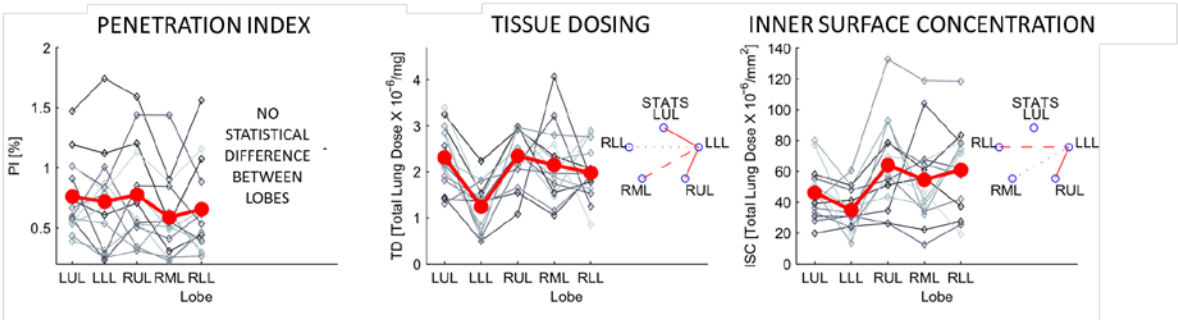
D. LOBAR PI, TD, AND ISC
PENETRATION INDEX
PI [%]
NO STATISTICAL DIFFERENCE BETWEEN LOBES
LUL LLL RUL RML RLL
Lobe
TISSUE DOSING
TD [Total Lung Dose X 10⁻⁶/mg]
STATS
LUL
RLL
LLL
RML
RUL
INNER SURFACE CONCENTRATION
ISC [Total Lung Dose X 10⁻⁶/mm²]

Discussion

The methods above defined anatomically consistent regions of the lung (ARs) from HRCT. The concentration of aerosol deposited within the ARs were measured with lower resolution nuclear medicine imaging methods (PET and SPECT). A novel Grayscale method was developed to account for the effects of image blurring and uncertainty and for the contribution of airways too small to be identified with the limited resolution of the nuclear medicine imaging devices. In this method, Voxel Influence Matrices (VIMs) are used to evaluate the average specific deposition in each of the ARs and provide estimates of the pharmacologically relevant parameters TD and ISC.

The Grayscale method presented here is an extension of methods previously used to account for limited spatial resolution of imaging methods [32-34]. A similar formulation was described by Berker et al. to improve quantification of radionuclide therapy dosing [32], based on the method introduced by Rousset et al. to account for blurring in PET imaging of the brain [33]. A version of Rousset's method was applied by Fleming et al. to correct for partial volume effects between concentric shells in SPECT evaluation of aerosol deposition [34]. Here, we generalized the concept by defining VIMs and adding breathing motion and co-registration uncertainty to the effect of limited imaging spatial resolution. Thus, VIMs can be thought as the influence (probability of effect * degree of effect*)* that activity within each AR has on measured activity at any point in the image. This represents a new method to analyze radionuclide images and shifts the paradigm from a Black-or-White to a more flexible Grayscale method.

Both methods were implemented and applied to the deposition on the lungs of bronchoconstricted asthmatics. In these subjects, aerosol administration and imaging were performed in the supine position. While aerosol therapy is usually done in the upright position, having the actual airway geometry during deposition (which is different that upright) will allow to use this data for validating computational models of aerosol deposition.

Both the BW and Grayscale method only explain part of the variance on the image (with R^2 of 0.27 and 0.39 respectively). A major source of the unexplained variance is the intra-AR variability; the method estimate the average deposition within each ARs, while in our data the deposition in the peripheral ARs was clearly concentrated near the visible large airways (see the first column in Figure 2A). The averaging of activity within the AR diffuses the appearance of local hot spots. While we are interested in the average deposition within the ARs (and not in exactly reconstructing the PET images), the assumption of homogenous deposition within an AR affects the estimates of average specific deposition in the following ways: 1) It underestimates the spill-over

of activity just beyond the central airway ARs, and thus the activity in the central airways. 2) The deposition in the portions of the lobes not included in the PET field of view (which are usually far from the central airways) was likely smaller than the average deposition in the measured part of the lobe; the assumption of homogeneous specific deposition throughout the lobe introduces error and tends to overestimate the amount of activity in the periphery. These issues might be mitigated by dividing the lung into a greater number of ARs. Despite this, Grayscale method yields a less diffuse description of deposition that is closer to the original PET image than the BW method ($P<0.0001$).

To use the more detailed airway tree at TLC in the analysis we formulated an affine transformation that described the displacement of bifurcation points between TLC and MLV (Appendix I). Parameterizing the affine by the global lung volume, allowed estimation of blurring due to tidal breathing motion and also registration of the HRCT anatomy to the PET deposition images (Appendix II). Other methods have been used in the past to describe the displacement of landmarks between images (e.g. B-spline [40, 41], elastic-body spline [42, 43] , thin-plate spline [44, 45], or moving least squares [46]). There are also alternative semi-automatic methods to extract the displacement of points in the lung [46, 47] as well as image registration techniques [41, 48]. The simple affine transformation applied to automatically detected bifurcations was successful in mapping intrapulmonary airways from TLC to MLV (see Figure 1D) and made it possible to parameterize the function in a way that linearly transformed the airway tree with global lung volume in a way consistent with the HRCT images. One of the alternative methods for modeling lung motion [41] assumes that each point of the tree moved along a line connecting the point in both images, where the position of point along the line was determined by the relative change in lung volume. If the motion of the airway tree did not include rotation, this method and the parameterized affine transformation would lead to similar results. Nonetheless, in the presence of the rotation expected by the inflation of a taper shaped lung and chest wall (see Figure 2D for an example of this) the inline motion method would not preserve the linear relationship between airway volume and lung volume.

The TLC image was taken before bronchoconstriction to maximize the fraction of the visible airway tree. While the position of the airways is not expected to be very different after bronchoconstriction, measurements of airway caliber taken from the TLC image likely do not reflect the bronchconstricted state.

Parameterizing the affine transformation by global lung volume is clearly an approximation. Relative expansion of the different lobes during breathing can be quite different from that of the total lung [49] particularly in lungs with heterogeneous airway resistance as in asthmatic lungs during bronchoconstriction [50]. Even in normal lungs, changes of shape and volume depend on at least two independent parameters: the motion of both the diaphragm and that of the ribcage. In the absence of images, or models from which these parameters could be estimated, modeling the airway tree motion using a global lung volume parameter is a necessary simplification.

Even though in a PET-CT scanner the PET and CT images were acquired by the same instrument and their voxels were spatially co-registered, in a number of cases additional co-registration was required due to subject motion and/or differences in lung volume between the images. This co-registration was feasible because in our data, the central airways had substantially higher specific activity than the periphery. We believe that the highly central pattern of deposition observed likely resulted from the breathing pattern (spontaneous free tidal breathing), the bronchoconstricted state of the subject, and the aerosol specific to this study. In inhalation conditions with more peripheral deposition patterns co-registration may be done with the external boundaries of the chest wall. It should be noted, however, that the PET to CT registration could erroneously mask two potential effects on the pattern of deposition; systematic sedimentation on the gravitationally dependent side of the airway, and impaction along the inner walls distal to each bifurcation. However, even the complete sedimentation within an airway in the horizontal plane would only shift the deposition by ½ an airway diameter; registration based on the smaller of the central airways is only weakly sensitive to these differences. Similarly the impaction effect would result in more distal deposition, but in a different direction for each bifurcation; global registration based on the whole tree should only be weakly sensitive to this effect as well. Reducing the time between scans and controlling the lung volume during both images should decrease the need for additional co-registration. Alternatively, co-registration techniques with fiducial markers visible in both imaging modalities (such as those in Berridge et .al.[26]) could be used. Despite significant work automating the co-registration algorithm, in some cases visual identification of the best co-registration was ultimately necessary. Though this is common in deposition imaging [28], it does reduce the reproducibility of the technique.

Our PET-CT imaging protocol used a HRCT image taken during breath hold at MLV to provide attenuation correction for PET images taken during breathing. While breathing over the course of the PET image, the anatomy is at a different position than in the HRCT image for most of

the breathing cycle (below or above MLV). This leads to errors in the most peripheral regions of the lung, particularly close to the diaphragm and the ventral side of the lung where the largest distances of lung tissue movement occur during tidal breathing. Additionally, even though the CT attenuation scan at a volume equal to the average lung volume during breathing, the filtered back projection reconstruction of the PET images can lead to negative values of activity near the chest wall. In our analysis the negative values were set to zero to minimize the underestimation of activity in the periphery of the lung. The attenuation problems at the chest wall would be more exacerbated when the attenuation CT is acquired at FRC, as recommended in [27]. Errors due to attenuation correction can be improved using a conventional transmission scan or a long exposure low energy CT taken during breathing. Gating the images to the breathing cycle can also reduce these artifacts, though there is a necessary signal to noise penalty. Alternatively, breath holds at MLV (which are possible only with PET, such as those implemented by Lee[51]) after inhalation could yield sharper images with fewer co-registration and attenuation concerns. However, eliminating the blurring due to breathing would be at the expense of a reduction in signal to noise.

High activity was seen in the esophagus of many subjects, which resulted from swallowing activity that was deposited in the oral cavity. While Lee[51] manually separated the Esophagus from the airways, we were unable to confidently separate the two sources of activity. Grayscale separation of these sources was hindered by the HRCT scans inability to delineate the location of the esophagus. In future studies a rinse with water could be used after aerosol inhalation (if somewhat difficult in the supine position) to lower the activity in the esophagus [7]. Another limitation of the data is that the fraction of the trachea included in the PET and CT images varied between subjects. For these reasons care must be taken interpreting values of deposition in the trachea, RMB and LMB.

The primary focus of this chapter is to describe an enhanced method to evaluate the anatomical distribution of an inhaled aerosol within the lungs using 3D imaging data from PET and HRCT. In future studies, the method could be used to estimate regional tissue dose and airway surface concentration as a percent of the inhaled dose. This will require assessment of radiation concentration in extra-pulmonary regions such as the oral cavity, pharynx, esophagus and stomach that were not imaged in the current study.

To our knowledge this is the first report of PET imaging data of asthmatics evaluating the centrality of the distribution pattern of an aerosol inhaled under our experimental conditions, namely: spontaneously breathing in the supine position and under provoked broncho-constriction.

It is of interest to note the exaggerated centralized pattern that is visually apparent from our data has a similar appearance to the deposition pattern of monodisperse 6 μm albuterol in aerosol observed with scintigraphy by Usmani [19] in asthmatics in the sitting position. Given that those subjects were mild-to-moderate asthmatics with an FEV1= 78% predicted, and that the bronchodilator aerosol was inhaled in three consecutive breaths, it is unlikely that the bronchodilatory effect of albuterol had substantially reduced the degree of bronchoconstriction during the short inhalation period. In our study the subjects had much higher baseline FEV1 (102% predicted) but were challenged with methacholine at a dose to reduce FEV1 by 20% at the beginning of the study, resulting therefore in equivalent degrees of obstruction during inhalation of the NH3-labeled aerosol.

We characterized the serial distribution of the aerosol deposition by the penetration index (PI) as recommended for standard for analysis of SPECT [28] and gamma camera deposition [30]. Here, the Grayscale method yielded average values of PI that were seven times lower than those obtained with the BW method. The main contributor to this difference is the different volumes over which the activity in the airways is concentrated; in the BW method the volume of the ROI is used (which is generally larger than the AR volume), while in the Grayscale method the actual AR volumes (built into the method) are used (Figure 3). This effect is largest in the central airways where the ROIs are 4.3 ± 1.5 times larger than the ARs. While it is possible to post process the BW deposition pattern to concentrate all the activity within the ROI into the AR volumes, this would neglect to account for activity that is in fact coming from the periphery. This problem becomes more significant with higher penetration indexes.

Average deposition on the three most central airway generations of each lobe (lobar, segmental, and sub-segmental) and on the rest of the lobe (periphery) were estimated in addition to the larger extra pulmonary airways. The method could be extended to analyze individual segmental or even the sub segmental airway ARs. However, as the images are divided into smaller regions approaching the length scale of blurring and uncertainty (~ 10mm) affects, it becomes increasingly difficult to separate the sources of the activity.

Aerosol deposition in 3D has also been analyzed using empirical models of airway tree morphometry to estimate deposition on different generations of the airway tree. In those methods the lung was divided into concentric shells (around the hilum [26, 28, 29, 52] or the carina [27]). An estimate of the volume occupied by airways of each generation within each shell was derived from a symmetrical airway tree model [29], or from a HRCT scan of a human lung cast [52] . Based on the

assumption that activity within each generation is uniform throughout the lung, an estimate of the fraction of the deposition per generation was inferred[28, 29, 52]. Although the average deposition within each shell was assessed after correcting for partial volume effects, the effects of lung motion during breathing or co-registration uncertainty between the morphometric model and the anatomy were not considered. As in-vivo imaging of aerosol deposition cannot presently visualize small airways, methods based on generalized morphometry seem the only viable method to estimate deposition within airways beyond the sub-segmental generations. However, our results showed that the deposition parameters in bronchoconstricted asthmatics were highly variable between lobes, and thus it would be at least necessary to analyze the lobes, or segments, separately before a shells approach could be meaningfully implemented. This approach could be integrated into the present method by defining generational ARs (at a lobar level) from generic morphometry or a lung cast. The resulting VIMs would avoid the loss of information that takes place when the airway generation is only described by its relative distance from the hilum.

The two pharmacologically relevant parameters TD and ISC were evaluated in the population. In the calculation of TD, the lobar deposition was assumed to be distributed over the tissue mass of the lobe. Tissue mass was estimated as one half of the non-air fraction of the lung (provided by the Apollo software) to account for the volume occupied by blood. This assumption may be avoided by directly assessing regional blood volume using contrast media in CT or ^{11}CO in PET. Also, because the deposition in the periphery is not evenly distributed throughout the tissue (it is likely concentrated in the airways), the TD presented here is only a first order approximation.

The inner lumen surface areas within the central airways were estimated to calculate regional ISC of the aerosol. It is important to note that the surface area measured from CT changes with lung volume. We chose to use the area measured at MLV because it provides a value that best approximates the inner area during breathing for that subject. The present measurement does not account for folding of the surface area that can happen in the smaller airways not visible with CT, and it is likely that the ISC is in fact lower than is estimated here in some airways.

The Grayscale method for analysis of regional aerosol deposition revealed additional heterogeneity between lobar deposition patterns in bronchoconstricted asthmatics. This average inter-lobar heterogeneity was similar whether the serial distribution was presented in terms of the volume normalized PI (Lobar COV = 0.30) or the parallel distribution expressed in pharmacologically relevant terms TD (Lobar COV=0.30) and Lobar ISC (COV=0.31). In practical terms, these results demonstrate that the serial (PI) or parallel (TD and ISC) heterogeneity may

need to be taken into account when estimating the concentration of inhaled aerosol medications to heterogeneous lungs, If we consider the additional intra-lobar deposition heterogeneity not considered here we venture to speculate that substantial parallel variability in tissue exposure within the lung could be responsible for significant reductions in effectiveness of certain inhaled medications[31].

In summary, four main improvements of the proposed methodology over standard methods are presented here. First, anatomically consistent lobar airways are defined to allow unbiased comparisons between lobes and subjects. Second, subject movement, breathing motion, limited PET resolution, the contribution of small airways and registration inaccuracies are accounted for in the estimation of regional anatomical deposition. Third, the more detailed airway tree imaged at TLC is used to interpret deposition imaged at lower lung volumes. Fourth, specific deposition values were correctly normalized by the airways true volume instead of the conventional ROI volume thus avoiding gross underestimations of central airways specific activity. It was demonstrated that the standard Black or White ROI method substantially underestimated the specific deposition of aerosol in central airways. In contrast, the Grayscale method described the PET image more accurately, correctly assigning deposition to the volume of the AR, and yielded estimates of deposition terms such as tissue dose, TD, and inner surface concentration, ISC. These pharmacologically relevant terms could be important in translational research as well as in evaluation of novel aerosol delivery systems. More generally, the notion of voxel influence matrices, VIMs, represents a paradigm shift in the analysis of radio-tracer localization within the anatomy that could have applications in other imaging modalities.

Acknowledgements

This chapter was sponsored by NIH grant HL68011, and by support from American Air Liquide Inc. Aerogen is thanked for providing the vibrating mesh nebulizers.

Author Disclosure Statement

This chapter was sponsored in part by American Air Liquide Inc. and Aerogen. However, there is no conflict of interest with these parties on any of the material presented in this chapter.

Appendixes

Appendix I. Affine Transformation:

An affine transformation is any transformation under which a straight line in the original space remains a line in the transformed space. In 3D this allows for any combination of translation, scaling and rotation. If a series of points are positioned at points

in the TLC image move to positions in the MLV image, we can organize the points into corresponding rows of matrices X_{TLC} and X_{MLV} then add a column of ones to the end of each matrix. We can write the system of equations for the affine transformation matrix B_{TLC}^{MLV} (which can be solved using least squares with the backslash operator in Matlab):

$$B_{TLC}^{MLV} X_{TLC}{}^{T} = X_{MLV}{}^{T}, \text{ or } B_{TLC}^{MLV} = \left[X_{TLC} \setminus X_{MLV}\right]^{T} = \begin{bmatrix} R_{TLC}^{MLV} & d_{TLC}^{MLV} \\ 0 \quad 0 & 0 \quad 1 \end{bmatrix} \tag{3}$$

By applying all points in the TLC airway tree to the B_{TLC}^{MLV} affine we were able to transform the TLC airways to MLV.

Appendix II. Volume Corrected Affine Parameterization:

The above affine transformation yields a transformation for point in the TLC image to points in the MLV image. We sought to find parameterize this transformation with lung volume to find the transformation from TLC to other lung volumes (Identified with subscript VOL). As the affine transformation from TLC to TLC is the identity matrix, one simple way is to do this is to suggest that each of the components of the affine moves from its value in the identity matrix at TLC to corresponding B_{TLC}^{MLV} entry at MLV with a single volume dependent parameter s_{VOL}:

$$\widehat{B}_{TLC}^{VOL} = s_{VOL}\left(B_{TLC}^{MLV} - I\right) + I = \begin{bmatrix} \widehat{R}_{TLC}^{VOL} & d_{TLC}^{VOL} \\ 0 \quad 0 \quad 0 & 1 \end{bmatrix}, \text{ where}$$

$$s_{VOL} = \frac{\left(V_{VOL}\right)^{\frac{1}{3}} - \left(V_{TLC}\right)^{\frac{1}{3}}}{\left(V_{MLV}\right)^{\frac{1}{3}} - \left(V_{TLC}\right)^{\frac{1}{3}}} \tag{4}$$

However, this does not ensure that the actual airways volume under the transformation will match the expected airways size at V_{VOL}. It can be shown that the absolute value if the determinant of R (the upper three by three of any affine matrix B (which holds a combination of the rotation and scaling effects) is equal to the net volume scaling of B. A correction factor was applied to R to scale the airways to their expected volume for a given lung volume. The expected positive scaling factor k_{VOL} at a given V_{VOL} is:

$$k_{VOL} = \left(\frac{V_{VOL} - V_{TLC}}{V_{MLV} - V_{TLC}} \right) \left(\left| \det\left(R_{TLC}^{MLV} \right) \right| - 1 \right) + 1 \qquad (5)$$

Multiplying a 3x3 matrix with a constant C results in an amplification of the determinant by C^3. The correct scaling C to yield a volume scaling of k_{VOL} is:

$$C = \left(\frac{k_{VOL}}{\left| \det\left(\hat{R}_{TLC}^{VOL} \right) \right|} \right)^{\frac{1}{3}} \qquad (6)$$

The scaling is done about the origin of the coordinate system and can cause the airways to change position. To counter this effect we add a displacement to the corrected affine that ensures that the corina (situated at TLC at point x_{corina}) does not move as a consequence of the scaling. One possible volume corrected affine parameterization is then:

$$B_{TLC}^{VOL} = \begin{bmatrix} C\hat{R}_{TLC}^{VOL} & \left((1-C)\hat{R}_{TLC}^{VOL} x_{corina} + d_{TLC}^{VOL} \right) \\ 0 \quad 0 \quad 0 & 1 \end{bmatrix} \qquad (7)$$

Note that this gives the desired scaling k_{VOL} at all positive lung volumes:

$$\left| \det\left(B_{TLC}^{VOL} \right) \right| = \left| \det\left(C^{\frac{1}{3}} \hat{R}_{TLC}^{VOL} \right) \right| = \left| \left(\left(\frac{k_{VOL}}{\left| \det\left(\hat{R}_{TLC}^{VOL} \right) \right|} \right)^{\frac{1}{3}} \right)^3 \det\left(\hat{R}_{TLC}^{VOL} \right) \right| = \left| k_{VOL} \right| = k_{VOL} \big|_{(k_{VOL} \geq 0)} \qquad (8)$$

The carina position also does not shift under the correction:

$$\begin{aligned} B_{TLC}^{VOL} \begin{bmatrix} x_{corina} \\ 1 \end{bmatrix} &= \begin{bmatrix} C\hat{R}_{TLC}^{VOL} & \left((1-C)\hat{R}_{TLC}^{VOL} x_{corina} + d_{TLC}^{VOL} \right) \\ 0 \quad 0 \quad 0 & 1 \end{bmatrix} \begin{bmatrix} x_{corina} \\ 1 \end{bmatrix} \\ &= \begin{bmatrix} \left(C\hat{R}_{TLC}^{VOL} x_{corina} + (1-C)\hat{R}_{TLC}^{VOL} x_{corina} + d_{TLC}^{VOL} \right) \\ 1 \end{bmatrix} = \begin{bmatrix} \hat{R}_{TLC}^{VOL} & d_{TLC}^{VOL} \\ 0 \quad 0 \quad 0 & 1 \end{bmatrix} \begin{bmatrix} x_{corina} \\ 1 \end{bmatrix} = \hat{B}_{TLC}^{VOL} \begin{bmatrix} x_{corina} \\ 1 \end{bmatrix} \end{aligned} \qquad (9)$$

Appendix III. Airway Surface Area and Volume:

The volume of the intrapulmonary central airways at TLC was found by counting the number of voxels within the airways. The surface area of the airways was estimated using the Apollo measurements of the lobar and segmental airways. Measurements of the diameter and length of the sub-segmental airways could not be

reliably made and these airways are not included in the surface measurement. The determinant of the affine operator gives the ratio of the airways' volume after transformation to that before transformation. We used this to scale the TLC airway volume to MLV. Similarly we used this factor raised to the 2/3 to scale the TLC airway area to MLV.

Chapter II: What Causes Uneven Aerosol Deposition in the Bronchoconstricted Lung? A Quantitative Imaging Study

Elliot Eliyahu Greenblatt MS [1,2], Tilo Winkler PhD[2], Robert Scott Harris MD[2], Vanessa Jane Kelly PhD [2], Mamary Kone MD[2], Ira Katz PhD [3,4], Andrew R. Martin PhD [5], George Caillibotte PhD [3], Jose Venegas PhD [2]

[1] *Mechanical Engineering, Massachusetts Institute of Technology, Boston, MA, USA*

[2]*Massachusetts General Hospital and Harvard Medical School, Boston, MA, USA*

[3]*R&D Medical, Air Liquide Santé International, Les-Loges-en-Josas, France*

[4] *Mechanical Engineering, Lafayette College, Easton, PA, USA*

[5]*Mechanical Engineering, University of Alberta, Edmonton, AB, Canada*

This chapter has been submitted to the Journal of Aerosol Medicine and Pulmonary Drug Delivery, and the text and figures are reproduced here with the permission of the publisher.

Abstract

Background: A previous PET-CT imaging study of 14 bronchoconstricted asthmatic subjects showed that peripheral aerosol deposition was highly variable among subjects and lobes. The aim of this work was to identify and quantify factors responsible for this variability.

Methods: A theoretical framework was formulated to integrate four factors affecting aerosol deposition: differences in ventilation, in how air and aerosol distribute at each bifurcation, in the fraction of aerosol escaping feeding airways, and in the fraction of aerosol reaching the periphery that is exhaled. These factors were quantified in 12 of the subjects using PET-CT measurements of relative specific deposition sD^*, relative specific ventilation sV^* (measured with dynamic PET or estimated as change in expansion between two static HRCTs), average lobar expansion F_{VOL}, and breathing frequency measured during aerosol inhalation f_N.

Results: The fraction of the variance of sD^* explained by sV^* (0.38), by bifurcation effects (0.38), and by differences in deposition along feeding airways (0.31) were similar in magnitude. We could not directly estimate the contribution of aerosol that was exhaled. Differences in expansion did not explain any fraction of the variability in sD^* among lobes. The dependence of sD^* on sV^* was high in subjects breathing with low f_N , but weakened among those breathing faster. Finally, sD^*/sV^* showed positive dependence on F_{VOL} among low f_N subjects while the dependence was negative among high f_N subjects.

Conclusion: The theoretical framework allowed us to analyze experimentally measured aerosol deposition imaging data. When considering bronchoconstricted asthmatic subjects, a dynamic measurement of ventilation is required to evaluate its effect on aerosol transport. The mechanisms behind the identified effects of f_N and F_{VOL} on aerosol deposition need further study and may have important implications for aerosol therapy in subjects with heterogeneous ventilation.

keywords: aerosol deposition, asthma, ventilation, escape fractions, sedimentation, bronchoconstriction

Introduction

The success of an inhaled therapy depends on the dose delivered to the lungs and regional deposition likely influences therapeutic effectiveness [18, 19]. We previously reported PET-CT measurements showing that deposition of inhaled aerosol in bronchoconstricted asthmatic subjects was heterogeneous. The pattern of deposition that we observed included both serial differences in the fraction of aerosol retained by the central airways feeding each lobe as well as parallel differences in the aerosol that deposited distal to these airways[7]. In the present work we seek to understand how serial differences in airway deposition couple with other factors to achieve the parallel heterogeneity in deposition of aerosol among lobes.

Given what is known about aerosol deposition, it is likely that most of the variability in peripheral aerosol deposition among lobes, sublobes, or any set of peripheral lung regions, can be attributed to four distinct factors: 1) differences in regional ventilation[13, 14, 18], 2) differences in how the aerosol and air distribute between branches in the series of bifurcations along the pathway feeding the region [14], 3) variability in the amount of the aerosol that escapes the series of airways along that pathway[53, 54], and 4) variability in the amount of aerosol that reaches the periphery and deposits (i.e. is not exhaled)[55]. Each of these mechanisms is described in greater detail below.

Because the aerosol particles are carried by airflow through the airway tree , heterogeneity in regional ventilation can generate heterogeneity in peripheral deposition[56]. When diseased regions are less ventilated than the rest of the lung, delivery of inhaled aerosol therapy may be reduced to areas where it may be most needed. For example, bronchoconstricted subjects with asthma might expect to receive lower local dose of inhaled bronchodilator or anti-inflammatory agents in ventilation defective regions. In the present work we compare the regional distribution of aerosol deposition among lobes against the corresponding distributions of ventilation estimated with two methods: one from the washout of a gas tracer during breathing as imaged with dynamic PET-CT, and the other inferred from the relative changes in volume between two lung inflation conditions as measured from static HRCT scans.

Heterogeneity in peripheral aerosol deposition may also occur due to differences in the concentration of aerosol reaching the periphery, even in lungs with uniform ventilation[56]. These concentration differences may develop by two distinct factors. One factor emerges at bifurcations when air and aerosol divide between daughter branches in unequal fractions. This may occur when aerosol entering the bifurcation is not well mixed within the cross section of the parent branch[14], or when the inertia of the aerosol particles prevents them from following the airflow in sharp turns.

The second factor influencing the concentration of aerosol reaching peripheral regions is the fraction of aerosol that deposits along the airways that feed them. Deposition within these airways, generally by inertial impaction, reduces the concentration of aerosol reaching the periphery. The extent of the deposition within airways can vary depending on local variations in air speed, velocity profiles, and airway tree morphometry[53, 54, 57].

In certain circumstances, not all of the aerosol escaping the central airways deposits in the periphery; small particles can remain in suspension and are exhaled[55, 58]. Differences among lobes in peripheral retention are thus considered as a fourth source of variable peripheral deposition among lobes.

In this chapter we integrate these four factors into a theoretical framework that describes the processes of transport and deposition of an inhaled aerosol along the airway tree to the periphery. Using this framework we evaluate the influence of each factor based on PET-CT imaging data of lung anatomy, aerosol deposition, and ventilation in bronchoconstricted asthmatic subjects. The unique richness of the combined PET and CT images presented here allows this information to be evaluated for the first time. The theoretical framework yields lobar indices of the sources of variability that can be used to validate the clinical applicability of patient specific numerical models of aerosol deposition.

Nomenclature

peripheral	Airways and lung tissue beyond the subsegmental airways
central	The central airways up to and including the subsegmental airways
x_s , x_{sl}	The subscript *s* indicates the value *x* changes with subject, and the subscript *sl* indicated that the value x changes with both subject and lobe
sD_{sl} , $\overline{sD_s}$, sD_{sl}^*	The specific deposition in the periphery of a lobe, the subject average specific deposition, and the non-dimensional ratio of $sD_{sl} / \overline{sD_s}$
$s\dot{V}_{sl}$, $\overline{s\dot{V}_s}$, $s\dot{V}_{sl}^*$	The specific ventilation of a lobe, the average specific ventilation of a subject, and the non-dimensional ratio of $s\dot{V}_{sl} / \overline{s\dot{V}_s}$

$\varepsilon_{I,x}$, $\varepsilon_{S,x}$, $\varepsilon_{D,x}$	The escape fractions of aerosol passing location x in inhalation of the aerosol due to impaction, sedimentation, and diffusion
η_x , η_{sl}, $\overline{\eta_s}$, η_{sl}^*	The fraction of aerosol passing location x during inhalation of the aerosol that is not exhaled, that fraction for a given lobe, for a given subject, and the non-dimensional ratio of $\eta_{sl} / \overline{\eta_s}$
$\eta_{carina,sl}$, $\eta_{carina,s}$	The retention factor of aerosol passing the carina along a pathway leading to a specific lobe, or to the entire lung
C_x, C_{sl}, $C_{carina,\,s}$	The concentration of the aerosol in air at: location x in the airway tree, entering into the periphery of a given lobe, passing the carina of a given subject
D_x, V_x,	The cumulative aerosol that deposits past location x in the airway tree during inhalation, and the cumulative volume of air that passes that location during inhalation
B_k	The branching factor of airway k. Describes the change of concentration between the terminus of the parent airway and the airway entrance during inhalation if the aerosol
E_k	The escape fraction of airway k. Describes the change of concentration along an airway k during inhalation of the aerosol
$\Pi_{B.sl}$, $\overline{\Pi_{B,s}}$, $\Pi_{B.sl}^*$ $\hat{\Pi}_{\mathrm{B},sl}^*$	The net branching factor of a given lobe, the average for a subject, the ratio of $\Pi_{B.sl} / \overline{\Pi_{B,s}}$, and this value estimated with complete retention
$\Pi_{E,sl}$, $\overline{\Pi_{E,s}}$, $\Pi_{E.sl}^*$ $\hat{\Pi}_{E,sl}^*$	The net escape fraction of a given lobe, the average for a subject, the ratio of $\Pi_{E,sl} / \overline{\Pi_{E,s}}$ and this value estimated with complete retention
g_{sl}^* , h_{sl}^*	Factors of η_{sl}^* that independently effect $\hat{\Pi}_{E,sl}^*$ and $\hat{\Pi}_{\mathrm{B},sl}^*$
$t_{N,s}$	The nebulization time for a given subject
$D_{0,s}$, $D_{E,s}$, $D_{T,s}$, $D_{P,s}$, $D_{C,s}$	The total aerosol arriving at the carina, the exhaled fraction, the total deposited the peripheral deposition, and the central deposition of a given subject. With a subscript *sl,* it is of a given lobe
$\dot{V}_{T,s}$, V_s	The total average rate and volume of gas passing the carina of a given subject during inhalation

$V_{L,s}$	The subject lung volume
ψ_{sl}	The set of airways feeding a given lobe
S	The set of all lobes of all subjects
sI_{sl}, $\overline{sI_s}$, sI^*_{sl}	The specific inflation of a lobe, the subject average specific ventilation, and the non-dimension ratio of the $sI_{sl} / \overline{sI_s}$
MLV,TLC	The mean lung volume during tidal breathing, and total lung capacity
$I_{T,s}$	The total change in gas volume from the *MLV* to *TLC* HRCT image
K_{sl}	A factor that accounts for segmentation differences and the change in blood volume between the *MLV* to *TLC* HRCT images
$f_{\dot{V},sl}$	The fraction of subjects ventilation reaching a given lobe
d_s, v_s, t_s	The distance a particle would sediment, the settling velocity, and the settling time
Q_N	The inhalation flow rate
$F_{VOL,sl}$	The degree of expansion of a lobe (the gas volume/the non-gas volume)
$V_{Gas,MLV,sl}$, $V_{Tissue,MLV,sl}$	The gas and non-gas (tissue and blood) volumes estimated for a given lobe in the *MLV* image. A subscript of *TLC* indicates that this was taken from the *TLC* image, and a subscript of *s* (or *T)* indicates that is volume of the entire lung
f_N	The breathing frequency of a given subject during inhalation
FEV_1	Forced expiratory volume in 1 second after a deep inhalation
FVC	Functional vital capacity

Methods

We begin by introducing a general theoretical framework that describes deposition in terms of four distinct parameters that can vary among lobes. Subsequently, we describe the imaging

protocol and the means of evaluating these parameters in a group of bronchoconstricted asthmatic subjects.

Theoretical Framework

Overview

In this section we define a general framework that may be used to isolate sources of variable deposition among lobes, or any other region of the lung periphery that is subtended by a unique airway. We begin by defining appropriate measures of deposition and ventilation that are not sensitive to differences in volume among lobes, and introduce the notions of retention fraction and aerosol concentration. We identify two factors that can influence the concentration along each airway and identify the net contribution of each factor to differences in aerosol deposition among lobes. We then collect all sources of variability into a single expression that describes lobar deposition in Eq. (15). To better compare these sources of variability across different subjects, we account for differences in overall dosing, lung size, centrality of deposition, and restate the expression in non-dimensional, normalized form in Eq. (18). After several simplifications, we decouple the sources of variability in Eq. (24).

Lobar Measures of Deposition and Ventilation

Deposition beyond the sub-segmental airways within a lobe can be characterized by a specific deposition sD_{sl}, where the subscript *s* indicates the subject studied and the subscript *l* indicates the lobe (or any other lung region). In this chapter, regions beyond the sub segmental airways are referred to as peripheral regions, while more proximal regions are referred to as central airways. sD_{sl} is defined as the aerosol deposition with a lobe's periphery normalized by the total volume of the lobe measured at the mean lung volume during the subjects' tidal breathing (MLV). The specific deposition allows for meaningful comparisons between lobes of different volumes.

The ventilation of a lobe or lung region is similarly characterized by its regional specific ventilation $s\dot{V}_{sl}$, defined as the ventilation of the region per unit total volume at MLV to allow comparisons between these variables and among lobes or regions of different sizes.

Retention Fraction and Aerosol Concentration

The retention fraction η_x of a location x along the airways is the fraction of the total aerosol that passes that location during inhalation that deposits. When ventilation data is acquired in conjunction with the deposition data, the concentration C_x of aerosol in the inhaled air can be evaluated at any location x along the airway tree. This is the average concentration along the cross section during inhalation of the aerosol, and is the ratio of aerosol to air volume that passed that location. The aerosol that passed the location is found by dividing the total deposition that deposited distal to that location D_x with the retention fraction of that location η_x (to account for exhaled aerosol that did not deposit). For a cumulative volume of air V_x passing location x during inhalation:

$$C_x = \frac{D_x}{\eta_x V_x} \quad \textbf{(10)}$$

Note the units of the concentration will be aerosol per unit volume of air. The aerosol itself can be described in terms of mass, volume, or number of particles.

Individual Airway Branching Factors and Escape Fractions

When the airflow and the aerosol entering into a bifurcation split differently between daughter branches, the aerosol concentration entering a daughter the kth airway $C_{airway\ k,\ ent.}$ is no longer equal to the aerosol concentration leaving the parent airway $C_{parent\ k,exit}$. We can therefore define a Branching Factor B_k for an airway k as:

$$B_k = \frac{C_{airway\ k,ent.}}{C_{parent\ k,exit}} \quad \textbf{(11)}$$

Thus a value of $B_k \neq 1$ quantifies a change in aerosol concentration between mother and daughter airways (Figure 1).

A second factor affecting the concentrations is the aerosol deposition along airways; as aerosol deposits along an airway wall, the concentration of aerosol in suspension is reduced[53]. The concentration of the aerosol leaving an airway, $C_{airway\ k,\ exit}$, and that entering it, $C_{airway\ k,\ ent.}$ (Figure 1), can be used to define an escape fraction, E_K, as the ratio of these concentrations:

$$E_k = \frac{C_{airway\ k,exit}}{C_{airway\ k,ent.}} \tag{12}$$

Note that because the volume of air entering and exiting an airway is identical, the escape fraction can be determined without knowing the ventilation. By combining equations (11) and (12), it can be shown that the product of B_k and E_k is the ratio of $C_{airway\ k,\ exit}$ to $C_{parent\ k,\ exit}$:

$$B_k E_k = \frac{C_{airway\ k,exit}}{C_{parent\ k,exit}} \tag{13}$$

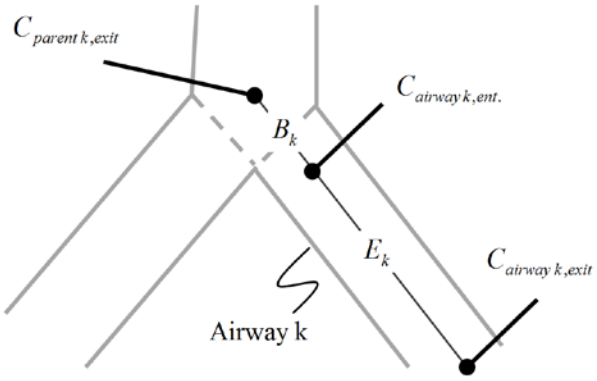

Figure 1: Concentration changes at a bifurcation and along an airway k are characterized by two transitions; B_k captures the change in concentration at the inlet of the airway, and E_k captures the change in concentration along an airway.

Net Branching Factors and Net Escape Fractions

The path between the carina and the periphery of each lobe includes a series of bifurcations and airways that partition and trap the aerosol. For a lobe of a subject we can calculate the ratio of average aerosol concentrations between that leaving the sub-segmental airways of that lobe C_{sl} to that entering the tracheal carina $C_{carina,s}$. Thus, for a set of airways ψ_{sl} leading to a specific lobe of given subject the net escape fraction can be written in terms of the product of branching factor and escape fractions:

$$\frac{C_{sl}}{C_{carina,s}} = \prod_{j\in\psi_{sl}} B_j E_j = \prod_{j\in\psi_{sl}} B_j \prod_{k\in\psi_{sl}} E_k = \Pi_{B.sl}\Pi_{E,sl} \tag{14}$$

Note that the product $\Pi_{B.sl}$ is a net branching factor that characterizes the effect of the mismatch between air and aerosol division at bifurcations on the lobar aerosol concentration. Similarly, the product $\Pi_{E,sl}$ is a net escape fraction that characterizes the effect of aerosol deposition within the airways along the pathway to the lobe. Note that to evaluate either of these metrics, the individual values of B_k and E_k of each airway along the pathway must first be evaluated.

Expressing Specific Deposition in Terms of Sources of Variability

The lobar specific deposition of aerosol of subject *s* in lobe *l* is therefore:

$$sD_{sl} = t_{N,s} s\dot{V}_{sl} C_{carina,s} \Pi_{B.sl} \Pi_{E,sl} \eta_{sl} \quad \textbf{(15)}$$

The term $t_{N,s} s\dot{V}_{sl}$ corresponds to the cumulative volume of air that reached the periphery of the lobe during nebulization (normalized by the total volume of the lobe). The term $C_{carina,s} \Pi_{A.sl} \Pi_{E,sl}$ corresponds to the concentration of aerosol entering the lobe periphery C_{sl}, explicitly expressed in terms of the two factors influencing it. The product of the normalized volume of air and its aerosol concentration yields the cumulative aerosol delivered to the lobar periphery (per unit volume of lobe), and when multiplied by the fraction that is not exhaled η_{sl}, we arrive at sD_{sl}. Note that since the nebulization time $t_{N,s}$ and $C_{carina,s}$ are constants for a given subject, the four remaining terms express the sources of variability of specific deposition among lobes for a given subject.

Rearranging into Non-Dimensional Form

A non-dimensional form for Eq. (15) can be used to compare data from subjects with different lung sizes who received different aerosol doses, different overall ventilation and deposition, and have different degrees of overall central deposition. It is also desirable to have the non-dimensional variables vary about unity to simplify the analysis as is discussed below. Let us first describe the total aerosol passing a subject's carina $D_{0,s}$ as the sum of the deposited aerosol past the carina $D_{T,s}$ and the exhaled aerosol $D_{E,s}$. $D_{T,s}$ itself can be expressed as the sum of the deposition in the periphery $D_{P,s}$ and that in central airways $D_{C,s}$:

$$D_{0,s} = D_{T,s} + D_{E,s}, \text{ and } \; D_{T,s} = D_{P,s} + D_{C,s} \tag{16}$$

Using this we can expand the concentration at the carina using the definition of concentration given in Equation (10), rewritten in terms of the total deposition beyond the carina $D_{T,s}$ and the total average inspiratory flow through the carina $\dot{V}_{T,s}$:

$$C_{carina,s} = \frac{D_{carina,s}}{\eta_{carina,s} V_{carina,s}} = \frac{D_{T,s}}{\eta_{carina,s} \dot{V}_{T,s}} \frac{1}{t_{N,s}} = \frac{D_{0,s}}{\dot{V}_{T,s}} \frac{1}{t_{N,s}} \tag{17}$$

After substituting this relationship into Eq. (15), a dimensionless form can be obtained by rearranging the terms and dividing by the total lung volume $V_{L,s}$, and by $D_{P,s} / D_{T,s}$:

$$sD_{sl}^{*} = s\dot{V}_{sl}^{*} \Pi_{B.sl}^{*} \Pi_{E,sl}^{*} \eta_{sl}^{*} \tag{18}$$

Here the dimensionless specific deposition and ventilation are:

$$sD_{sl}^{*} = \frac{sD_{sl}}{\overline{sD_s}} = \frac{sD_{sl}}{D_{P,s}/V_{L,s}}; \quad s\dot{V}_{sl}^{*} = \frac{s\dot{V}_{sl}}{\overline{s\dot{V}_s}} = \frac{s\dot{V}_{sl}}{\dot{V}_{T,s}/V_{L,s}} \tag{19}$$

These are the specific deposition of each lobe normalized by the specific deposition in the entire periphery of each subject $\overline{sD_s}$, and the specific ventilation of each lobe normalized by the specific ventilation of the entire lung for each subject $\overline{s\dot{V}_s}$. Lobar values for these numbers for each subject distribute about unity. The already dimensionless product $\Pi_{B.sl}$ is normalized by the ventilation weighted lung average for each subject $\overline{\Pi_{B,s}}$. Thus, if $f_{\dot{V},sl}$ is the fraction of a subject's ventilation that is delivered to a lobe, we have that:

$$\Pi_{B.sl}^{*} = \frac{\Pi_{B.sl}}{\overline{\Pi_{B,s.}}} = \frac{\Pi_{B.sl}}{\sum_j f_{\dot{V},sj} \Pi_{B.sj}} = \Pi_{B.sl} \tag{20}$$

Note that the ventilation weighted average of $\Pi_{B.sl}$ is unity because the branching factors do not provide a mechanism for deposition and therefore conserve the total amount of aerosol. Similarly, the already dimensionless $\Pi_{E,sl}$ has been normalized by the average escape fraction of the of the airway tree $\overline{\Pi_{E,s}}$ for each subject:

$$\Pi^*_{E.sl} = \frac{\Pi_{E.sl}}{\overline{\Pi_{E,s}}} = \frac{\Pi_{E.sl}}{\frac{D_{P,s} + D_{E,s}}{D_{O,s}}} \quad \textbf{(21)}$$

Finally, the retention fraction of each lobe has been normalized by the retention of the entire periphery of each subject $\overline{\eta_s}$:

$$\eta^*_{sl} = \frac{\eta_{sl}}{\overline{\eta_s}} = \frac{\eta_{sl}}{\frac{D_{P,s}}{D_{P,s} + D_{E,s}}} \quad \textbf{(22)}$$

Decoupling Sources of Variability

Taking the log of equation (18) transforms the product of effects into a sum of effects. Given that all the variables have been defined to vary about unity, we can further approximate the logarithm with the first order Taylor expansion of the logarithm about unity (log(x)≈x-1)), Eq. (18) can then be approximated as:

$$sD^*_{sl} \approx sV^*_{sl} + \Pi^*_{B,sl} + \Pi^*_{E,sl} + \eta^*_{sl} - 3 \quad \textbf{(23)}$$

In the specific case where these four effects are independent (i.e. there is weak covariance among the terms) we arrive at a decomposition of the variance in specific deposition in terms of the variance of the four factors that independently influence it. For the set *S* of all lobes among all subjects:

$$\underset{j\in S}{\text{var}}\left(sD^*_j\right) \approx \underset{j\in S}{\text{var}}\left(sV^*_j\right) + \underset{j\in S}{\text{var}}\left(\Pi^*_{B,j}\right) + \underset{j\in S}{\text{var}}\left(\Pi^*_{E,j}\right) + \underset{j\in S}{\text{var}}\left(\eta^*_j\right) \quad \textbf{(24)}$$

This final equation allows us to estimate the fraction of the variance that comes from each of the four factors.

Experimental Methods

Overview

This section describes the imaging technique, and the method to extract the abovementioned parameters in a group of bronchoconstricted asthmatic subjects from PET-CT images of ventilation and aerosol deposition.

Imaging Protocol

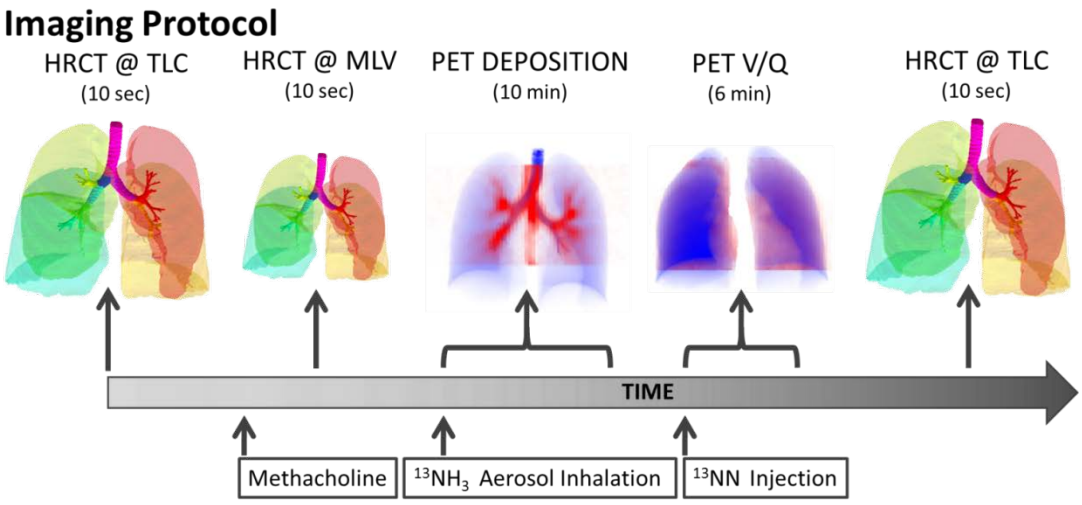

Figure 2: The imaging protocol sequence.

The imaging protocol was completed at Massachusetts General Hospital with IRB approval (Application No. 2007P000493). 12 asthmatic subjects were imaged with PET-CT (Biograph 64; Siemens AG). The subjects were young (average 20.1 years), predominantly female (3 male and 9 female) and not obese (BMI's less than 32 Kg/m^2). All subjects had mild intermittent or mild persistent asthma as defined by the NIH Global Initiative for Asthma [35] with FEV_1 and FVC ≥ 80% predicted, fewer than daily symptoms, and peak flow or FEV_1 variability of less than 30%. All

subjects demonstrated reversible obstruction with inhaled albuterol (≥ 12% on previous spirometry).

During an initial screening visit the concentration of methacholine (MCh) required to cause a 20% drop in the subjects FEV_1 (PC_{20}) was estimated. On a second visit that same concentration was administered with five deep breaths of methacholine aerosolized by a DeVilbiss nebulizer and Rosenthal dosimeter (model 646, DeVilbiss Healthcare, Somerset, PA) with the subject in the supine position in the PET-CT camera. Three HRCT images were obtained during breath hold: one at total lung capacity (TLC) before bronchoconstriction, a second at mean lung volume (MLV) approximately 5 minutes after bronchoconstriction, and a final HRCT at TLC approximately 30 minutes after the MCh challenge.

To monitor lung volume and guide its value during imaging, a real time trace of instantaneous volume was obtained with an inductance plethysmograph (RIP) (SomnoStar PT, SensorMedics Corp, Yorba Linda, CA) and presented to the subject through video goggles. When imaging the lung at MLV with HRCT, the subject was instructed to stop breathing and hold his/her breath when the trace reached a line defining their MLV (previously determined during a 30 second window of spontaneous breathing before the scan).

After the MLV HRCT image (16 +/- 5 minutes after the MCh challenge), an aerosol of $^{13}NH3$ labeled isotonic saline was generated with a vibrating mesh nebulizer (Aeroneb Solo, Aerogen , Galway, Ireland) and delivered via an Idehaler holding chamber (Aerodrug, Cedex, France) into the mouthpiece through which the subject was breathing while wearing a nose clip. The aerosol reaching the mouthpiece was previously characterized by laser diffraction as having an approximately lognormal distribution with a median aerosol diameter of 4.9μm and a geometric standard deviation of 1.8 (4.9 μm VMD with a GSD of 1.8). This indicates that approximately 95% of the aerosol volume was between 1.5 and 15 μm[36]. While the subjects were supine in the PET-CT camera, intrapulmonary aerosol deposition was imaged with dynamic PET during the 2-minute period of inhalation and the following 8 minutes of spontaneous breathing.

After the end of the deposition image collection (30 +/- 5 minutes post MCh) regional specific ventilation was assessed during a V/Q scan from the washout of a bolus of ^{13}NN gas as

described in detail elsewhere[59]. Briefly, during a V/Q scan nitrogen (^{13}N-N) in saline solution was injected intravenously as a bolus during apnea. The poorly soluble radioactive nitrogen gas diffuses from the plasma to the alveolar airspace resulting in an intrapulmonary tracer distribution proportional to that of regional pulmonary blood flow. Following a 20 second breath hold, the subject resumes breathing and the washout of the tracer is used to determine regional specific ventilation.

In 9 of these 12 subjects, we were also able to estimate the breathing frequency during aerosol inhalation from the RIP signal; the data from the first three subjects was recorded on an older laptop, and the signals could not be recovered.

Evaluating Deposition and Ventilation from the Images

The PET images were analyzed to quantify the anatomical location of the aerosol deposition and the alveolar ventilation. The local tracer from the deposition images was assigned to anatomical regions (ARs) using the Grayscale method previously developed [7]. This technique allowed quantification of aerosol deposition within anatomically defined portions of the central airway tree (CA) and on distal regions fed by them, after accounting for blurring of the PET image due to breathing motion, limited spatial resolution of PET, and PET-CT co-registration uncertainties. Using Apollo™ software (Vida Diagnostics, Mountain View, CA) the lung was segmented into 14 ARs, including 5 peripheral lobar regions and 9 segments of the airway tree. The lung periphery included the five lobes; left upper lobe (LUL), left lower lobe (LLL), right upper lobe (RUL), right middle lobe (RML), and right lower lobe (RLL). Central airways included the bronchus intermedius (BINT), the right and left main bronchus (RMB and LMB) and the trachea (TRC), as well as 5 lobar central airway trees feeding each lobe that included the lobar, segmental and sub segmental airways.

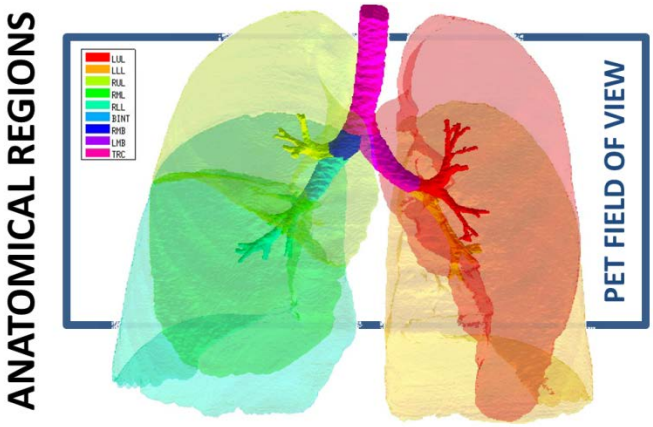

Figure 3 : Rendering of the 14 anatomically consistent regions (ARs) used in this study. The lobar central airways are color matched to the lobes that they feed. The 16cm PET field of view and the typical placement of the PET image are shown with the rectangle. The PET field of view typically covers 83±8% of the lung volume, with 4±3% missing from the apex, and 13±7% missing from the base.

The distribution of deposition throughout the lung and airways was described as the relative specific deposition sD_{sl}^{*} . Note that the radionuclide concentration of the aerosol must be known to evaluate sD_{sl} from the activity within the image. However, once normalized by the average specific deposition $\overline{sD_s}$ (as in sD_{sl}^{*}), the *relative* depositions can be determined directly from the relative activities in the image.

The relative distribution of ventilation during aerosol inhalation was assumed to be equal to that measured during the subsequent ^{13}NN washout during the V/Q scan. Voxel by voxel ventilation was estimated from the best model chosen by the Akaike Information Criterion[59] among a 2-compartment model, a one compartment model, a partial gas trapping model, and a full gas trapping model. Net alveolar ventilation for each lobe was estimated as the sum of voxel products of compartment's turnover rate times its gas volume. The gas volume in each compartment within a voxel was estimated by the gas content of the voxel (measured from the CT scan at MLV) multiplied by the fraction of perfusion of the voxel that was delivered to that compartment. The voxel by voxel estimates were then distributed among lobes based on how each lobe contributed to the activity in that voxel [7]. The total ventilation of the lobe is divided by the lobe volume to identify the specific ventilation $s\dot{V}_{sl}$. Dividing by the average specific ventilation among all lobes in the subject yielded $s\dot{V}_{sl}^{*}$. Note that although this is a measure of relative *alveolar* specific ventilation, if the deadspace

ventilation distributes in a similar way as the fresh gas[60], this is also a measure of relative total specific ventilation.

Estimating Specific Inflation from 2 HRCTs

An alternative estimate of lobar ventilation distribution, similar to one used in previous studies [60, 61], uses the change in lobar volume between two static HRCT scans from MLV to TLC as a proxy for the ventilation during tidal breathing. The specific inflation sI_{sl}^{*} was therefore:

$$sI_{sl} = \frac{V_{TLC,sl} - V_{MLV,sl}K_{sl}}{V_{MLV,sl}K_{sl}} \quad \textbf{(25)}$$

Where the *V* terms are the different total lung volumes post constriction and K_{sl} is a number close to 1 that corrects for lobar segmentation differences of the lobe between the two images. Under the assumption that differences in the tissue volume of a perfectly segmented lobe should not differ between the two images, and that changes in blood volume can be estimated from the entire lung. K_{sl} can be expressed in terms of the blood and tissue volumes V_{Tissue} of the lobes and lungs:

$$K_{sl} = \left(\frac{V_{Tissue,TLC,sl}}{V_{Tissue,MLV,sl}}\right) * \left(\frac{V_{Tissue,MLV,Total}}{V_{Tissue,TLC,Total}}\right) \quad \textbf{(26)}$$

A dimensionless form for sI_{sl}^{*} is obtained by normalizing by the average lung specific inflation $\overline{sI_s}$, or the total lung inflation $I_{T,s}$ divided by the MLV lung volume:

$$sI_{sl}^{*} = \frac{sI_{sl}}{\overline{sI_s}} = \frac{sI_{sl}}{I_{T,s}/V_{L,s}} \quad \textbf{(27)}$$

Estimating Lobar Retention Fractions

Lobar retention fractions could not be directly estimated from our data, nor were there values in the literature that could be directly used. However, based on global lung bolus retention data presented by Kim et al. [55], we could estimate a global retention fraction of the periphery $\overline{\eta_s}$ as a function of the settling distance d_s (see details in Appendix I). A general relationship could be derived that explained 97% of the variance in the measured peripheral retention fraction among 9

experiments with varying particle sizes and flow rates (Figure 4). Given the settling distance d_s that a particle of a given diameter would descend at the Stokes settling velocity v_s during the average residence time in the periphery t_s, we found that the retention fraction could be described by the equation:

$$\overline{\eta_{fit}} = 1 - e^{-\frac{d_s}{371\mu m}} \text{, where } d_s = v_s t_s \quad \textbf{(28)}$$

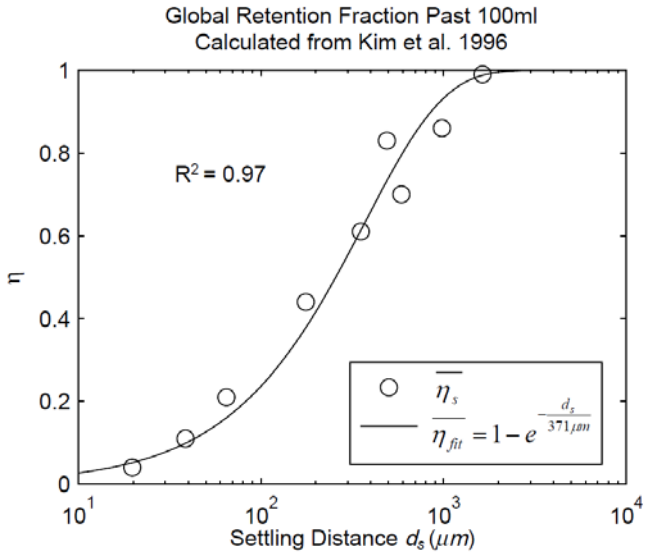

Figure 4: The global retention fraction estimated from the sequential bolus data presented in Kim et al.[55] versus the settling distance.

Evaluating $\overline{\eta_s}$ for the polydisperse aerosols used in our study showed that we can expect those subjects breathing at the highest frequencies during nebulization f_N should show approximately 20 to 60% lower average retention. The value of $\overline{\eta_s}$ was highly sensitive to proximal filtering effects; when larger aerosols are selectively filtered in the upper and central airways, the retention fraction of the periphery is significantly reduced (Figure 5).

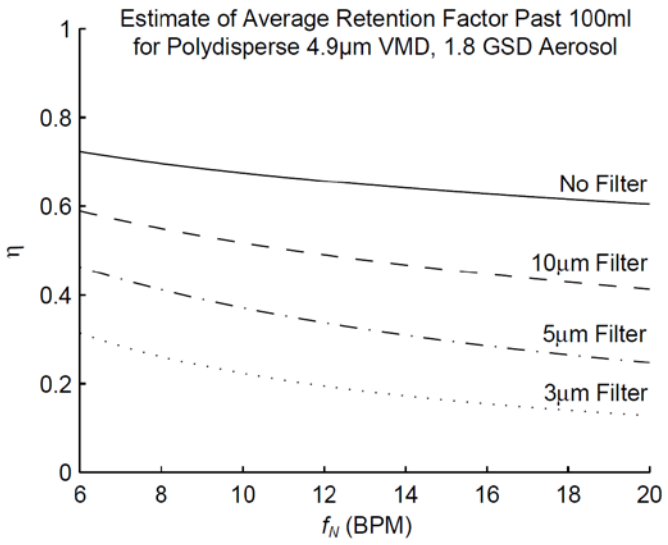

Figure 5: Estimates of the global retention in the lobar periphery for the polydisperse aerosols used in this study. The different lines describe different extents of proximal filtering of the larger sized aerosols; 'No Filter' assumes that the aerosol distribution entering the periphery is identical to the distribution at the mouth, while the filtered estimates assume that all particles above the filter size have already been deposited in the upper airways.

While this population averaged and lung averaged data can provide a useful estimate of the degree of average retention among all lobes, lobar retention fractions may vary substantially between subjects and lobes. For example, expanded lobes may have reduced η_{sl} due to both the longer sedimentation distances and lower likelihood of impaction in the distended airways. The expansion of a lobe $F_{VOL,sl}$ can be defined as the total volume of gas V_{gas} per unit of tissue and blood volume V_{Tissue} in a lobe at MLV:

$$F_{VOL,sl} = \frac{V_{Gas,MLV,sl}}{V_{Tissue,MLV,sl}} \tag{29}$$

Assessment of both f_N and $F_{VOL,sl}$ may provide insight into retention fraction effects.

Apparent Net Branching Factor and Escape Fraction

The net branching factor $\Pi^*_{\text{B},sl}$ and net escape fraction $\Pi^*_{E,sl}$ are both functions of changes in aerosol concentration along the airway tree and are thus intricately coupled with the lobar retention fractions. If these parameters are evaluated under the assumption of complete deposition in all lobes, an *apparent* net branching factor $\hat{\Pi}^*_{\text{B},sl}$ and apparent net escape fraction $\hat{\Pi}^*_{E,sl}$ are

obtained. Appendix II demonstrates that if $\eta_{carina,sl}$ is defined as the retention fraction of a specific lobar pathway at the carina, then the *apparent* branching factor and *apparent* escape fraction have the following relationship with the actual values:

$$\frac{\hat{\Pi}^*_{B,sl}}{\Pi^*_{B,sl}} = \frac{\eta_{carina,sl}}{\eta_{carina,s}} = h^*_{sl} \text{ and } \frac{\hat{\Pi}^*_{E,sl}}{\Pi^*_{E,sl}} = \frac{\eta_{sl}/\eta_{carina,sl}}{\overline{\eta_s}/\eta_{carina,s}} = g^*_{sl} \quad \textbf{(30)}$$

Note that g^*_{sl} and h^*_{sl} are both dimensionless terms that both distribute around 1 and combine to form the lobar retention fraction η^*_{sl} :

$$\eta^*_{sl} = g^*_{sl} h^*_{sl} \quad \textbf{(31)}$$

In this chapter we will present the apparent parameters as a proxy for the actual factors, noting that they differ from the actual factors by the g^*_{sl} and h^*_{sl} factors defined in equation (30).

The apparent branching factors can be evaluated from PET-CT deposition and ventilation images for the first four bifurcations in the airway tree (Figure 6) by setting η_x as unity throughout the airway tree. The apparent escape fractions can be similarly calculated up to the lobar central airways. Due to the limited spatial resolution of PET, proximal airways within each lobe, up to the sub-segmental airways, had to be lumped into a single compartment with an average lobar escape fraction.

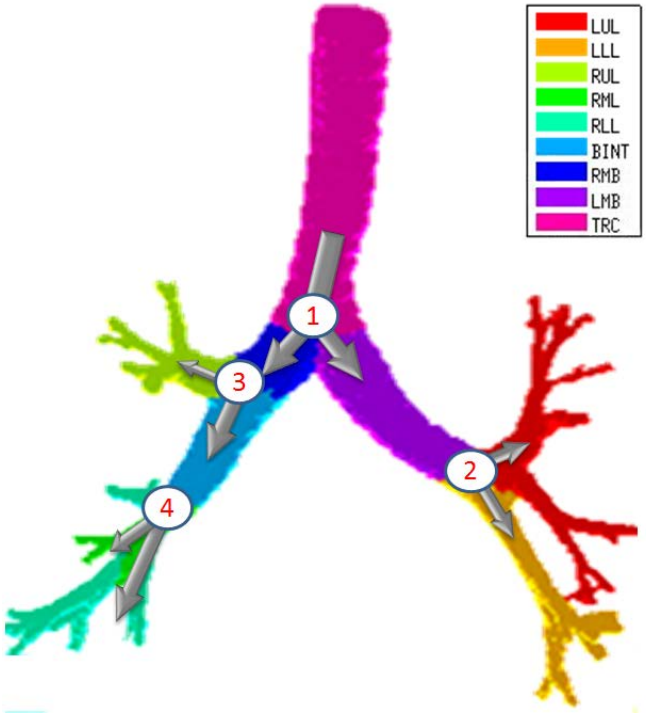

Figure 6: The four bifurcations in which the changes in concentration between the parent and daughter can be evaluated using PET-CT. These bifurcations are at the terminal ends of 1) the trachea, 2) the left main bronchus, 3) the right main bronchus, and 4) the bronchus intermedius.

Statistical Analysis

Systematic Differences Among Lobes in sD_{sl}^{*}, $sD_{sl}^{*} / s\dot{V}_{sl}^{*}$, and $\hat{\Pi}_{E,sl}^{*}$, were tested using ANOVA with repeated measures. When differences were evident at the 5% alpha level, a Holm-Sidak test for multiple comparisons was used to test for individual differences between lobes [39]. It should be noted that no further correction was made for the different ways that we divided and explored our data; all statistics are therefore exploratory and only intended to guide future studies. Variability in sD_{sl}^{*} and $s\dot{V}_{sl}^{*}$ was characterized using the average coefficient of variation among lobes for each subject (COV_{Lobes}), and using the COV among subjects for each lobe ($COV_{Subjects}$).

Results

Typical Deposition Pattern

PET-CT measurement of the aerosol deposition showed a highly centralized pattern of deposition in the present data set, with 33 +/- 6% of the aerosol entering the carina depositing in

the airways up to and including the sub-segmental generation. The maximum intensity projections for a typical subject are presented in Figure 7.

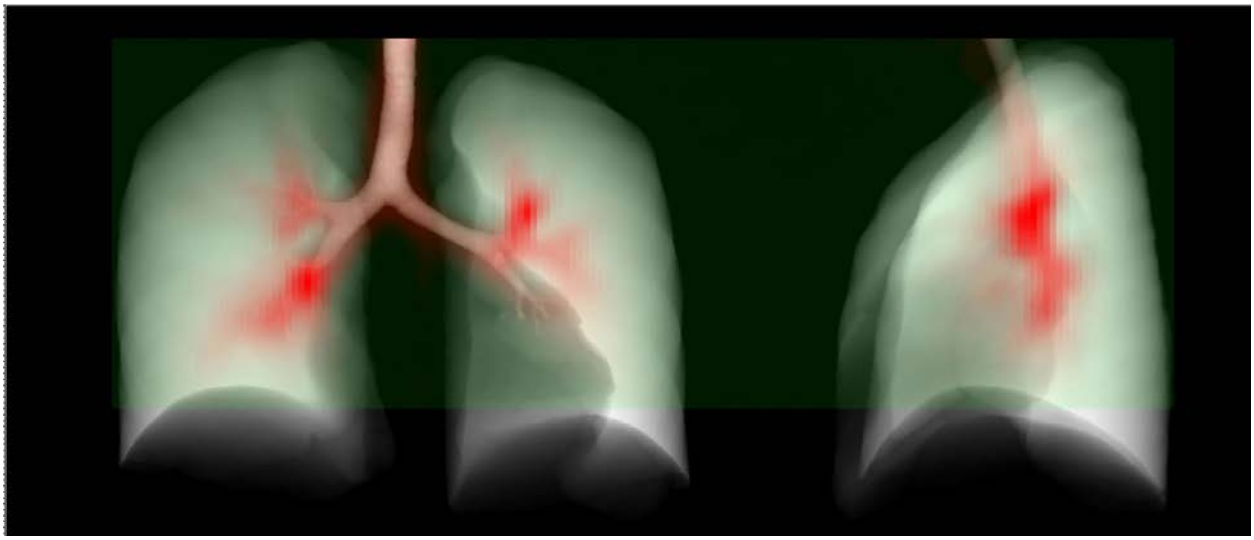

Figure 7: Maximum intensity projections of the highly central deposition pattern of one typical subject in the current data. In the left projection the right lung is on the left. In the right projection the back of the supine subject is to the right of the image.

Relationship Between sD* and sV*

A global correlation between lobar ventilation and deposition for the group of subjects was found by pooling the non-dimensional results for all lobes of all subjects (Figure 9, *left*). The distribution of $s\dot{V}_{sl}^{*}$ correlated with the distribution of sD_{sl}^{*} (*Corr*(*sD*,sV**) = 0.62 , P(*Corr*. <0) < 0.0001). The strength of subject by subject relationships varied, and these are shown in Figure 8. The average Correlation coefficients $Corr(sD^*,sV^*)_s$ was 0.51 ± 0.29, with the subjects breathing at slower frequencies during the aerosol nebulization f_N having higher correlations between $s\dot{V}_{sl}^{*}$ and sD_{sl}^{*} than those breathing faster ($Corr(Corr(sD^*,sV^*)_s,f_N)$ = -0.71, P(*Corr*. < 0) = 0.032). Additionally, subjects presenting lower inter-lobar variability in deposition or ventilation, tended to yield poor ventilation-deposition correlations (Figure 8).

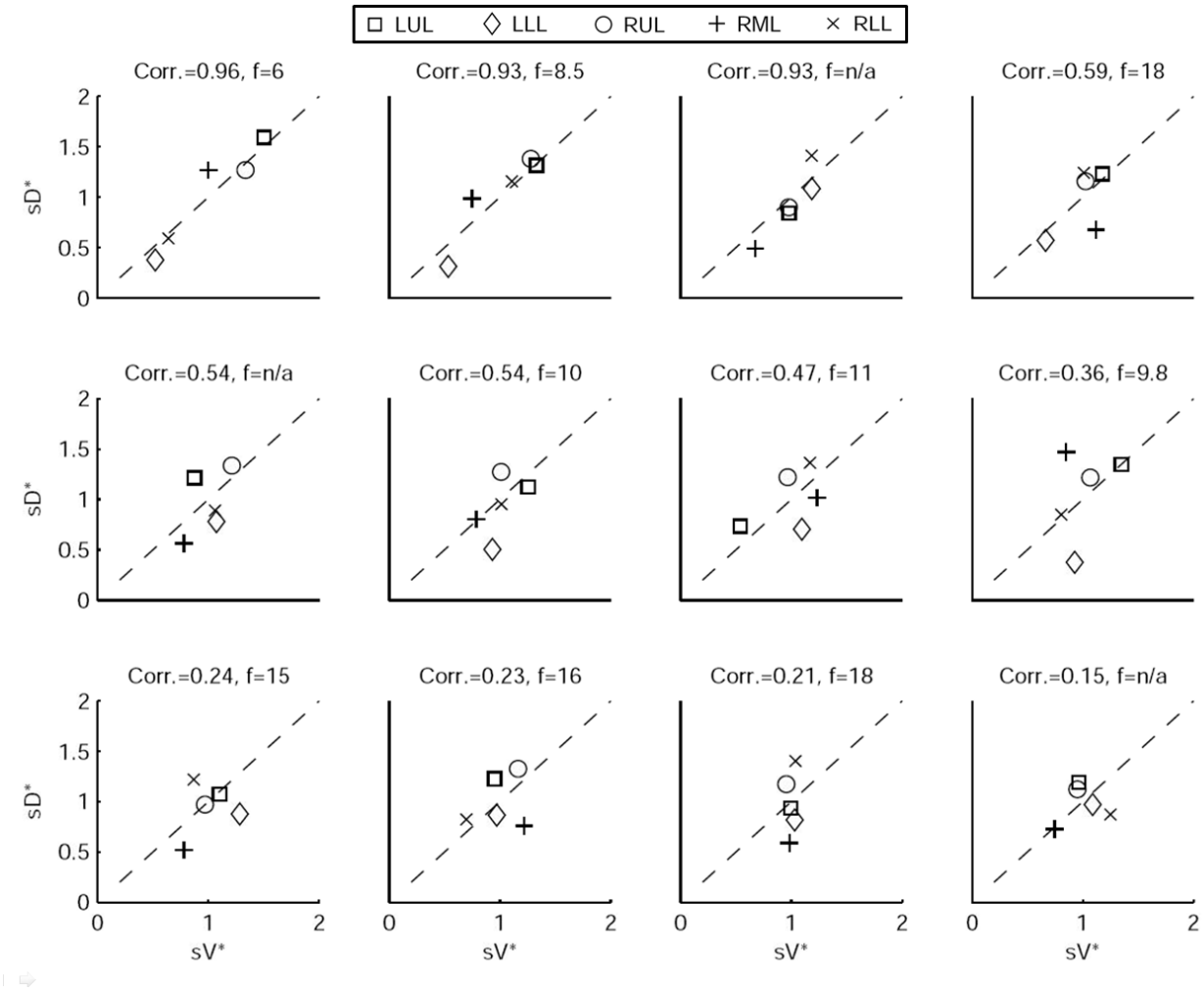

Figure 8: Subject-by-subject specific deposition vs. specific ventilation, organized by strength of thec. The breathing frequency during nebulization in breaths per minute is also shown in each figure caption.

Relationship Between sD* and sI*

We further compared the distribution of sI_{sl}^{*} (derived from two static CT images at MLV and TLC) and sD_{sl}^{*}. In contrast with $s\dot{V}_{sl}^{*}$, there was no significant correlation between normalized sD_{sl}^{*} and normalized sI_{sl}^{*} for the pooled lobar results (Figure 9, *right*). However, there was a great deal of intersubject variability that was evident among subjects ($Corr(sD^{*},sI^{*})_s$ = 0.11 ± 0.64); some correlations were strongly negative, others strongly positive, and others did not correlate at all. These correlations were found to be a function of the inhalation breathing frequency, with the

lower f_N subjects having a negative relationship between sD^*_{sl} and sI^*_{sl} ($Corr(Corr(sD^*,sI^*)_s,f_N)$ = 0.89, P($Corr$>0) = 0.0012).

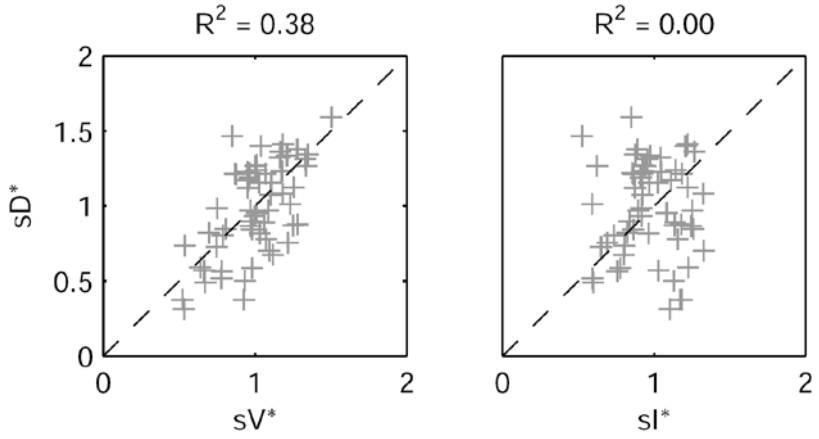

Figure 9: *sD** vs. *sV** **(***Left*) and *sD** vs. *sI** (*Right*) for all lobes of all subjects. The square of the Pearson correlation Coefficient is shown above each plot.

Relationship Between sI* and sV*

We found no correlation between sI^*_{sl} and $s\dot{V}^*_{sl}$ among all subjects. However, the 3 subjects who had the highest percent predicted FEV_1 during imaging had positive correlations ranging from 0.71 to 0.95. It is of interest to note that there was a strong negative relationship between the lobar $F_{VOL,sl}$, measured from the single CT at MLV, and the value of sI^*_{sl} derived from 2 images (average $Corr(F_{VOL},sI^*)_s$ = -0.94 ± 0.08). This suggests that in bronchoconstricted subjects sI^*_{sl} may represent the degree of mean lobar expansion during breathing rather than an index of specific ventilation.

Sources of Variability in sD*

There was high variability in sD^*_{sl} among lobes: average COV_{Lobes} of 0.335 ± 0.082 among lobes in a subject, and an average $COV_{Subjects}$ 0.264 ± 0.109 among the same lobe in different subjects. Deposition in the LLL was significantly lower than other lobes except for the RML (Figure 10, *left panel*). This variability was reduced after accounting for regional differences in lobar

ventilation: average COV_{Lobes} = 0.277 ± 0.067, average $COV_{Subjects}$ = 0.214 ± 0.105 (Figure 10 *center panel*). After accounting for branching factors and a portion of the particle retention effects, the variability was further reduced: average COV_{Lobes} = 0.116 ± 0.074, average $COV_{Subjects}$ = 0.084 ± 0.057 (Figure 10, *right panel*).

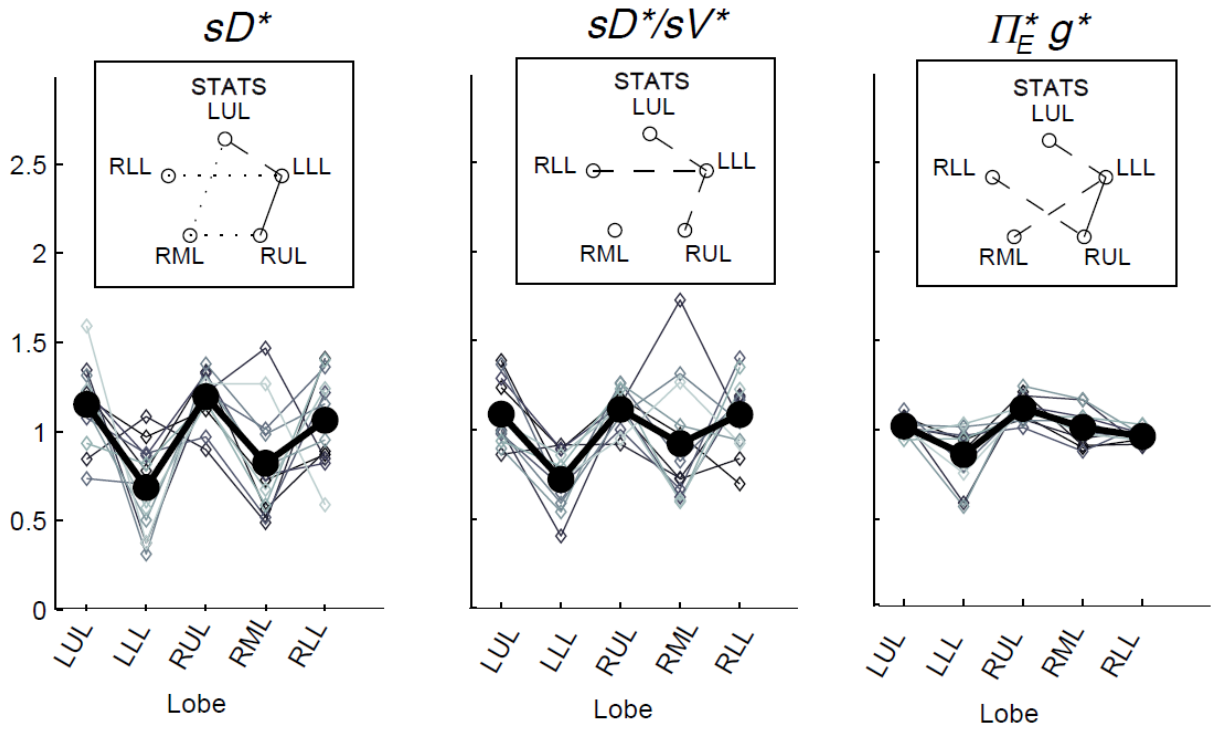

Figure 10: Variation among lobes as sources of variance are accounted for. Lobar values for each subject are connected with thin lines, and the thick solid line connects average values. *Left*: relative specific deposition *sD**, *Center*: relative deposition per unit of relative ventilation (*sD*/sV**), *Right*: the apparent escape fraction. Statistically significant differences between any two lobes are depicted as a line connecting the lobes to the above each plot (solid is P<0.001, dashed is P<0.01, and dotted is P <0.05). The absence of a line indicates that no statistically significant differences were evident.

The contribution of each of the three factors to the variability in specific deposition was characterized using the Pearson Correlation Coefficient squared among the specific deposition and measurements of its influencing factors. The contribution of these three factors to the average variability in sD_{sl}^{*} was approximately 1/3 for each factor (**Error! Reference source not found.**). However, the variances of lobar $s\dot{V}_{sl}^{*}$ and $\Pi_{B,sl}^{*}h_{sl}^{*}$ among all lobes and subjects was about ½ of the

variance of sD_{sl}^{*} while the variance of $\Pi_{E,j}^{*} g_{j}^{*}$ was only 1/7 of that of sD_{sl}^{*} (**Error! Reference source not found.**). Weak interactions were observed among the specific ventilation, the apparent net branching factors, and the apparent net escape fraction (**Error! Reference source not found.**). This suggests that the separation of the sources of variability in Equation (24), which neglected covariance between the parameters, is in fact accurate for the present data.

Table 1: Relationships among measured values

X_j	Y_j	$\underset{j \in S}{\mathrm{Corr}}\left(X_j, Y_j\right)^2$
sD_{sl}^{*}	sV_{sl}^{*}	0.38
sD_{sl}^{*}	$\Pi_{B,sl}^{*} h_{sl}^{*}$	0.38
sD_{sl}^{*}	$\Pi_{E,j}^{*} g_{j}^{*}$	0.31
sV_{sl}^{*}	$\Pi_{B,sl}^{*} h_{sl}^{*}$	0.01
sV_{sl}^{*}	$\Pi_{E,j}^{*} g_{j}^{*}$	0.02
$\Pi_{B,sl}^{*} h_{sl}^{*}$	$\Pi_{E,j}^{*} g_{j}^{*}$	0.04

Table 2: Relative variability of factors influencing specific deposition

x_j	sV_{sl}^{*}	$\Pi_{B,sl}^{*} h_{sl}^{*}$	$\Pi_{E,sl}^{*} g_{sl}^{*}$
$\underset{j \in S}{\mathrm{var}}\left(x_j\right) / \underset{j \in S}{\mathrm{var}}\left(sD_j^{*}\right)$	0.48	0.45	0.15

A Relationship Among f_N, F_{VOL}, and sD*/sV*

The variability among subjects in *sD*/sV** for each lobe was well organized by the frequency of breathing during nebulization in the LLL, RLL and RML. In Figure 10 the plots for each lobe have been ordered from left to right based on the average expansion at MLV. Note the least expanded lobes during inhalation (the LLL and RLL) tended to increase their deposition per unit ventilation with increasing breathing frequency, while the opposite was true for the most expanded lobe which was the RML.

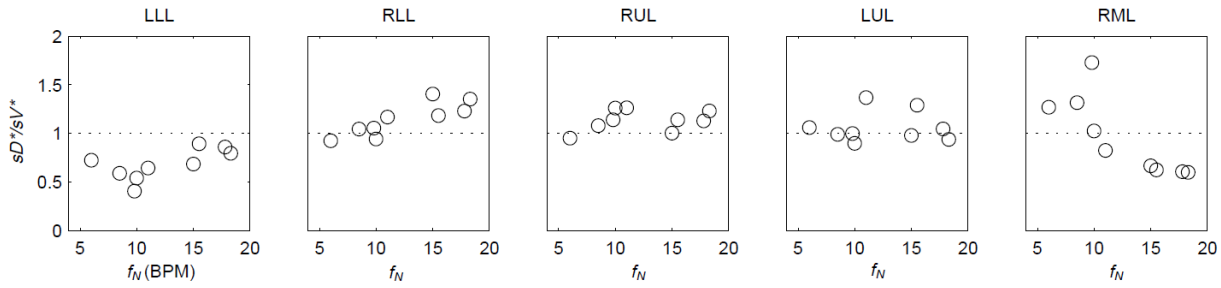

Figure 11: The ratio of *sD*/sV** for each lobe vs. the breathing frequency during nebulization for the 9 subjects whom the frequency data was available. The lobes have been reordered based on their average inflation at MLV.

This effect is also shown as a systematic, gradual frequency dependence of the correlation between lobar $F_{VOL,sl}$ and *sD*/sV** for the different subjects (Figure 12). Note that the subjects breathing the slowest showed strong positive correlations, while those breathing the fastest showed a strong negative relationship ($Corr(Corr(sD^*/sV^*, F_{VOL}), f_N) = -0.97$, $P(Corr. > 0) < 0.0001$).

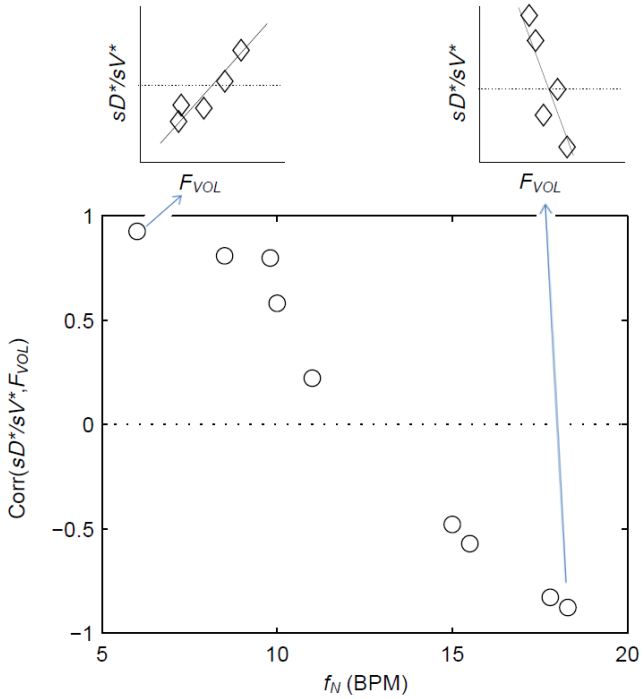

Figure 12: The relationship correlation between inflation F_{VOL} and sD^*/sV^* was strongly modulated by the inhalation breathing frequency.

Discussion

Key Findings

We have presented a theoretical framework to quantify four mechanisms that can lead to heterogeneous aerosol deposition among lobes: differences in lobar ventilation, uneven splitting of aerosol and air at bifurcations, differences in the fraction of aerosol deposited along the feeding airways, and differences in the fraction of aerosol that reaches the periphery but escapes via exhalation. We used this framework to quantify the contribution of these four effects in a group of 12 bronchoconstricted subjects with asthma. The following observations were seen from our data: First, differences in lobar specific ventilation (measured from the turnover rate of ^{13}NN washout) and in the apparent net branching factors each accounted for more than a third of the variability in deposition among lobes and subjects. The remaining variability was caused by differences in deposition along the feeding airways as characterized by their apparent net escape fractions. Secondly, subjects breathing slowly (< 9BPM) during nebulization had a strong relationship

between regional deposition and ventilation with PET, while the relationship weakened in subjects breathing more rapidly. Also in subjects breathing more rapidly, more expanded lobes showed *lower* deposition per unit ventilation than less expanded lobes, while the opposite was true for subjects breathing slowly. Lastly, differences in lobe expansion between HRCTs at two lung volumes did not systematically explain any variability in deposition across all subjects.

The Relationship Between sD* and sV* Depended on f_N

Large inter-subject variability was observed in the relationship between $s\dot{V}_{sl}^{*}$ and sD_{sl}^{*}. These include a tendency for strong positive relationships between the two measures when the subjects breathed at a lower breathing frequency and weaker positive relationships in those subjects that breathed at a faster frequency. It is likely that the other factors besides ventilation become important at higher breathing frequencies (possibly due to increased central impaction, increased branching factor effects, and a more variable retention fraction). This pattern is qualitatively consistent with a recent CFD model undertaken by Darquenne et al.[56] that used an idealized geometry of the human airway and uniform specific ventilation to evaluate the relationship between the ventilation and aerosol delivery to lung segments. Their results showed that the delivery of aerosol to lung segments was largely determined by the distribution on ventilation for Stokes numbers in the trachea less than 0.01. Conversely, they showed that when 10 μm particles were inhaled at flow rates 500ml/s, other effects besides the distribution of ventilation had a strong impact on the transport of aerosol to the periphery. They also found that the Stokes number of the segmental airway feeding the sublobe explained 55% of the variance in deposition that was not otherwise explained by ventilation. Similar quantification in the present experimental work remained elusive; among other challenges, the polydisperse nature of the aerosol used in this study, together with uncertain proximal filtering effects, make it difficult to evaluate comparable Stokes numbers from the present data. In addition, where the CFD model compares all particles that escaped the segmental airways to the ventilation passing through that airway, the in-vivo data measured here must consider that not all of these particles deposit, and that some are lost via exhalation. Despite these difference, the range in sD^*/sV^* (average COV_{Lobes} = 0.277 ± 0.067) was similar to the range in R (a measure equivalent to $sD^*/(sV^*\eta^*)$) observed in the CFD model at a Stokes numbers in the trachea of 0.02 to 0.04. To use the present data to validate CFD models of aerosol deposition, a polydisperse aerosol should be used in the model, and the effect of incomplete deposition in the lobar periphery must be considered.

Lung disease may influence the relationship between regional ventilation and deposition[18]. In diseased lungs the presence of constricted or obstructed airways can be expected to interfere with the relationship between ventilation and deposition. This may happen when an obstruction in an airway (such as in cystic fibrosis[16], or asthma[57]) both collects deposition and interferes with the ventilation of subtended regions of the lung. Indeed, no relationship between ventilation and deposition was found in 10 subjects with HIV infections using a 2D gamma-scintigraphy[15]. Other factors in poorly ventilated regions may lead to paradoxical increases in deposition; within these regions suspended particles may have more time to sediment than in well ventilated regions due to lower gas turnover rates[17]. It is also possible that the reduced caliber of constricted airways may lead to shorter sedimentation distances and allow for more complete retention. However, these paradoxical effects have only been observed after correcting for the bulk effect of reduced ventilation[17], and are likely of second order.

sV* Accounts for a Third of the Variability in sD*, sI* Does Not

When we compared $s\dot{V}_{sl}^{*}$ to sD_{sl}^{*}, the dynamic ventilation measurement derived from PET accounted for more than a third of the variability in deposition among the lobes of all subjects. In contrast, the specific inflation sI_{sl}^{*} derived from two static CT images failed to similarly explain the variability in sD_{sl}^{*}. Presumably, the dynamic PET measure captures the reduced ventilation of slowly filling regions (that would have time to fill during the breath hold needed for CT, which ranges between 4 to 16 seconds depending on the slice). However, if this was the only explanation for our findings, one would have expected that the correlation between sD_{sl}^{*} and sI_{sl}^{*} would have been most positive in those subjects breathing with the lowest f_N. Remarkably, the opposite was true: sD_{sl}^{*} and sI_{sl}^{*} had the highest positive correlations in subjects breathing with high f_N, while in subjects breathing with low f_N the correlation was strongly negative! It is therefore likely that both the positive and negative correlations between sD_{sl}^{*} an sI_{sl}^{*} are in fact due to the strong negative relationship between sI_{sl}^{*} and $F_{VOL,sl}$, a parameter that may be related to lobar retention, as we discuss below.

A recent study of mild to moderate asthmatic, but not bronchoconstricted, subjects compared estimates of ventilation using static HRCT at two lung volumes to the deposition pattern of 1.3 μm ^{99m}Tc particles inhaled during slow tidal breathing as imaged by SPECT-CT[61]. They found

that the average difference in ventilation distribution of a lobe between the static estimates and the ^{99m}Tc deposition were only 3%. This measure would be approximately 12% of the lobar ventilation (only four effective lobes were used in that analysis). In contrast, our measurements using injected ^{13}NN with PET-CT with *bronchoconstricted* asthmatic subjects during spontaneous tidal breathing showed average differences of 22% between sI^*_{sl} and $s\dot{V}^*_{sl}$, with no overall correlation between these variables. Our finding is consistent with earlier measurements from our laboratory[60], which concluded that in asthmatic subjects, or in bronchoconstricted normal subjects, static measures from HRCT did not correlate with the sub-lobar distribution of specific ventilation. The two measures correlated only among normal subjects before bronchoconstriction.

If CFD models of aerosol inhalation during tidal breathing are to reflect clinical reality in *diseased* or *bronchoconstricted* lungs, boundary conditions determined from measurement that are sensitive to the dynamic effects of slowly filling and emptying regions may be required. However, it is still possible that lobar inflation patterns measured from two static CT scans could yield representative boundary conditions for airflow in CFD models of healthy lungs, or in diseased lungs with slow and deep breaths.

Explaining the Relationship Among f_N, $F_{VOL,}$ and sD*/sV*

Among subjects breathing at very low (< 9 BPM) and very high frequencies (>17 BPM) the expansion of the lobes was strongly related to the deposition not explained by ventilation, albeit the direction of the effect depended on breathing frequency. While this signal was exceptionally strong, it is not easily interpreted. One possible explanation is as follows: lobes with high $F_{VOL,sl}$ are expected to have dilated airways with reduced retention η_{sl} due to both the longer sedimentation distances and reduced likelihood of impaction due to slower velocities and wider turns. Additionally, the analysis based on data from Kim et al.[55] (Figure 5) showed a 20 -60% reduced $\overline{\eta_s}$ in subjects breathing with a higher f_N. A reduction in $\overline{\eta_s}$ could be expected to amplify differences in η^*_{sl} caused by heterogeneous $F_{VOL,sl}$, thus generating a negative correlation with the measured deposition and $F_{VOL,sl}$. An alternative explanation is based on the branching effect at the junction between the RML and RLL (bifurcation 4 in Figure 6). From the data in Figure 11, it is clear that *sD*/sV** in the RML (the lobe with the highest average $F_{VOL,sl}$ across subjects) is inversely related

with the subject's f_N, while the opposite is true for the lobe with the lowest average $F_{VOL,sl}$ across subjects (the RLL). It could be that at higher f_N, the sharp turn to the RML causes the aerosol to keep moving into the RLL. However, this theory does not explain the positive effect of f_N for the LLL.

It is important to note that although these explanations are consistent with the emerging phenomenon at high f_N, alone they can't explain why hose same high $F_{VOL,sl}$ lobes appear to be receiving greater deposition than would be expected based on their ventilation at low f_N. To explain this, a certain degree of bias for a positive relationship between $F_{VOL,sl}$ and *sD*/sV**, driven by a consistently low *sD*/sV** in the LLL (a lobe that also has low $F_{VOL,sl}$). This low *sD*/sV** appears to be evident in the $\hat{\Pi}^*_{E,sl}$ of the LLL in Figure 10, and could be related to the definition of the LLL CA used in our analysis: the Vida output separates the segments LB1 and LB2 as distinct sublobes. In most subjects a single apicoposterior segment of the LUL is fed by the more proximal airway LB1+2[62] (as is illustrated in Netter, Altlas of the human anatomy, Plate 203[63]). If this latter perspective is correct, it may be that the current LLL CA definition consistently one generation deeper than other lobes, and thus captures more of the deposition, which would result in a lower $\hat{\Pi}^*_{E,sl}$. This may illustrate the importance of consistent anatomical definitions among lobes[7].

Methodological Limitations

A number of methodological limitations in the present study should be considered when interpreting our findings. First, the lobar retention fractions could not be measured, but are required to obtain accurate estimates of the actual net escape fractions and branching factors. Unless particle motion can be visualized, these values may need to be estimated from CFD or analytical models in which the data provided by our study could be used as input. Despite this limitation, we were able to separate apparent net branching factor and escape fractions, and to directly express in Eq. (30) how heterogeneity in retention fractions among lobes causes these measures to differ from the actual branching factor and retention fractions. Additionally, using aerosol bolus data from Kim et al.[55] we identified a relationship that estimates the overall magnitude of the peripheral retention that we could expect in the present data, and provided a means to understand how breathing frequency during inhalation affects the retention.

It was also assumed that the fine particles that escape deposition in the periphery do not significantly deposit in the central airways on their egress from their lung. While this is likely the case when only a small fraction of the aerosol is exhaled, when a significant amount of aerosol is exhaled, deposition during exhalation should be considered, particularly in the presence of flow limitation in the central airways[64]. The primary consequence of not considering this effect is an underestimation of airway escape fractions.

Additional limitations in the measurements arise from the estimation of ventilation distribution. The distribution of ventilation during nebulization was assumed to be similar to the distribution of alveolar minute ventilation measured 10 minutes later (30 ± 4.5 minutes after Mch), an assumption that could be weakened by the presence of a nebulizer circuit during the nebulizing image, and the possibility of a reduced methacholine effect during the ventilation image; while some researchers have found little change in the degree of methacholine induced bronchoconstriction after 60 minutes[65], others have found that methacholine wears off by 60% within 30 minutes[66].

The close proximity (15.4 +/- 2.2 mins) between the deposition and ventilation images, meant that there was some residual labeled aerosol that was registered as ^{13}NN gas in the washout image. This residual activity was very small compared to the activity coming from the ^{13}NN (<4%) and similar among lobes, and thus weakly affects sV_{sl}^{*}.

There are also potential errors in the estimates of sD_{sl}^{*} that were fully explored in a previous paper[7]. The overall effect of such potential errors in sD_{sl}^{*} and sV_{sl}^{*} are challenging to quantify, and they are in part responsible for some of the variability in $sD_{sl}^{*} / sV_{sl}^{*}$ (shown in Figure 10, *central panel*). However, given the high correlation between sD_{sl}^{*} and sV_{sl}^{*} that was observed in subjects breathing with slow frequency, and the systematic effects of f_N on the relationship between $F_{VOL,sl}$ and $sD_{sl}^{*} / sV_{sl}^{*}$, it is unlikely that these limitations invalidate our results. Also, as $\hat{\Pi}_{E,sl}^{*}$ can be derived from the aerosol deposition pattern alone, it is insulated from errors in the ventilation estimation. This isolation is evident in the consistent measurements across subjects of $\hat{\Pi}_{E,sl}^{*}$. $\hat{\Pi}_{B,sl}^{*}$, on the other hand, is sensitive to errors in both the ventilation and

deposition assessment, and errors in the interpretation of both images likely contributed to some of the variance in $\hat{\Pi}^{*}_{B,sl}$.

Clinical Relevance

In this study, we evaluated the heterogeneity in aerosol deposition and ventilation in conditions similar to those expected clinically by allowing the subjects to breathe freely without attempting to control their lung volumes or breathing frequency. This technique provided us with a data set of that spanned the physiological range of breathing frequencies during nebulization. From our results it has become clear that breathing frequency and lung expansion appear to have important effects on the relationship between ventilation and aerosol deposition among subjects at a lobar level. Although these effects were not expected *a-priori*, they provide an important basis for future experimental and numerical studies where these effects can be controlled and evaluated. The present data set can be used to identify physiologically appropriate boundary conditions for ever improving CFD models.

Despite other sources of heterogeneity, it is clear that poorly ventilated regions of the lung will generally receive a smaller fraction of the inhaled aerosol than better ventilated regions. Lower deposition might result in paradoxical effects where an inhaled bronchodilator could aggravate the discrepancy between low and high ventilated regions. This effect has been anecdotally observed with imaging in our laboratory[31], where a single administration of bronchodilator increased the size of ventilation defects in an asthmatic subject. In the present study several regions that received low ventilation clearly showed markedly reduced aerosol deposition as exemplified in the extreme case presented in Figure 13.

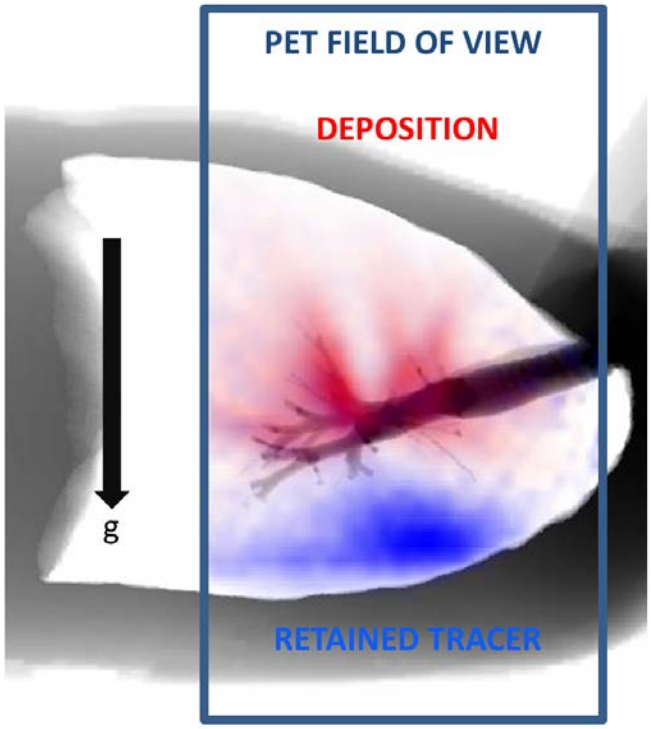

Figure 13: This ventilation defect, shown by the trapped gas at the end of washout (blue) in the dependent regions of the image, receives little deposition (red). The strong ventilation defects in the subject's left and right lower lobes may have caused the deposition to avoid the lower lobes.

The theoretical framework presented here has proven to be a useful tool to describe and understand parallel heterogeneity in deposition among lobes. In the bronchoconstricted asthmatic subjects studied, more than a third of this variability was caused by ventilation heterogeneity; poorly ventilated lobes tended to receive lower aerosol deposition. Breathing was not controlled during nebulization in this study, and it is expected that the deposition pattern observed after nebulization during spontaneous breathing is reflective of the type of distribution that occurs beyond laboratory walls. The relationship between ventilation and deposition has implications for the distribution of aerosol therapies in subjects with heterogeneous ventilation, and should be considered when using inhaled therapies to treat regions of poor ventilation.

In summary, heterogeneity in specific deposition among lobes can emerge from 1) differences in lobar ventilation, 2) uneven splitting of aerosol and air at bifurcations, 3) differences in the fraction of aerosol trapped by feeding airways, and 4) differences in the fraction of aerosol that is retained in the periphery and not exhaled. These effects were integrated into a theoretical framework that provided insight into measurements of deposition and ventilation in bronchoconstricted asthmatic subjects. In this data, heterogeneous specific ventilation accounted in

average for more than a third of the heterogeneous specific deposition of aerosols among lobes. This relationship can cause inhaled aerosol therapy to miss poorly ventilated regions. Lobar inflation between two CT images did not show a similar relationship, suggesting that dynamic PET may provide a better estimate of ventilation for bronchoconstricted asthmatic subjects. The remaining three factors besides ventilation that influence specific deposition appeared to be related to the inflation of the lobes during nebulization in a way that was strongly modulated by the breathing frequency during nebulization, though the mechanism for this remains somewhat unclear. Understanding the ventilation-deposition relationship at a regional level may help to develop strategies for inhaled therapies.

Acknowledgements

Research reported in this chapter was supported by the National Institutes of Health under award number R01HL68011. The content is solely the responsibility of the authors and does not necessarily represent the official views of the National Institutes of Health. Additional support was provided by American Air Liquide Inc., and Aerogen is thanked for providing the vibrating mesh nebulizers

Author Disclosure Statement

This work was sponsored in part by American Air Liquide Inc. and Aerogen. However, there is no conflict of interest with these parties on any of the material presented in this chapter.

Appendices

Appendix I

Lobar retention fractions were not available from our data. Inhalation bolus data from Kim et al. [55] 1996 were used to calculate the overall retention fraction at penetration volumes V_P greater than 100ml (about the depth of the sub segmental airways) for particle sizes d_p ranging from 1-5 um, delivered at a fixed tidal volume V_T of 500ml constant inhalation speeds Q_N ranging from 150 to 500 ml/s. To estimate the retention fraction, we calculated the fraction of the inhaled aerosol that deposited past 100ml by removing the deposition in regions more proximal than 100ml (provided in Figure 8) from the non-bolus total deposition (Table 3). We compared the deposition to the fraction of aerosol that survived the first 100 ml, which was determined by fraction exhaled in the 100 ml bolus depth experiment. The ratio of the deposited fraction to the fraction that arrived is the retention fraction.

We then calculated the distance d_s that the monodisperse aerosols in each of the experiments would travel during the average residence time t_s at depths greater than 100 ml if the particles traveled at the Stokes settling velocity v_s.

$$d_s = v_s t_s = \left(\frac{g \rho d_p^{\,2}}{18 \mu} \right) \left(\frac{V_T \left(1 - \frac{V_P}{V_T} \right)}{Q_N} \right) \qquad \textbf{(32)}$$

Where gravity, the density of the particle and the viscosity of air are represented with their conventional symbols. We found that 97% of the variance among the experiments could be explained with a single parameter fit:

$$\eta_{fit} = 1 - e^{-\frac{d_s}{371 \mu m}} \qquad \textbf{(33)}$$

Note that the fit constant of 371um is on the order of an alveolus.

Estimating the global retention fraction in the present data set taken with polydisperse aerosols is significantly more complex. Given a particle distribution function P, the net retention fraction can be estimated as:

$$\overline{\eta_{fit}} = \int_0^\infty P(\tau)\eta_{fit}(\tau)d\tau \qquad \textbf{(34)}$$

The particles size distribution was measured to be lognormal with a VMD of 4.9um and a GSD of 1.8. Larger particles are more likely to deposit in the upper airways, and the distribution reaching the periphery is expected to have a reduction in larger particles. We therefore numerically integrated the above equation for the net retention fraction for particles below several cutoff diameters (see Figure 5).

Appendix II

Apparent and actual net branching factors and escape fractions. It is helpful to first define an *apparent* concentration $\hat{c}_x = D_x / V_x = c_x \eta_x$ as the concentration of aerosol that at a location x in the airway that will ultimately deposit and which we can directly measure. If we use the apparent concentration in place of the actual concentration, we can derive an *apparent* net branching factor $\hat{\Pi}_{\mathrm{B},sl}$ and *apparent* net escape fraction $\hat{\Pi}_{E,sl}$ using equations (10)-(14). These can be non-dimensionalized by the by the average apparent branching factor and average apparent escape fraction to arrive at $\hat{\Pi}^*_{\mathrm{B},sl}$ and apparent net escape fraction $\hat{\Pi}^*_{E,sl}$. In the absence of information about lobar retention fractions it is necessary to understand how the apparent parameters (the factors that are calculated if the retention fraction is assumed to be one) relate to the actual parameters. If we consider the ratio of the escape fractions in terms of the distribution of aerosols, and then factor out the retention fractions, we arrive at our first result:

$$\frac{\hat{\Pi}^*_{E.sl}}{\Pi^*_{E.sl}} = \frac{\left(\frac{D_{P,sl}}{D_{T,sl}}\right)\left(\frac{D_{T,s}}{D_{P,s}}\right)}{\left(\frac{D_{P,sl}+D_{E,sl}}{D_{0,sl}}\right)\left(\frac{D_{0,s}}{D_{P,s}+D_{E,s}}\right)} = \frac{\eta_{sl}/\eta_{carina,sl}}{\overline{\eta_s}/\eta_{carina,s}} = g^*_{sl} \qquad \textbf{(35)}$$

Further, sD^*_{sl} can be written in terms of the non-dimensional actual and apparent factors. If we equate the two we conclude that:

$$\hat{\Pi}^{*}_{B.sl}\hat{\Pi}^{*}_{B.sl} = \Pi^{*}_{B.sl}\Pi^{*}_{B.sl}\eta^{*}_{sl} \quad \textbf{(36)}$$

By substituting our first result into this equation we conclude that:

$$\frac{\hat{\Pi}^{*}_{B,sl}}{\Pi^{*}_{B,sl}} = \frac{\eta^{*}_{sl}}{g^{*}_{sl}} = \frac{\eta_{carina,sl}}{\eta_{carina,s}} = h^{*}_{sl} \quad \textbf{(37)}$$

Chapter III: Regional Ventilation and Aerosol Deposition with Helium-Oxygen in Bronchoconstricted Asthmatic Lungs

Elliot Eliyahu Greenblatt MS [1,2], Tilo Winkler PhD[2], Robert Scott Harris MD[2], Vanessa Jane Kelly PhD [2], Mamary Kone MD[2], Ira Katz PhD [3,4], Andrew Martin PhD [5,6], George Caillibotte PhD [3], Dean R. Hess[2], Jose Venegas PhD [2]

[1]Massachusetts Institute of Technology, Boston, MA, USA
[2]Massachusetts General Hospital and Harvard Medical School, Boston, MA, USA
[3]R&D Medical, Air Liquide Santé International, Les-Loges-en-Josas, France
[4]Department of Mechanical Engineering, Lafayette College, Easton, PA, USA
[5]Delaware Research and Technology Center, American Air Liquide, Newark, DE, USA
[6]Mechanical Engineering, University of Alberta, Edmonton, AB, Canada

This chapter has been submitted to the Journal of Aerosol Medicine and Pulmonary Drug Delivery, and the text and figures are reproduced here with the permission of the publisher.

Abstract

Background: He-O_2 has lower density than room air and may increase peripheral aerosol deposition and result in more homogenous deposition in the periphery. However, that effect of He-O_2 has not been consistently observed. This chapter considers whether the ventilation and deposition patterns obtained in a group of 10 bronchoconstricted asthmatic subjects breathing He-O_2 differed from the ventilation and deposition patterns of a previously studied similar group of 12 subjects breathing air.

Methods: PET-CT imaging was used to generate 3D anatomical maps and lobar values of relative specific deposition *sD**, relative specific ventilation *sV**, and lung expansion F_{VOL}. The imaging data were analyzed along with the breathing frequency during inhalation f_N to estimate factors affecting the lobar distribution of *sD**.

Results: The distributions of *sD** and *sV** were not statistically different between the air and He-O_2 groups. Among subjects with uneven *sD**, the correlation with *sV** was on average higher ($p<0.05$) in the He-O_2 group (0.84+/-0.8) compared with the air-group (0.55+/-0.28). There was also a tendency for larger number of lobes having *sV** and *sD** closer to unity with a few lobes having more extreme differences in the He-O_2 group. Higher f_N , previously found to weaken the correlation in the air group, had no effect in the He-O_2 group and the f_N dependent effect of F_{VOL} on *sD**/*sV** found in the air group was not detected in the He-O_2 group.

Conclusion: Within these limited number of bronchoconstricted mild asthmatic subjects we could not detect systematic differences in the distributions of *sD** or *sV** between the group breathing He-O_2 and that breathing air. Future studies using these personalized data sets as inputs of realistic CFD models may help yield a clearer understanding of when and for whom breathing He-O_2 during aerosol inhalation may be beneficial.

Keywords: helium-oxygen, lobar, ventilation, aerosol deposition, carrier gas, escape fraction, retention fraction, aerosol concentration, peripheral deposition, lung expansion, breathing frequency.

Introduction

Breathing a helium oxygen gas mixture (He-O_2) is used to reduce the effect of severe lung obstruction in asthma, COPD, and bronchiolitis and has been proposed as a possible means of enhancing aerosol delivery[12, 57, 58, 67, 68]. Because He-O_2 is less dense than air, turbulent flows are is less likely to develop in the glottis and central airways[12, 57, 58, 67, 68], thus reducing central aerosol deposition and increasing the peripheral aerosol delivery[58, 67-69]. Additionally, the lower density of He-O_2 may also reduce pressure losses in central airways where gas inertia is an important component of airway resistance[57]. In the presence of heterogeneous central airway obstruction, a reduction in airway resistance by He-O_2 could homogenize the intrapulmonary distribution of alveolar ventilation[70] and given that aerosol therapy is carried in gas suspension it could result in more even deposition among peripheral regions[56, 71].

Indeed, computational fluid dynamic (CFD) models have shown lower aerosol deposition in the extrathoracic airways with He-O_2 [72], reduced turbulent mixing [14], increased peripheral deposition and more homogenous ventilation[57]. However, experimental and clinical evidence testing the premise that He-O_2 results in increased peripheral deposition[57, 58, 67-69, 73-75] have not been conclusive and few studies have addressed whether using He-O_2 as carrier gas homogenizes ventilation or aerosol deposition among parallel regions of the lung. It is therefore not surprising that the clinical benefit of using He-O_2 to enhance aerosol therapy in bronchoconstricted asthmatic subjects remains unclear[76].

Given the complexity and multifactorial nature of aerosol deposition[71], it is likely that using validated, physiologically informed computational models may be the best candidate to test how and for whom aerosol delivery with He-O_2 will benefit. The primary aim of this research was to collect 3D imaging data sets of anatomical structure, ventilation, and aerosol deposition data in bronchoconstricted asthmatic subjects receiving aerosol with He-O_2 as a carrier gas under typical clinical conditions using PET-CT. Together with our earlier work with air as the carrier gas, these data sets can be used as a realistic platform to both validate and provide physiological boundary conditions for CFD models on a personalized basis. A second aim of the research of this chapter, was to compare the distributions of ventilation and aerosol deposition obtained with He-O_2 with those obtained with air[71]. Using the theoretical framework described in a previous paper[71], we estimate the contribution of a number of factors on aerosol deposition in peripheral regions of the lung. We investigated whether significant differences in deposition pattern or in the factors affecting its heterogeneity could be detected between the subjects breathing air vs. those breathing He-O_2. By supporting future numerical studies, and by evaluating PET-CT images of deposition with

He-O_2 with new analysis techniques, the present work seeks to contribute to our understanding of how carrier gasses affect the regional distribution of aerosol.

Nomenclature

peripheral	Airways and lung tissue peripheral to the subsegmental airways
central	The central airways up to and including the subsegmental airways
x_s , x_{sl}	The subscript *s* indicates the subject's value *x*, and the subscript *sl* indicates the value x of an individual lobe *l* of subject *s.*
sD^*_{sl} , sD^*_{sv}	The specific peripheral deposition of a lobe normalized by the average specific deposition of the whole lung, and this value for a voxel *v*
$s\dot{V}^*_{sl}$	The specific ventilation of a lobe normalized by the specific ventilation of the whole lung.
η^*_{sl}	The retention fraction of a lobar periphery normalized by the retention fraction of the entire periphery
$\Pi^*_{B.sl}$, $\hat{\Pi}^*_{B,sl}$	The net branching factor of a given lobe, and this value estimated with the assumption of complete retention
$\Pi^*_{E.sl}$, $\hat{\Pi}^*_{E,sl}$	The net escape fraction of a given lobe's pathway normalized by the escape fraction of the all central airways from the carina onward, and this value estimated with the assumption of complete retention
S	The set of all lobes of all subjects
ζ_s	The set of all voxels of subject *s* that are within the parenchyma and removed from the lung surface by at least 1cm.
MLV,TLC	The mean lung volume during tidal breathing, and total lung capacity
d_s , v_s , t_s	The distance a particle would sediment, the settling velocity, and the settling time
$F_{VOL,sl}$	The degree of expansion of a lobe (the gas volume/the non-gas volume)
f_N	The breathing frequency of a given subject during inhalation
FEV_1	Forced Expiratory Volume in 1 second after a deep inhalation
FVC	Forced Vital Capacity
FER	Forced Expiratory Ratio

BMI	Body Mass Index
MCh	Methacholine
PC_{20}	Concentration of MCh that causes a 20% drop in FEV_1 in a subject
VMD	Volume Median Diameter or the diameter of the aerosol droplet for which half of the aerosol volume is larger and half is smaller
GSD	The Geometric Standard Deviation of the lognormal volume histogram of aerosol droplet diameters

Methods

Theoretical Framework

We recently introduced[71] a theoretical framework that quantified four factors affecting aerosol deposition in the lung periphery: differences in ventilation , unequal partitioning between aerosol and air at bifurcations, differences in the fraction of aerosol escaping deposition in central airways, and differences in the fraction of aerosol reaching the periphery that is exhaled. We identified metrics for each of these four factors for each subject *s* and lobe *l*, and evaluated their values after normalizing by the respective lung averages for each subject. The framework describes the relative specific deposition sD_{sl}^* as the product of the relative specific ventilation $s\dot{V}_{sl}^*$ (capturing lobar ventilation differences), the net branching factor $\Pi_{B.sl}^*$ (capturing the net effect of unequal partitioning between aerosol and air at bifurcations on the aerosol reaching each lobe), the net escape fraction $\Pi_{E.sl}^*$ (capturing relative differences in the fraction of aerosol escaping deposition in central airways feeding each lobe), and the lobar retention factor η_{sl}^* (capturing relative differences in the fraction of aerosol reaching the periphery that is retained and not exhaled for each lobe):

$$sD_{sl}^* = s\dot{V}_{sl}^* \Pi_{B.sl}^* \Pi_{E,sl}^* \eta_{sl}^* \quad (38)$$

We further demonstrated that in the absence of direct measurements of the lobar retention fractions, the specific deposition could be described in terms of the *apparent* net branching factor $\hat{\Pi}_{B.sl}^*$ and the *apparent* net escape fraction $\hat{\Pi}_{E.sl}^*$ estimated from experimental imaging data of $s\dot{V}_{sl}^*$

and sD_{sl}^{*} under the assumption of complete retention of aerosol entering into the lung periphery. Each of these *apparent* factors expresses a portion of the lobar retention factor η_{sl}^{*}, such that:

$$sD_{sl}^{*} = s\dot{V}_{sl}^{*}\hat{\Pi}_{B.sl}^{*}\hat{\Pi}_{E,sl}^{*} \quad (39)$$

Experimental Methods

Overview

The imaging protocol, methods of image analysis, and the extraction of regional parameters, were identical to those described in our earlier study of bronchoconstricted asthmatic subjects breathing room air[71]. Portions of that study are used here for comparison. The only methodological difference between protocols was the carrier gas; instead of air, the subjects were breathing a gas mixture of 79% helium and 21% oxygen (Airgas, custom blend) during aerosol delivery and the ventilation image. The subjects included in both studies were well matched in terms of demographics and pulmonary function (

Table 3). They were young, predominantly female and not obese (BMI's less than 32 kg/m^2) and had mild intermittent or mild persistent asthma as defined by the NIH Global Initiative for Asthma[35] (FEV_1 and FVC ≥ 80% predicted, less than daily symptoms, and peak flow or FEV_1 variability of less than 30%). All subjects demonstrated reversible obstruction with inhaled albuterol (≥ 12% on previous clinical spirometry). Note that all while we collected aerosol deposition data in 14 subjects breathing air, in only 12 of these subjects were we able to obtain ventilation data, and these are used here for comparison with the subjects breathing He-O_2.

Table 3: Subject data on the screening day for the air and He-O_2 Groups (± SD)

Parameter	Air	He-O_2
n	12	10
Male/Female	3/9	2/8
Age (years)	20.1 ± 1.8	19.2 ± 1.2
Weight (kg)	65 ± 10	67 ± 11
Height (cm)	167 ± 10	169 ± 10
FEV_1 (L)	3.76 ± 0.9	3.94 ± 0.64
BMI (kg/m^2)	24 ± 3	24 ± 4
FEV_1 (% Predicted)	102.7 ± 8.9	92.4 ± 31.4
FVC (L)	4.58 ± 0.92	4.68 ± 0.98
FER (1/s)	0.84 ± 0.07	0.85 ± 0.05
FVC (% Predicted)	107.1 ± 6.4	108.5 ± 12.5
PC_{20} (mg/ml)	0.99 ± 1.88	0.70 ± 0.66

Imaging Protocol

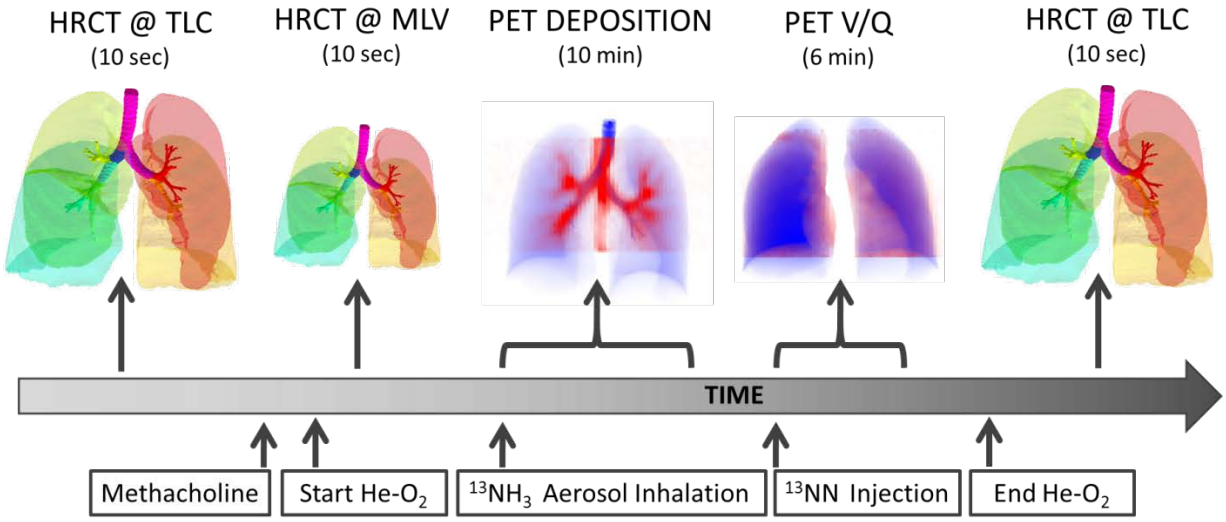

Figure 14: The imaging protocol for the He-O_2 group.

The imaging protocol was completed at Massachusetts General Hospital with IRB approval (Application No. 2011P000755). While breathing room air, the subject was positioned supine in the PET-CT camera and was imaged during a breath hold at total lung capacity (TLC) with HRCT. The subject was then fitted with nose clips and methacholine (MCh) was administered over five deep breaths using a DeVilbiss nebulizer and Rosenthal dosimeter (model 646, DeVilbiss Healthcare, Somerset, PA) at a concentration determined on a previous screening day to cause a 20% drop in FEV_1 (PC_{20}). The subject was then asked to breath via a sealed mouth piece from a breathing circuit (Figure 15) that delivered a premixed gas of 21% O_2 and 79% He. The circuit included a vibrating mesh nebulizer (Aeroneb Solo, Aerogen , Galway, Ireland) and an Idehaler holding chamber (Aerodrug, Cedex, France). After 5 minutes of free breathing the subject was imaged again with HRCT during a breath hold at his/her mean lung volume MLV determined from impedance plethysmgraphy during 30 seconds of steady tidal breathing before imaging.

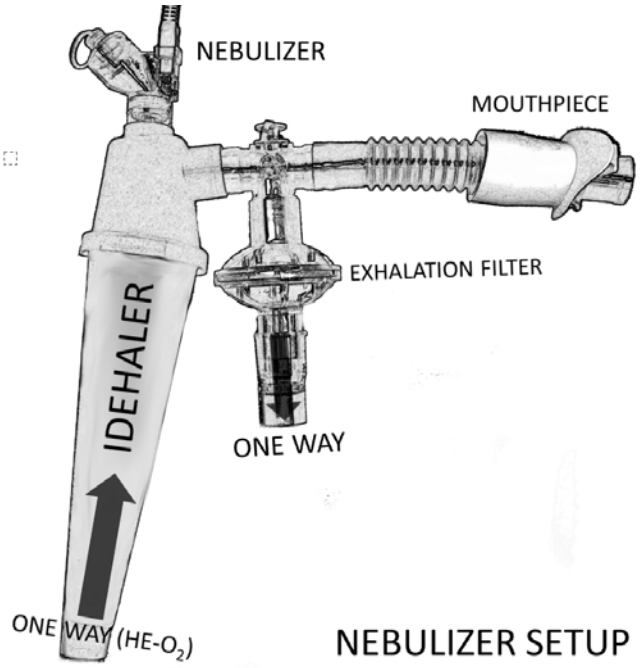

Figure 15: The breathing circuit used during nebulization. He-O_2 gas was stored in a Mylar bag at atmospheric pressure. Both carrier gases were supplied through the base of the Idehaler through a one way valve. After nebulization, the subject was switched to a second breathing circuit that continued to provide He-O_2 without the nebulizer. Changing the circuit eliminated noise in the deposition image arising from residual tracer in the nebulizer.

Following acquisition of the HRCT scan, 1 ml of ^{13}N-NH_3 labeled (1-4 mCi) isotonic saline was aerosolized and inhaled over a period of 2 minutes while breathing He-O_2. The particle sizes of the aerosol exiting the mouthpiece were previously characterized by laser diffraction to have a volume median diameter (VMD) of 4.9 μm and a geometric standard deviation GSD of 1.8 that was not significantly affected by the carrier gas[36]. At the end of the aerosol inhalation, the subject continued to breathe He-O_2. PET image acquisition of the ^{13}N-NH_3 tracer was conducted for 10 minutes starting with the beginning of the aerosol inhalation.

Once the aerosol deposition image collection ended, the distribution of specific ventilation was assessed with PET using the ^{13}NN bolus injection-washout method[59]. The method uses the low solubility of nitrogen in blood plasma to deliver the tracer to the lung; when an intravenous bolus of ^{13}NN in saline solution passes through the pulmonary capillary bed, it diffuses from the blood plasma into the alveolar airspace. Starting with the tracer injection, subjects were asked to hold their breath for 20 seconds at mean lung volume followed by normal tidal breathing. Dynamic PET images were acquired for 7 minutes starting simultaneously with the 13NN injection.

Imaging data was reconstructed in 4D and analyzed to evaluate the dimensionless values of relative specific depositions $_sD^*_{sl}$ and relative specific ventilation $_s\dot{V}^*_{sl}$, where *l* is the index of the lobe, and *s* of the subject. From these values and the activity measured in anatomically defined portions of the airway tree, the apparent net branching factor $\hat{\Pi}^*_{B.sl}$ and the apparent net escape fraction $\hat{\Pi}^*_{E.sl}$ were derived using the method previously described in the study breathing air[71]. The values of lobar retention needed to estimate the true net branching factors and escape fractions could not be directly measured from our imaging data[71].

Possible Effects of a Heterogenous Lobar Retention Fraction

We could not determine the actual fraction of the aerosol retained in the periphery. However, we evaluated the effect of two parameters that could have been influenced by the degree of regional lobar retention: the intersubject differences in the breathing frequency during nebulization f_N and the interlobar differences in mean parenchymal expansion during breathing $F_{VOL,sl}$, estimated from the HRCT image acquired at MLV as:

$$F_{VOL,sl} = \frac{V_{Gas,MLV,sl}}{V_{Tissue,MLV,sl}} \quad (40)$$

Lobes with high $F_{VOL,sl}$ could have reduced η^*_{sl} due to the combined effects of longer sedimentation distances and lower likelihood of impaction on the walls of the more distended airways. Inhaled particles by subjects breathing at higher f_N have less residence time in the periphery, and thus lower average retention $\overline{\eta_s}$. Because η^*_{sl} is the retention fraction of the lobe normalized to $\overline{\eta_s}$ [71], a lower average retention could amplify lobar differences in retention and result in a wider distribution of η^*_{sl}. Since the retention of a lobe is expected to be reduced by increasing f_N and $F_{VOL,sl}$, these measures may provide insight into retention fraction effects that could not be directly measured.

As with the air group, we could estimate a global retention fraction in the periphery $\overline{\eta_s}$ [71] using our analysis of the retention of mono-disperse aerosols by Kim et al. [55] demonstrating that $\overline{\eta_s}$ could be well described as a function of a single parameter: the average sedimentation distance d_s defined as the product of a stokes settling velocity v_s multiplied by the average residence time of a particle in the periphery t_s:

$$\overline{\eta_s} = 1 - e^{-\frac{d_s}{371\mu m}} \text{, where } d_s = v_s t_s \quad (41)$$

Assuming that this function holds for He-O_2, and after accounting for the 16% reduction of d_s caused by the more viscous He-O_2 mixture compared with air, $\overline{\eta_s}$ should not have increased by more than 6% in He-O_2 compared to air for the size range of the poly-disperse aerosols used in this study.

Statistical Analysis

Systematic differences among lobes in sD^*_{sl}, sD^*_{sl}/sV^*_{sl}, and $\hat{\Pi}^*_{E,sl}$, were tested using ANOVA with repeated measures. When differences were evident at the 5% alpha level, a Holm-Sidak test for multiple comparisons was used to test for individual differences between lobes [39]. It should be noted that no further correction was made for the different ways that we divided and explored our data (e.g. varied ways of characterizing the ventilation, deposition, ratios of depositions, ROIs, and numerous comparisons between the measured variables). All statistics are therefore exploratory and only intended to guide future studies.

In addition to evaluating heterogeneity among lobes, histograms of the voxel-by-voxel intrapulmonary distributions of sD^*_{sv} in each subject *s* were analyzed for their variance, skewness, and kurtosis to quantify their spread, symmetry and peakedness, respectively. To avoid boundary effects at the edge of the lung, only voxels that were separated from the edge of the lung by at least 10mm were considered in this analysis

Results

Aerosol Deposition Pattern in Air and He-O_2

No obvious differences in the aerosol deposition pattern could be detected between the 3D images of He-O_2 and air groups. This is supported by the visual similarity between the 2D projections of the images (Figure 16) and the lack of quantitative differences (

Table 4) among anatomical regions (AR). Note that the specific deposition in the central airways can be two orders of magnitude larger than the average deposition in the periphery as reported for air in our earlier work[7].

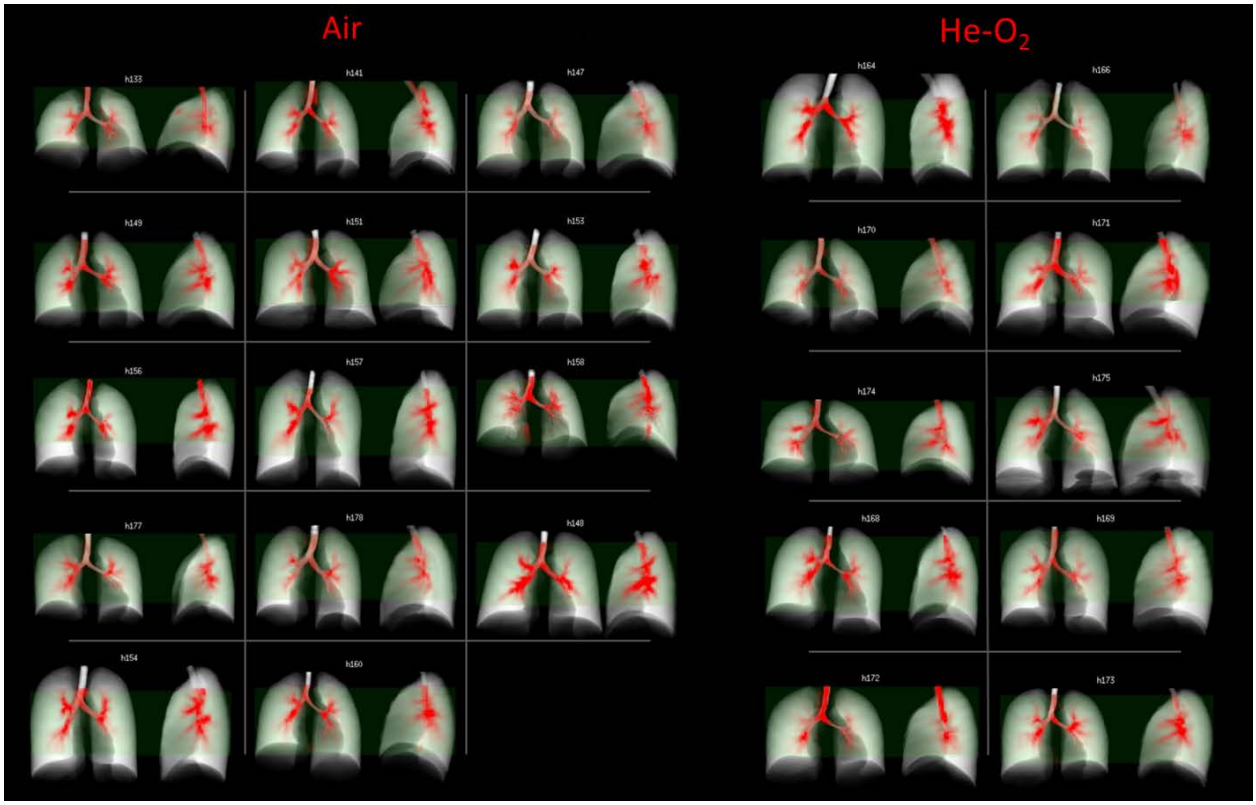

Figure 16: Maximum intensity projections for air and helium show similar highly centralized patterns of deposition. The PET field of view is shown in light green. Note that all of the 14 subjects in whom we had collected deposition data with air are shown in the figure.

Table 4: Average specific and total deposition by anatomical region (± SD). The relative specific deposition *sD** is a measure of the concentration of the aerosol compared to the average concentration in the periphery. The total deposition is the fraction of aerosol that deposited in the anatomical region, and is given as a percent of the total deposition past the carina (the total lung dose TLD).

AR	Location	Average *sD**		Total Deposition [% TLD]	
		Air	He-O_2	Air	He-O_2
LUL	Lobar Periphery	1.15 ± 0.23	1.08 ± 0.26	16.9 ± 3.40	19.5 ± 4.86
LLL		0.69 ± 0.25	0.69 ± 0.29	9.44 ± 4.41	12.0 ± 5.07
RUL		1.19 ± 0.14	1.12 ± 0.31	13.1 ± 1.83	17.3 ± 7.24
RML		0.82 ± 0.31	1.06 ± 0.52	4.59 ± 1.65	8.33± 4.38
RLL		1.06 ± 0.27	1.04 ± 0.39	15.9 ± 5.42	18.6 ± 8.66
LUL CA	Lobar Central Airways	166 ± 61	136 ± 69	4.77 ± 1.40	4.52 ± 1.16
LLL CA		113 ± 63	115 ± 60	4.43 ± 1.51	5.32 ± 1.85
RUL CA		199 ± 120	152 ± 76	4.02 ± 1.24	3.9 ± 1.85
RML CA		175 ± 96	194 ± 77	1.63 ± 0.76	2.37 ± 1.04
RLL CA		214 ± 137	208 ± 99	6.40 ± 1.73	8.19 ± 2.97
BINT	Extrapulm. Airways	68.5 ± 28.2	79 ± 42	1.76 ± 0.57	2.08 ± 0.98
RMB		47.6 ± 26.5	43.7 ± 28.2	1.61 ± 0.41	1.87 ± 1.24
LMB		91.3 ± 47.4	118± 59	5.50 ± 2.21	8.02 ± 3.29
TRC		47.6 ± 25.3	50.6 ± 28.4	9.87 ± 2.51	12.1 ± 5.25

The fraction of the aerosol that deposited past the carina in the periphery $D_{P,s} / D_{T,s}$ was also not statistically different between the two groups. While $D_{P,s} / D_{T,s}$ with He-O_2 was on average 1.2% higher than air, the upper 95% confidence interval for this difference was 7.4%. In other words, given the large intersubject variability in $D_{P,s} / D_{T,s}$ (~7%), we can only be certain that deposition in the He-O_2 is likely no more than 7.4% more peripheral than in air. Metrics describing the distribution of sD^*_{sv} in the lung periphery showed that the variance of deposition among voxels was 13% lower in He-O_2, the skewness was 20% higher, and the Kurtosis was 29% higher, but

these changes were not significantly different due to the large variability of these parameters among the subjects of both groups.

Table 2: Characterization of the specific deposition voxel histograms (Average ± SD)

Metric	Air	He-O_2
$D_{P,s} / D_{T,s}$	0.664 ± 0.062	0.678 ± 0.074
$\underset{v\in\zeta_s}{\text{median}}\left(sD^*_{sv}\right)$	0.472 ± 0.099	0.469 ± 0.084
$\underset{v\in\zeta_s}{\text{var}}\left(sD^*_{sv}\right)$	0.556 ± 0.163	0.483 ± 0.117
$\underset{v\in\zeta_s}{\text{skewness}}\left(sD^*_{sv}\right)$	2.53 ± 0.93	3.04 ± 0.87
$\underset{v\in\zeta_s}{\text{kurtosis}}\left(sD^*_{sv}\right)$	12.9 ± 9.1	16.6 ± 8.1

Comparing the Sources of Variability in sD* in Air and He-O_2

Taken as a whole, the distributions of sD^*_{sl} , sD^*_{sl} / sV^*_{sl}, and $\hat{\Pi}^*_{E,sl}$ were not systematically different between the groups (Figure 17). Except for $\hat{\Pi}^*_{E,sl}$, statistical differences among lobes that were evident in the air subjects were not present in the He-O_2 subjects. In both groups, the apparent escape fraction $\hat{\Pi}^*_{E,sl}$ was higher for the upper lobes than that the lower lobes within each lung (P<0.05). In the He-O_2 group this apical-basal gradient in $\hat{\Pi}^*_{E,sl}$ was also significant in the RML which had an average $\hat{\Pi}^*_{E,sl}$ higher than that of the RLL and less than that of the RUL (P<0.05).

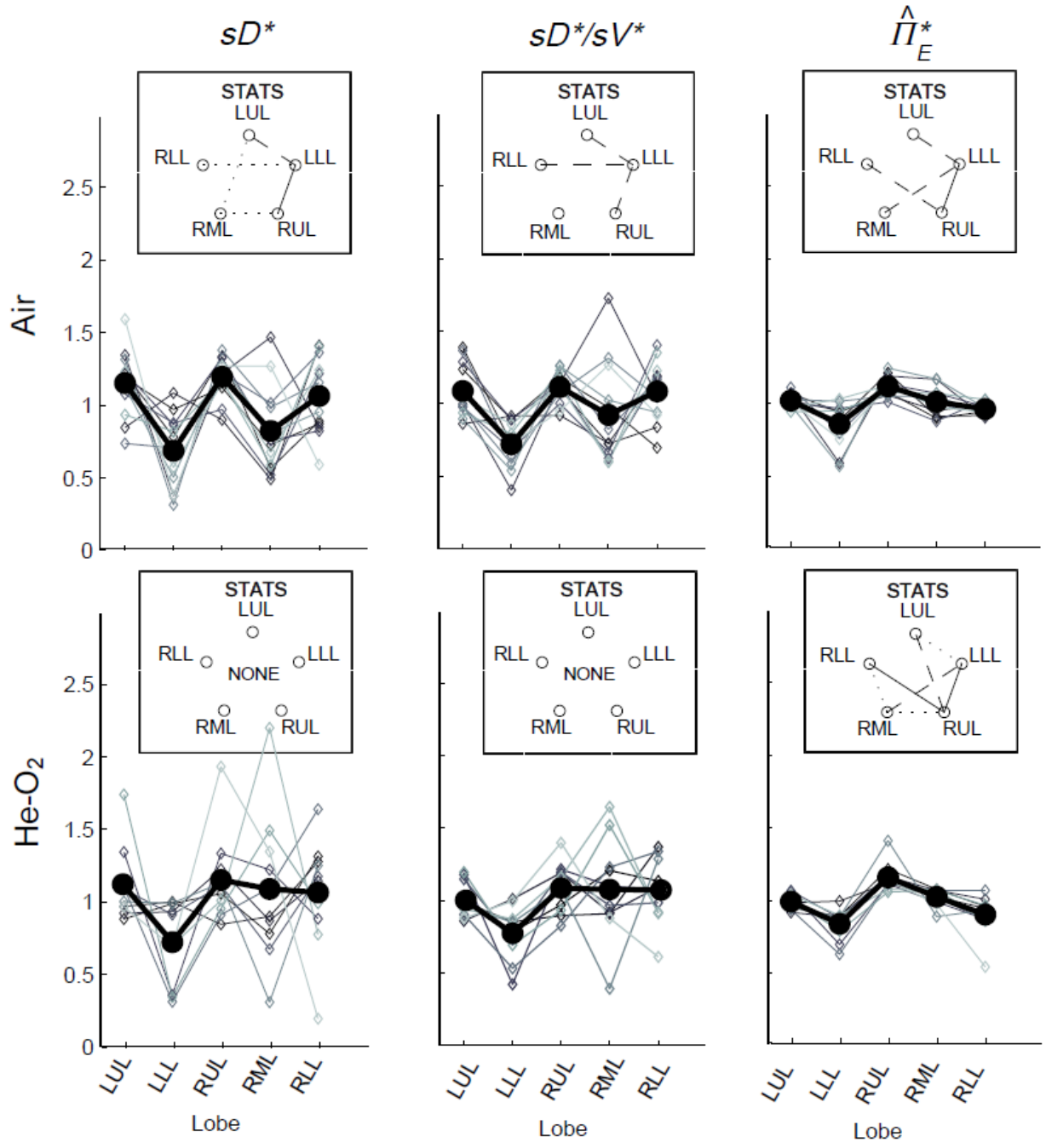

Figure 17: *sD** (*left column*) ,*sD**/*sV** (*center column*) , and the apparent escape fraction (*right column*) for each lobe in the air (*top row*) and He-O_2 (*bottom row*) subjects. Lobes of the same subject are connected with thin lines, and the average among subjects is shown with the circular markers and connected with thick lines. Statistical differences in parameters between any two lobes in the air group are depicted as a line connecting the lobes to the above each plot (solid is P<0.001, dashed is P<0.01, and dotted is P <0.05). Note also the systematic **apical-basal** gradient in apparent escape fractions in the right and left lungs of both groups.

The Relationship Between sD* and sV* May be Stronger in He-O_2 than Air

Both sD^*_{sl} and sV^*_{sl} tended to be more variable among lobes in He-O_2 than in air, and the correlation between sD^*_{sl} and sV^*_{sl} among all lobes was stronger for He-O_2 than for air (Figure 18). However, these differences were not statistically significant. There was large intersubject variability in the correlation between sD^*_{sl} and sV^*_{sl}, and the average of the subject-by-subject correlation coeficients of the groups (0.51 ± 0.29 in air, and 0.66 ± 0.32 in He-O_2) were not significantly different (P=0.28). However, when we considered only those subjects with uneven sD^*_{sl} (COV^2 > 0.03), the average of the correlation coefficient was higher among subjects (P<0.05) in the He-O_2 group (0.78 ± 0.13) compared with the air group (0.51 ± 0.29). The cut off value of 0.03 excluded the 2 subjects with lowest correlations in He-O_2 from the analysis and none in the air group. These subjects were not excluded from any other analysis in this chapter. Additionally, among the subjects breathing air, the correlation between *sD** and *sV** was high in subjects breathing with low f_N but was reduced in those with higher f_N ($corr(corr(sD^*,sV^*)_s,f_N)$= -0.71, P(*corr.* < 0) = 0.032, in air). In contrast, the correlation was high and was not affected by f_N among the subjects breathing He-O_2.

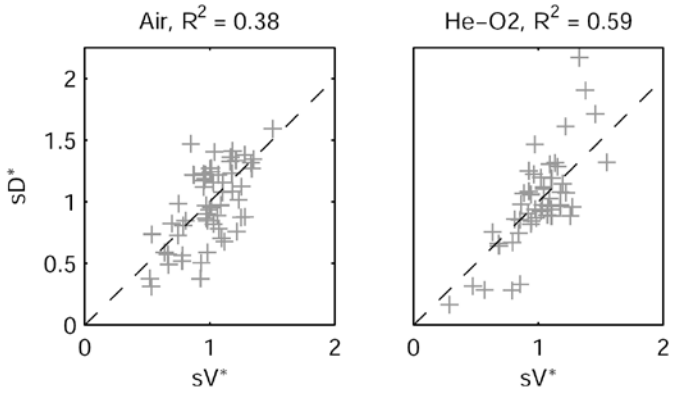

Figure 18: *sD** vs. *sV** for air (*left*) and He-O_2 (*right*), along with the correlation squared between the metrics. Helium tended to have a wider spread in *sD** and *sV**, with a tighter correlation between the metrics than air.

Table 5: Lobar variability in specific deposition and its influencing factors over the set S of all lobes of all subjects.

x_j	Gas	sV_{sl}^*	$\hat{\Pi}_{B,sl}^*$	$\hat{\Pi}_{E,sl}^*$
$\underset{j\in S}{\mathrm{var}}(x_j)/\underset{j\in S}{\mathrm{var}}(sD_j^*)$	Air	0.48	0.45	0.15
	He-O_2	0.38	0.29	0.15

While the air data showed weak correlations among the lobar measures of relative specific ventilation, the apparent net branching factors, and the apparent net escape fraction (**Error! Reference source not found.**), the He-O_2 data showed a significant and substantial correlation between ventilation and escape fractions with corr(sV_{sl}^* , $\hat{\Pi}_{E,sl}^*$) = 0.44, (P(corr.<0 = 0.0014).

Table 6: The square of the Pearson correlation coefficient between elements in Equation **(39)** for both groups over the set S including the lobes of all subjects. *(P<0.05)

X_j	Y_j	Gas	$\underset{j\in S}{\mathrm{corr}}(X_j,Y_j)^2$
sD_{sl}^*	sV_{sl}^*	Air	0.38
		He-O_2	0.59
sD_{sl}^*	$\hat{\Pi}_{B,sl}^*$	Air	0.38
		He-O_2	0.40
sD_{sl}^*	$\hat{\Pi}_{E,sl}^*$	Air	0.31
		He-O_2	0.33
sV_{sl}^*	$\hat{\Pi}_{B,sl}^*$	Air	0.014
		He-O_2	0.011
sV_{sl}^*	$\hat{\Pi}_{E,sl}^*$	Air	0.023*
		He-O_2	0.193*
$\hat{\Pi}_{B,sl}^*$	$\hat{\Pi}_{E,sl}^*$	Air	0.040
		He-O_2	0.010

The Relationship between F_{VOL}, sD*/sV* and f_N Was Not Present in the He-O_2 Group

In the 9 subjects breathing air with measurements of f_N , the relationship between F_{VOL} and *sD*/sV** among lobes for individual subjects had been found to be strongly modulated by the

frequency of breathing during nebulization (corr(corr(sD^*/sV^* ,F_{VOL}),f_N) = -0.97, P(corr. >0) < 0.0001), with those subjects breathing at a low frequency showing a strong positive relationship, and those breathing at a faster rate having a strong negative relationship. In the He-O_2 group these effects were not present (Figure 19).

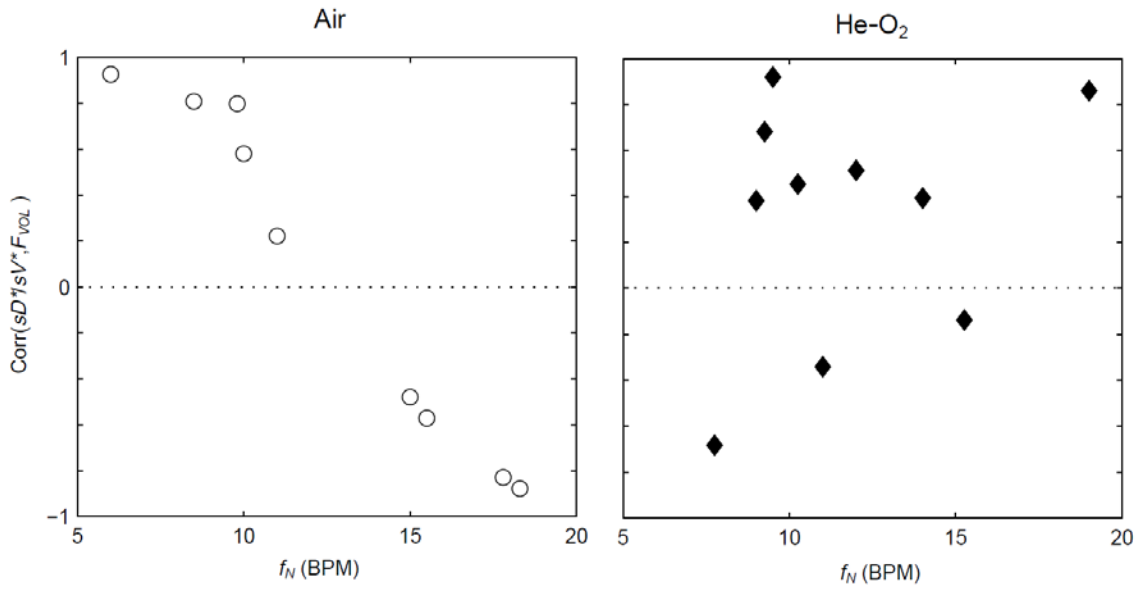

Figure 19: The correlation between sD^*/sV^* and F_{VOL} for each individual subject, plotted against nebulization breathing frequency for air (*left*) and He-O_2 (*right*). This relationship was strongly modulated by the breathing frequency for subjects breathing room air, but not for those breathing He-O_2.

Discussion

The primary aim of this study was to collect 3D distributions of aerosol deposition during He-O_2 breathing together with detailed anatomical and functional data to be used as appropriate boundary conditions in future CFD modeling analysis. As a second aim, and the central topic of the present report, we compared the results obtained from the He-O_2 group with those from the previous air group to test if average differences between the groups could be detected. We observed that: 1) due to large inter-subject variability, the general anatomical distributions of aerosol deposition observed in the two groups were not statistically different from each other, 2) In subjects showing variability in sD^* (COV^2>0.03), the correlation between ventilation and deposition was higher in the subjects of He-O_2 group compared with the air group. The correlation between sD^* and sV^* weakened among subjects breathing air at higher f_N , but not in subjects

breathing He-O_2 at higher f_N, 3) The dependence of sD^*/sV^* on f_N and lobar expansion observed among subjects breathing air was not detected in the group breathing He-O_2.

The Patterns of Deposition Were Similar Between the Groups

Due to high inter-subject variability, the distributions of aerosol deposition and ventilation among lobes in the air and He-O_2 groups were not substantially different from each other. This was the case whether we compared the images visually, quantified the deposition within anatomical regions, compared the characteristics of the voxel-by-voxel histograms, or quantified the sources of variability in deposition among lobes. While there was a tendency for the distributions of deposition and ventilation among lobes to be more variable in He-O_2 than in air, these results were not statistically significant. Additionally, from Figure 18 it is evident that the group breathing He-O_2 had a greater fraction of lobes with sD^* closer to the average ($sD^* = 1$) than air, together with a handful of lobes having sD^* values much larger and smaller than the average. This is quantified in a histogram of $abs(1-sD^*)$ (Figure 20) showing that 33% of the lobes in the He-O_2 group had an sD^* within 10% of the mean value, compared to just 13% in the air group. Also, only in the He-O_2 group lobes had sD^* values deviating by more than 80% from uniformity. These extreme values in sD^* corresponded to lobes in subjects with extreme values in sV^*(Figure 18). Additionally, although the variability among all lobes tended to be larger in He-O_2 group, the two subjects with the most uniform lobar sD^* were both from the He-O_2 group. Taken together, these findings support the possibility that He-O_2 could be effective in some 'responder' subjects and not in others[70]. At present, *a-priori* identification of those subjects is not possible and more knowledge on basic mechanistic factors affecting the distribution of ventilation and deposition are needed.

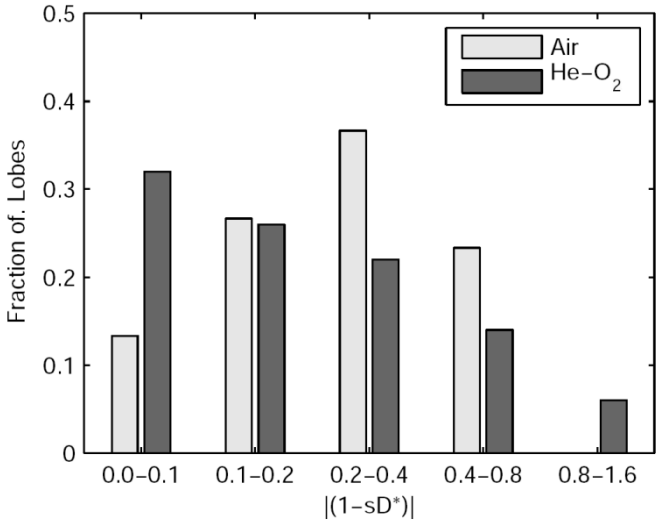

Figure 20: Histogram of the absolute difference of *sD** from unity. Note that the He-O_2 group has a greater fraction of lobes with *sD** deviating by less than 10% of the average compared with the air group, while only in the He-O_2 group did lobes deviate by more than 80% from the average.

The identification of 'responders' could come from computational fluid dynamic (CFD) models. Thus far, those models have shown lower aerosol deposition in the extrathoracic airways with He-O_2 [72], reduced turbulent mixing [14], more peripheral deposition and more homogenous ventilation[57]. However, experimental and clinical evidence testing the premise that He-O_2 results in increased peripheral deposition have not been conclusive. Aerosol bolus studies have shown lower overall deposition[58], with lower deposition in the upper airways, and increased deposition in the periphery[68]. On the other hand, 2D scintigraphy studies have had mixed results, with some showing either no difference in the upper airways [69] or among lung regions [73], and others showing reduced deposition in the upper airways[67]. Also using scintigraphy, another study reported increased lung aerosol deposition breathing He-O_2 compared to O_2 in pediatric subjects with severe airway obstruction, but not in subjects with lesser obstruction[74]. 3D imaging of aerosol deposition using SPECT-CT also showed variable results among two healthy and two asthmatic subjects, each imaged after inhaling aerosol suspended both in air and in He-O_2. Of these, only one of the subjects with asthma showed a detectable change in deposition pattern, with a reduction in deposition with He-O_2 within the central airways and an accompanying increase in the fraction of deposition within deeper generations[13, 19]. The present work is the first in-vivo study of the effect of ventilation distribution or aerosol deposition among parallel regions of the lung using helium oxygen as the carrier gas.

Given that the effects of He-O_2 on the pattern of aerosol deposition have not been consistently observed, it is not surprising that the clinical benefit of using He-O_2 as an aerosol carrier gas to deliver nebulized therapy in bronchoconstricted asthmatic subjects has also remained unclear. While some studies have shown improvements in FEV_1[77, 78], PEFR[78-80], FVC[78], clinical score[81], and intubation[80] and hospitalization rates[81], others have found little or no benefit from the He-O_2 in FEV_1[82, 83], PEFR[82, 83], FVC, clinical scores[83, 84] and hospitalization rates[85]. An excellent overview of these conflicting results is presented by Kim and Corcoran[76], who conclude that He-O_2 mixtures should only be considered for those patients who present with severe asthma. It has also been suggested that older subjects may show greater improvement[80], and that it may take time (>35 minutes of continuous nebulization with He-O_2) to show a benefit over 100% O_2[81]. Kim and Corcoran[76] noted that the aforementioned studies that demonstrated clinical benefit of using helium oxygen as a carrier gas[77-81] all used large volume nebulizers that could meet the minute ventilation of the subject without dilution of ambient air. This was not a factor in the present study where the aerosol was produced by a vibrating mesh nebulizer not driven by gas, an Idehaler served as a reservoir for the aerosol, the inhalation circuit delivered a fixed gas composition independent of breathing flow rates, and the nebulization circuit included a tight fit mouthpiece and nose clips to prevent dilution of the He-O_2 with ambient air (Figure 15).

The Relationship between sD* and sV* May be Stronger in He-O_2 than Air

The lobar distribution of aerosol deposition tended to follow that of ventilation more closely in the He-O_2 group compared with the air group when all lobes and subjects were grouped in the analysis. The difference in the correlation between *sD** and *sV** was significant when comparing subjects with variability in *sD** (COV^2>0.03). The two subjects that were excluded from the He-O_2 data had low variability in both *sD** and *sV**. Excluding these subjects from the analysis is justifiable given that subjects with uniform distributions of *sD* and sV** should only show the lack of correlation between the random errors in the estimates of *sD** and *sV**. The presence of limited error may also contribute to the trend for stronger correlations between *sD** and *sV** in He-O_2; even if the physical correlations between *sD** and *sV** were similar between the gases, if the error is similar between the groups, higher correlations would be measured in the He-O_2 data due to the higher spread in both *sD** and *sV** in some subjects of the He-O_2 group (evident in Figure 18).

Ventilation was positively correlated with the apparent net escape fraction for He-O_2 but not for air. Based on our theoretical framework, this covariance could be partially responsible for the trend for closer relationships between ventilation and deposition in He-O_2; the effect of *sV** on *sD** includes an effect of the net escape fractions so that a higher overall correlation between *sV**

and *sD** could be caused by a correlation of *sV** with the apparent escape fraction effects in He-O_2 that are not present in air. This is also likely the reason why the relationship between *sD** and *sV** appears to follow a slope greater than unity in Figure 18 in He-O_2. Why might there be positive correlation between *sV** and the apparent escape fractions? One could imagine that severely constricted airways might both collect aerosol and result lower subtended ventilation resulting in a low apparent escape fraction and a low *sV**. However, we might also expect reduced apparent escape fraction due to higher aerosol velocities with greater central impaction among lobes with higher ventilation. It is also unclear why this effect might only be detected in He-O_2 but not in air. It may be that the signal is in fact present in air, but could not be discerned without the elevated variability in lobar *sV** present in some of the subjects breathing He-O_2.

The corr(*sD**, *sV**) weakened among subjects breathing at higher f_N in air but not in He-O_2. One could postulate that this effect may have been caused by increased heterogeneity in central deposition driven local regions of turbulence in central airway during air breathing at high f_N that were reduced during He-O_2 breathing. However, if this effect was present it should have been reflected in differences in the apparent escape fractions between the carrier gasses, yet Figure 17 shows the similarity in apparent escape fractions between the groups. Additionally, there was no evidence of increased variability in the apparent net escape fractions among lobes with increased f_N for either carrier gas.

In fact, the parameter that seems to best organize the apparent escape fractions was the position of the lobe on the apical-basal direction; $\hat{\Pi}^*_{E,sl}$ was both higher for the upper lobes compared with the lower lobes of both lungs and in the He-O_2 group this gradient in $\hat{\Pi}^*_{E,sl}$ also included the RML. This too is surprising; one would have expected the lower (more caudal) lobes, which tend to have larger caliber airways and fewer sharp turns in their central airways than the upper lobes, to have a *higher* escape fractions.

The Relationship among F_{VOL}, sD*/sV* and f_N is Only Present in the Air Group

The breathing frequency during nebulization strongly modulated the correlation of *sD**/*sV** and lobar inflation among subjects in the air group. This was not the case in the He-O_2 group. One hypothesis behind the finding in air is that there was reduced aerosol retention in those lobes that were more inflated; the greater the inflation, the longer sedimentation takes to complete, and impaction becomes less likely in the distended airways. At higher breathing frequencies the time that the aerosol has to sediment in the periphery is reduced which lowers the retention of all lobes in the lungs. If this leads to lower overall retention among lobes, small differences in retention

among lobes due to differences in inflation can generate greater differences in the *relative* retention η_{sl}^{*} among lobes affecting the variability of *sD** (Eq. (38)). Together with a bias for lower deposition in the less inflated LLL due to a lower net escape fraction, this hypothesis begins to explain the strong relationship seen in air. It is unclear why this signal disappeared in He-O_2; particle sedimentation with He-O_2 is expected to be similar or slightly lower than in air[58], and the impaction effects are also expected to be similar in the laminar flows of the periphery[57]. It should be noted that two of the three subjects that had a negative correlation of *sD*/sV** and lobar inflation while breathing He-O_2 were the two subjects with COV^2(*sD**)< 0.03. These subjects also had a low variance in *sV*,* and in the presence of error in the deposition and ventilation estimates, the *sD*/sV** ratio may not be very meaningful. Whether or not these subjects are included in the analysis, the strong modulation of f_N on the correlation seen in air was not present in He-O_2.

Methodological Limitations

Limitations in the measurements of deposition and ventilation have been discussed at length in previous publications[7, 71], and the reader is referred to those works for a more complete discussion of these limitations. Several important points are important to reiterate for the comparison of breathing He-O2 and air: part of the variance in the apparent net branching factor includes measurement errors in both ventilation and deposition. In contrast, the apparent net escape fraction is exclusively determined from the deposition image, and thus not affected by possible errors in the estimates of ventilation. This may be, in part, the cause for stronger statistical differences between lobes in the apparent escape fractions (Figure 17, *right column*). However, the effect of these potential measurement errors in ventilation was not high enough to prevent the strong correlation between sV* and sD* in helium at all breathing frequencies.

Even if helium oxygen could have a significant effect on the distribution of ventilation in some subjects, there are several potential reasons why it may not have been detected in the present study. First is the large inter-subject variability in the distribution of *sV** and *sD** in bronchoconstricted subjects with asthma. These differences could be reduced in protocols designed with crossover measurements between air and He-O_2 in each subject. Differences in response between He-O_2 and air reported in the literature have generally been smaller than the inter-subject differences measured for each gas (e.g. the data presented in Darquenne et al.[58]). Therefore, without a crossover protocol (as were used in limited studies with SPECT-CT[75]), very large group numbers would be required to show statistical differences between the gases. However, the large inter-subject variability implies limited clinical relevance unless 'responders' can be readily identified. Additionally, the highly central deposition pattern observed in bronchoconstricted

subjects may have limited our sensitivity to peripheral deposition; it is possible that if aerosol inhalation is conducted with a controlled breathing pattern conducive to a more peripheral deposition pattern (deep breaths with prolonged breath holds), or with smaller aerosols, we could have observed significant differences. However, even when crossover design was used with a pattern of ventilation conducive to peripheral deposition, a variable response to He-O_2 was still be present among subjects. In the SPECT-CT study [75], only one of the two asthmatics subjects, and none of the healthy subjects, responded with a more uniform distribution of deposition with He-O_2. This reinforces the importance of using CFD analysis to better understand why and who may or may not respond to He-O_2.

The subjects included in the present study were young mild asthmatics who were challenged with a PC_{20} concentration of methacholine. It has been observed that the benefits of He-O_2 for inhaled therapy are more prominent in both older subjects[80] and in those subjects with severe bronchoconstriction[74]. It is therefore possible that older and more severely constricted subjects could be better candidates for aerosol delivery with He-O_2 than the young mildly asthmatic subjects studied here. Finally, this study, along with the parallel study in air, focused on heterogeneous distribution of the aerosol among the lobes, and for this reason did not image the mouth, throat and upper trachea. If helium oxygen has lower deposition in extra-pulmonary regions, it would not have been included in our PET images. In fact, if a greater fraction of larger sized particles reached the carina with He-O_2, this would have resulted in an *increase* in central deposition within the PET field of view masking any preference of He-O_2 for deeper deposition in relation to the total inhaled dose.

He-O_2 can influence the size of the aerosols emitted from the nebulizer[74, 86-88], and potentially the rate of hygroscopic growth in the lung. Martin et al. [89] found that particle volume median diameter (VMD) at the exit of Aeroneb Solo vibrating mesh nebulizers used with a T piece was larger for medical air (VMD of 5.5 ± 0.1 μm) than for helium–oxygen (VMD of 4.3 ± 0.1 μm) when the gases were supplied without humidification. Darquenne at al.[58] have noted that greater hygroscopic effects can be expected with He-O_2 than with air, and this is supported by the results of Martin et al. [89] who found that in the presence of humidified gasses size differences between air and He-O_2 were smaller than for dry gases. Observed differences between gases were attributed to increased evaporation of nebulized droplets in He-O_2 versus air between the nebulizer and laser diffraction measurement volume[30]. In the present study, the output of the nebulizer-holding chamber setup was tested using laser diffraction (Helos/BF with Inhaler module; Sympatec GmbH, Germany) in dry gasses at the Air Liquide laboratories, and droplet size distributions were found

not to be sensitive to the differences in the inhalation flow rate or carrier gas. This is very likely due to the significantly increased droplet concentration that results from use of the holding chamber. Just as humidification limited droplet evaporation in the Martin study[30], use of the holding chamber in the present study increased droplet concentration to the extent that any small initial amount of evaporation from droplets rapidly saturated the surrounding gas phase, thereby limiting further evaporation. Such effects resulting in negligible hygroscopic size changes have been well described for high concentration aqueous aerosols[90], and mathematical models have predicted that only trivial differences in hygroscopic size changes within the lung occur between air and He-O_2, for droplet mass fractions typical of pharmaceutical nebulizers[91]. As a result, it is unlikely that particles grew to a significant extent in the humid lungs in either He-O_2 or in air.

We used radiolabeled isotonic saline to identify the deposition pattern in both groups. While other studies have included a bronchodilator in the aerosol [77, 78, 80-85], the introduction of an agent that interacts with the ventilation pattern would have interfered with our ability to identify the actual ventilation distribution over the entire course of nebulization. Additionally, in contrast with other studies[12, 57, 67, 68, 75] we did not control the breathing pattern of the subjects; in our measurements the subjects were allowed to breathe spontaneously at their chosen breathing frequency and tidal volume. This provided us with a span of breathing patterns that might be clinically expected, and the range of f_N allowed us to observe the influence of breathing frequency during inhalation on other factors.

In summary, the present study found no systematic differences in the pattern of aerosol deposition within the lungs and airways of the group breathing He-O_2 and the group breathing room air. The clustering of more lobes around average deposition in several subjects is balanced by increase heterogeneity in lobes with extremes ventilation and deposition in others. Amid conflicting reports, some studies have found that He-O_2 has lower deposition in the mouth, throat and upper airways, and greater deposition in the periphery[67, 68]. It has also been suggested He-O_2 can homogenize ventilation and aerosol deposition among in bronchoconstricted subjects[57, 92]. The large variability among subjects precluded the significant detection of either effect between the two groups of young bronchoconstricted mild asthmatic subjects that were studied, and a number of additional limitations with the present work bound the conclusions that we can draw; it remains possible that stronger effects might be observed in an older population and among subjects with more severe asthma. However, the quantitative 3D distributions of aerosol deposition during He-O_2 and air breathing, along with detailed anatomical and functional data collected in this work, may be used to validate CFD analysis on an individual basis. It is hoped that such validated and

physiologically informed computational models will improve our understanding of how and for whom using He-O_2 as a carrier gas for aerosol therapy may provide benefit.

Acknowledgements

Research reported in this chapter was supported by the National Institutes of Health under award number R01HL68011. The content is solely the responsibility of the authors and does not necessarily represent the official views of the National Institutes of Health. Additional support was provided by American Air Liquide Inc., and Aerogen is thanked for providing the vibrating mesh nebulizers at no cost.

Author Disclosure Statement

This work was sponsored in part by American Air Liquide Inc. Ira Katz, Andrew Martin, and Georges Caillibotte were employed by Air Liquide during the execution of this study. Air Liquide sells helium-oxygen gas. However, the Helium-Oxygen mixture used in this study was purchased from Airgas and there was no undue influence of Air Liquide on the design of this study, the interpretation of its results, or on the preparation of this manuscript.

Chapter IV: Pendelluft in the bronchial tree

Elliot E. Greenblatt[1,4], James P. Butler[2,3], Jose G. Venegas[4], and Tilo Winkler[4]

[1] Massachusetts Institute of Technology, Cambridge MA, 02139
[2] Molecular and Integrative Physiological Science Program, Department of Environmental Health, Harvard School of Public Health, Boston, MA 02115, United States
[3] Division of Sleep Medicine, Departments of Medicine and Neurology, Harvard Medical School and Brigham and Women's Hospital, Boston, MA 02115, United States
[4] Massachusetts General Hospital and Harvard Medical School, Department of Anesthesia and Critical Care, Boston, MA, USA

This chapter has been published in the Journal of Applied Physiology[8], and the text and figures are reproduced here with the permission of the publisher.

Abstract

Inhomogeneous inflation or deflation of the lungs can cause dynamic pressure differences between regions and lead to interregional airflows known as pendelluft. This chapter first uses analytical tools to clarify the theoretical limits of pendelluft at a single bifurcation. It then explores the global and regional pendelluft that may occur throughout the bronchial tree in a realistic example using an in-silico model of bronchoconstriction. The theoretical limits of pendelluft volume exchanged at a local bifurcation driven by sinusoidal breathing range from 15.5% to 41.4% depending on the relative stiffness of the subtended regions. When non-sinusoidal flows are considered, pendelluft can be as high as 200% V_{in}. At frequencies greater than 10Hz the inertia of the air in the airways becomes important and the maximal local pendelluft is theoretically unbounded, even with sinusoidal breathing. In a single illustrative numerical simulation of bronchoconstriction with homogenous compliances the overall magnitude of global pendelluft volume was less than 2% of the tidal volume. Despite the small overall magnitude, pendelluft volume exchange was concentrated in poorly ventilated regions of the lung, including local pendelluft at bifurcations of up to 13% V_{in}. This example suggests that pendelluft may be an important phenomena contributing to regional gas exchange, irreversible mixing, and aerosol deposition patterns inside poorly ventilated regions of the lung. The analytical results support the concept that pendelluft may be more prominent in diseases with significant heterogeneity in both resistance and compliance.

Keywords

Ventilation distribution, ventilation mechanics, gas exchange, asthma, computational modeling

Introduction

Inspiratory and expiratory airflows in healthy lungs are relatively uniform throughout the bronchial tree. However, in pulmonary diseases or under abnormal conditions, this uniform pattern can be disturbed; inhomogeneous inflation or deflation of the lungs can cause dynamic pressure differences between different regions which in turn lead to interregional airflows. This effect is referred to as pendelluft ('Swinging Air') because gas is passed back and forth between the different regions of the lungs.

Pendelluft occurs when regions of the lung have different dynamics of regional inflation and deflation. For example, in a lung with two regions of equal compliance inspiratory airflow is diverted away from a region with higher resistance (R), and incomplete equilibration leads to lower

end-inspiratory pressure in the region with higher resistance compared to the other region. If the inspiration is followed by a pause – having zero flow at the airway opening – the pressure difference will cause pendelluft flow from one region to the other until the pressures are equilibrated. If the region with the higher resistance also has a greater compliance (i.e. it is less stiff) than the other region, more pendelluft flow will be needed to balance the pressures throughout the lungs. Experimental evidence and theoretical aspects of pendelluft due to varied resistance and compliance were first described in a classic paper by Otis et al. in 1956 [93], which included an excellent analysis of frequency dependence of resistance and compliance at a bifurcation as well as a theoretical upper limit for pendelluft.

Clinically, pendelluft can be observed during mechanical ventilation of patients with unilateral chest or lung injury, where the two lungs can sometimes be seen inflating and deflating out of phase with each other [94, 95]. More subtle pendelluft is sometimes observed as a gradual drop in pressure during an end-inspiratory pause which may be caused by airflow between the different regions of the lungs. There is emerging evidence of pendelluft in bronchoconstricted asthmatics [96], in subjects with COPD [97], and during mechanical ventilation under certain conditions including spontaneous effort [98].

At breathing frequencies much higher than those at rest, differences in how air mass within parallel regions of the lungs respond to rapid pressure changes (characterized by their inertance, L) can also lead to pendelluft. This kind of pendelluft has been postulated to aid gas exchange during high frequency ventilation [99-101]. Although this effect was not explicitly included in the analytical description of pendelluft by Otis et al., their mathematical model would allow adding inertive terms. Other investigators included inertance in more complicated analytical descriptions [99, 101], and in a sophisticated model of airflows in an airway tree [102].

Since Otis' 1956 paper, work on pendelluft at a single bifurcation has continued analytically, numerically, and experimentally. For example, pendelluft can affect gas transport by displacing air in the anatomical dead space within the volume of the airways [103]. It has also been shown that pendelluft can be observed even in symmetrical bifurcations if instabilities (like those that emerge from nonlinearities in airway resistance) are considered [104]. Additionally, pendelluft may be an important physiological phenomenon for irreversible particle and gas mixing in the bronchial tree [105, 106].

Pendelluft in a multibranching bronchial tree is more complicated than that at a single bifurcation, as it may occur at several bifurcations. In particular, pendelluft that occurs at multiple airway bifurcations between the central airway and the terminal units results in some form of stacking or propagation of the effects of pendelluft across airway generations. Pendelluft throughout the tree increases the overall tidal expansion of the acini, albeit with an uncertain combination of fresh gas and gas that has already been resident elsewhere in the lungs. We reasoned that this additional *pendelluft volume* could be explored using an numerical model of the airway tree during bronchoconstriction [1]. This model would thus permit quantitative exploration of the magnitude and effect of pendelluft within a bronchial tree in an illustrative example.

This chapter has two distinct aims that are mutually supportive. First, to clarify the definition, causes, and magnitude of pendelluft. To this end, we use analytical tools to define a generalized quantitative definition of pendelluft, identify its limits, and evaluate its magnitude using analytical methods. We then extend this definition to include pendelluft throughout a bronchial tree. The second aim of the chapter is to provide an example of local and regional effects of pendelluft on airflow and ventilation in a realistic context using an in-silico model of bronchoconstriction. We then use the numerical simulation to explore the frequency dependence of global pendelluft volume and the conditions for which the inertance inertia of the airways becomes important.

Nomenclature

$\dot{V}_j, V_j$ Flow and tidal volumes of the jth daughter airway in a bifurcation (j =1,2 for all subscripts j).

V_k Tidal volume passing through the kth airway.

$\dot{V}_{in}, V_{in}$ Inlet flow and (tidal) volume to a bifurcation; depending on the context it may be related to the whole airway tree or a subtree.

$\dot{V}_{P,j}$ Pendelluft flow in the jth daughter airway of a bifurcation.

$\dot{V}_{PB,k}, V_{PB,k}$ Pendelluft flows and volumes at the kth bifurcation. In the context of a local bifurcation the subscript k is omitted.

V_P Pendelluft volume in an airway tree (global) or subtree (regional).

$V_{AP,j}$ The aggregate pendelluft volume passing through the j[th] daughter airway in a bifurcation.

$V_{AP,in}$ The aggregate pendelluft volume passing through the parent airway of a bifurcation.

$V_{B,j}$ The bulk volume that directly passes through the j[th] airway of a bifurcation without experiencing pendelluft.

β The set of bifurcations in an airway tree or subtree.

T The set of terminal airways in an airway tree or subtree.

R_j, C_j, L_j, Z_j The (frequency dependent) resistance, compliance, inertance and impedance of the j[th] airway of a bifurcation and its subtended region.

τ_j^* Model dependent non-dimensional time constant of the j[th] airway of a bifurcation and its subtended region.

κ Non-dimensional compliance or inertance ratio of the daughter airways and their subtended regions.

Methods

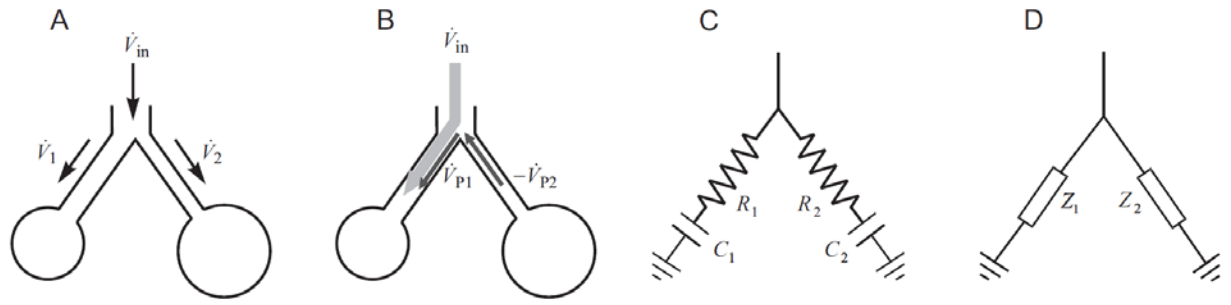

Figure 21: Schematics of single bifurcation models to describe pendelluft. (A) Definition of local parent flow and daughter flows, (B) Example of a pendelluft flow condition at the beginning of inspiration, note that the pendelluft flow going from one daughter–negative flow direction–into the other, combining with parent flow here in the left branch. Flows in the two daughters have opposite signs. (C) A resistance-compliance model of a bifurcation, (D) A general complex impedance model of a bifurcation.

Pendelluft Flow, Volume, and Ventilation Definition at a bifurcation are based on an earlier definition by Otis et al. [93]. Despite the complicated dynamics of airflows during pendelluft,

Otis et al. found an analytical description of the pendelluft volume at a bifurcation over a breathing period by using a circuit model of the lungs including resistances and compliances (Figure 21). Otis defined the relative pendelluft volume at a given bifurcation as the excess in the sum of the two daughter airways' tidal volumes relative to the tidal volume delivered through the parent airway. This pendelluft volume exchanged between regions increases the sum of the daughter tidal volumes without affecting the parent tidal volumes. This ratio quantifies pendelluft at a bifurcation.

We seek to extend this definition to include pendelluft flow over time, understand its limitations, and to ultimately use it to characterize the intergenerational aggregation of pendelluft throughout the global bronchial tree. However, before quantifying this aggregation, it is helpful to first identify the features that characterize pendelluft flow originating at an individual bifurcation: 1) Pendelluft flow occurs if and only if the flows in the daughter branches have opposite sign (Figure 21B). 2) Pendelluft flow passes from one daughter to the next and is therefore equal in magnitude in both daughters. 3) This magnitude is equal to the smaller flow of the two daughters which flows in the opposite direction as the parent and is entirely pendelluft. If there is no flow through the parent then both daughter flows are equal in magnitude and both are entirely pendelluft. 4) The direction of the pendelluft flow in each of the daughter airways is the same as direction of the total flow in the airway. These observations lead to the following definition of pendelluft flow emerging at an individual bifurcation:

$$\dot{V}_{P,j} = \begin{cases} \operatorname{sgn}(\dot{V}_j)\min(|\dot{V}_1|,|\dot{V}_2|); & \operatorname{sgn}(\dot{V}_1) \neq \operatorname{sgn}(\dot{V}_2) \\ 0; & \operatorname{sgn}(\dot{V}_1) = \operatorname{sgn}(\dot{V}_2) \end{cases} \quad [42]$$

The subscript *j* indicates either of the two daughter airways in a bifurcation (*j* =1,2 for all subscripts in this chapter). $\dot{V}_1, \dot{V}_2$ are the overall flows, and $\dot{V}_{P,1}, \dot{V}_{P,2}$ are the pendelluft flows. The total bifurcation pendelluft flow $\dot{V}_{PB}$ is the sum of the magnitude of the daughter pendelluft flows and is signed (arbitrarily) with $\dot{V}_1$:

$$\dot{V}_{PB} = \operatorname{sgn}(\dot{V}_1)\left(|\dot{V}_{P,1}| + |\dot{V}_{P,2}|\right) = \dot{V}_{P,1} - \dot{V}_{P,2} = 2\dot{V}_{P,1} = -2\dot{V}_{P,2} \quad [43]$$

An equivalent definition to the one presented in Equations [42] and [43], but without the piecewise character of Eq. [42] and the minimum function is:

$$\dot{V}_{PB} = \mathrm{sgn}(\dot{V}_1)\left(\left|\dot{V}_1\right| + \left|\dot{V}_2\right| - \left|\dot{V}_{in}\right|\right) \quad [44]$$

where $\dot{V}_{in}$ is the parent flow, which by conservation of mass satisfies $\dot{V}_{in} = \dot{V}_1 + \dot{V}_2$. Integration of the absolute amount of pendelluft flow over the breathing period T yields the local pendelluft volume at a bifurcation:

$$V_{PB} = \frac{1}{2}\int_0^T \left|\dot{V}_{PB}\right| dt = \frac{1}{2}\left(\int_0^T \left|\dot{V}_1(t)\right| dt + \int_0^T \left|\dot{V}_2(t)\right| dt - \int_0^T \left|\dot{V}_{in}(t)\right| dt\right) = V_1 + V_2 - V_{in} \quad [45]$$

where the volumes V_{PB}, V_1, V_2, V_{in} are defined as:

$$V_x = \frac{1}{2}\int_0^T \left|\dot{V}_x\right| dt \quad [46]$$

for any subscript x.

Note that V_{in} at the carina is the conventional tidal volume V_T of the whole lung, and the factor of ½ converts the integral of the absolute airflow over the breathing cycle to V_T; this is equivalent to an integral over inspiration or expiration only – provided there are no breath-to-breath changes in end-expiratory lung volume, which would require an average over multiple breathing cycles. The relative pendelluft volume at a bifurcation is defined as the pendelluft volume normalized by the local tidal volume delivered through the parent airway, which matches the description of Otis et al. [93]:

$$\frac{V_{PB}}{V_{in}} = \frac{V_1 + V_2 - V_{in}}{V_{in}} \quad [47]$$

Pendelluft can occur at many bifurcations throughout a given region of the bronchial tree, and its aggregation over the generations of the airway tree determines the overall increase in ventilation of the region. The regional pendelluft volume (denoted V_P) is normalized to the tidal volume feeding the region (denoted V_{in}) to yield the normalized regional pendelluft volume V_P/V_{in}. For the set of bifurcations β within the tree or subtree, and the set of terminal airways of the tree or subtree T:

$$\frac{V_P}{V_{in}} = \frac{\sum_{k\in\beta} V_{PB,k}}{V_{in}} = \frac{\sum_{k\in T} V_k - V_{in}}{V_{in}} \qquad [48]$$

Note that when the set includes the entire tree, V_P/V_{in} is the global pendelluft. Also, note that the regional pendelluft is evident from the sum of tidal volumes of the terminal airways compared to the inlet tidal volume. As proof of this, consider a tree with two generations and three bifurcations. Summing the pendelluft of these bifurcations (each given by Equation [45]) results in an algebraic combination of the airway tidal volumes that simplifies to the sum of tidal volumes of terminal units minus the inlet tidal volume. Normalizing by the inlet tidal volume gives the result shown in Equation [48]. Note the terminal airways used in Equation [48] are those at the end of any defined portion of the airway tree with a single inlet, and need not be those airways that directly feed the compliances. Therefore, the regional relative pendelluft definition in Equation [48] reduces to the bifurcation definition in Equation [47], since a single bifurcation may be considered as a subtree with two terminal airways.

While the regional pendelluft volume is a quantification including all local pendelluft volumes in a region, it does not show how the local pendelluft generated at bifurcations propagates through the airway tree. To quantify how pendelluft is distributed throughout the bronchial tree, we define the aggregate pendelluft volume $V_{AP,j}$ as the volume through the j^{th} daughter airway of a given bifurcation, that has accumulated from pendelluft in that or more proximal bifurcations. This volume combines with bulk flow $V_{B,j}$ that has never experienced pendelluft in the total flow through the airway V_j :

$$V_j = V_{AP,j} + V_{B,j} \qquad [49]$$

Recall that the subscript *j* indicates either of the two daughter airways in a bifurcation (*j* =1,2 for all subscripts in this chapter).

The aggregate pendelluft itself is a combination of the local pendelluft $V_{P,j}$ and a fraction of the aggregate pendelluft of the parent airway $V_{AP,in}$. Because the daughter airways cannot distinguish bulk volume from aggregate pendelluft volume, this fraction is the same as the fraction of ventilation that goes to that airway.

$$V_{AP,j} = V_{AP,in} \frac{V_j}{V_1 + V_2} + V_{P,j} \quad [50]$$

Note that the earlier definition of local and regional pendelluft considered pendelluft that emerges in a bifurcation or subtree, without considering pendelluft from more proximal bifurcations in the bronchial tree that can be that can arrive through the parent airway. In contrast, the aggregate pendelluft deals with this issue directly, and considers the total pendelluft driven volume that passes through a given airway.

This concludes our definitions of pendelluft flow, and the volume of local, regional, and aggregate pendelluft. We next use analytical methods to evaluate the magnitude of pendelluft volume at a single bifurcation.

Analytical Characterization of Pendelluft in a model with linear elements can be illustrated using the electrical analogues of resistance and compliance (Figure 1C), or more generally with impedance elements (Figure 1D). The components represent two daughter branches and subtended regions at any bifurcation in the tree. The amplitude of a sinusoidal flow through an impedance is given by the amplitude of the driving pressure divided by the magnitude of the impedance.

When such a system is driven with a single sinusoidal frequency the pendelluft volume over a breathing period can be expressed directly in terms of these impedances:

$$\frac{V_{PB}}{V_{in}} = \frac{|Z_1| + |Z_2|}{|Z_1 + Z_2|} - 1 \quad [51]$$

where Z_1 and Z_2 are the complex impedances of the daughters (Figure 21D).

This equation is equivalent to the one found originally by Otis et al. [93]. It is limited to a single bifurcation driven with a single frequency, and is evaluated over a complete period. Note that the impedances are complex, and the absolute value operator is that defined for complex numbers. Given that the initial definition of pendelluft flow (Eq. [42]) includes a piecewise definition, a minimum function, and absolute value operators, it is remarkable that the pendelluft volume of the breathing cycle can be expressed in this simpler form. This form permits calculations in networks of impedances such as the airway tree. However, note that Eq. [51] remains non-analytical because of

the absolute value operators; meaning that it is not additive and harmonic decomposition cannot be used to evaluate non-sinusoidal driving pressures.

Equation [10] can be derived directly from Eq. [45], but some observations simplify this considerably: The local pendelluft volumes can be evaluated using only the amplitudes of the input flow and the flow through the daughters without directly considering the phase difference between the flows. This is because integrating over a complete cycle to identify the tidal volume of each of the daughters' subtended regions is independent of the phase difference (even though the phase difference between the daughters is important, indeed key to the existence of pendelluft). These subtended volumes are determined by the magnitude of the daughter impedances, and after normalizing to the input flow Equation [51] is reached. See also the geometric construction in Figure 24.

The pendelluft equation (Eq. [51]), while only valid at a single sinusoidal frequency, permits any linear element to be included in the circuit. This can include conditions at very high breathing frequencies where the effect of inertance on airflows and pressures becomes important. At normal breathing frequencies, however, the airway tree can be modeled as a combination of resistances and compliances. Otis et al. pointed out that any bifurcation within such a tree might be modeled using a single frequency dependent effective resistance and compliance for each daughter branch. We therefore expressed Eq. [51] explicitly for any RC circuit in Eq. [52] and in doing so describe pendelluft volume at *any* bifurcation of the airway tree during normal breathing. The resulting equations were used to find the analytical limits of relative pendelluft for a range of circuits and conditions (Eqs [53]- [55]).

In the next section we describe the methodology of the second aim in this chapter: to use an in-silico model of bronchoconstriction to illustrate both local and global effects of pendelluft on airflow and ventilation in a realistic context and non-sinusoidal input.

Numerical Simulation of Pendelluft was used to illustrate the pendelluft that can occur during heterogeneous bronchoconstriction observed in asthma. An integrative model of bronchoconstriction including an airway tree with 12 generations was used to simulate a pattern of the self-organized airway constriction that emerges dur**i**ng an asthma attack, as previously described in detail [1]. Briefly, our computational model involves solving the distribution of airflow, pressure, and volume within a bronchial tree with 12 generations of branching using Euler's method for numerical integration and time steps of 10 milliseconds. The dynamics of airflow

distribution in the model are determined by the input at the central airway opening and recursive equations for the network of resistances connected to the compliances of the terminal units. Airway radii were updated breath-by-breath according to the relative airway smooth muscle tone (T_r) and the airway's peak transmural pressure during the breathing cycle taking into account the transmural pressure and parenchymal forces. The simulation using T_r = 90%, a mechanical ventilation profile with a volume-controlled mode, constant inspiratory flow, a tidal volume of 650 ml, positive end expiratory pressure (PEEP) of 5 cmH_2O, 12 breaths per minute for a period of 600 breaths resulted in the emergence a typical steady state pattern of heterogeneous airway constriction (Fig. 2) [1]. This pattern of bronchoconstriction within the airway tree is consistent with the emergence of ventilation defects (regions of gas trapping or very poor ventilation) in asthma [107]. The fraction of closed or hypoventilated terminal units receiving less that 15% of the average ventilation was 16.7%, indicating substantial ventilation defects. We used that pattern of heterogeneous airway constriction including the 8191 airways of the model, and simulated the airflows in all of the airways of the model over a complete breathing cycle. These airflows were used to calculate the pendelluft flow and volumes using equations [44] and [45], respectively.

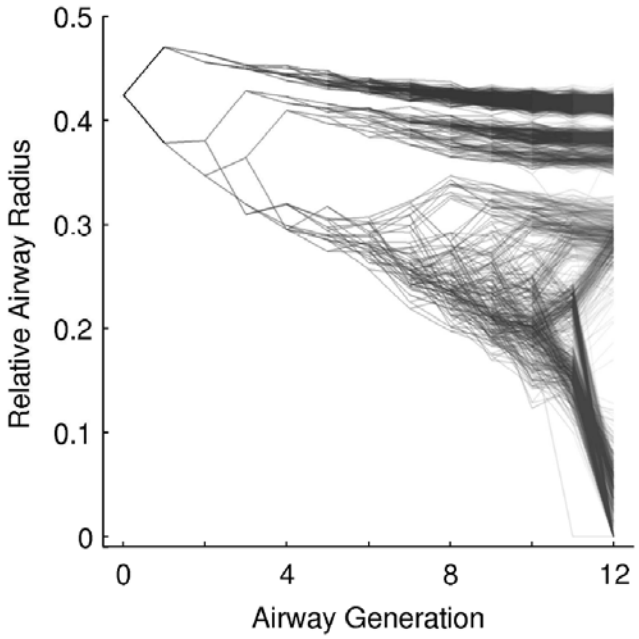

Figure 22: The example of self-organized bronchoconstriction used to explore pendelluft in a realistic context. Note that the constricted airways group together leading to regionally clustered ventilation defects, and that there are substantial differences in constriction among daughter airways. The airways are shown as points and the connectivity among the airways as lines; darker areas illustrate higher local density.

To explore the effect of breathing waveform on pendelluft we used the pattern of airway constriction and applied a sinusoidal breathing pattern. The airflows throughout the tree were used to calculate local and global pendelluft volumes. An example of pendelluft flow at a bifurcation is presented in Figure 26 for both the sinusoid and mechanical ventilation breathing simulations. In addition, the global relative pendelluft volume of the bronchial tree, the maximum and average local relative pendelluft volume at a bifurcation, the average fraction of the breathing cycle a bifurcation exhibited pendelluft flow, and the fraction of the breathing cycle that pendelluft occurred somewhere in the bronchial tree were tabulated. Finally, the frequency dependence of global pendelluft volume in the numerical example was explored using this same steady state solution for the airway diameters.

Results

Theoretical Limits for Pendelluft with sinusoidal airflow and at a single bifurcation were derived from the analytical evaluation of Equation [51]. Despite the five parameters in the physical circuit (two resistances, two compliances, and the frequency) shown in Figure 21C , the pendelluft depends only on three independent parameters τ_1^*, τ_2^*, and κ:

$$\frac{V_{PB}}{V_{in}} = \frac{\left(\tau_1^{*2}+1\right)^{1/2} + \left(\tau_2^{*2}+1\right)^{1/2}\kappa}{\left(\left(\tau_1^* + \tau_2^*\kappa\right)^2 + \left(1+\kappa\right)^2\right)^{1/2}} - 1 \qquad [52]$$

where τ_1^* and τ_2^* are the time constants, nondimensionalized by frequency, $\tau_1^* = \omega\tau_1$, $\tau_1 = R_1C_1$; $\tau_2^* = \omega\tau_2$, $\tau_2 = R_2C_2$; and $\kappa = C_1/C_2$. Importantly, note that τ_1^* and τ_2^* can also be read as the frequency, nondimensionalized by the respective time constants. This function is explored in Figure 23 for $\kappa = 1$. As κ increases from unity, the maximum on the horizontal axis increases and moves to the right.

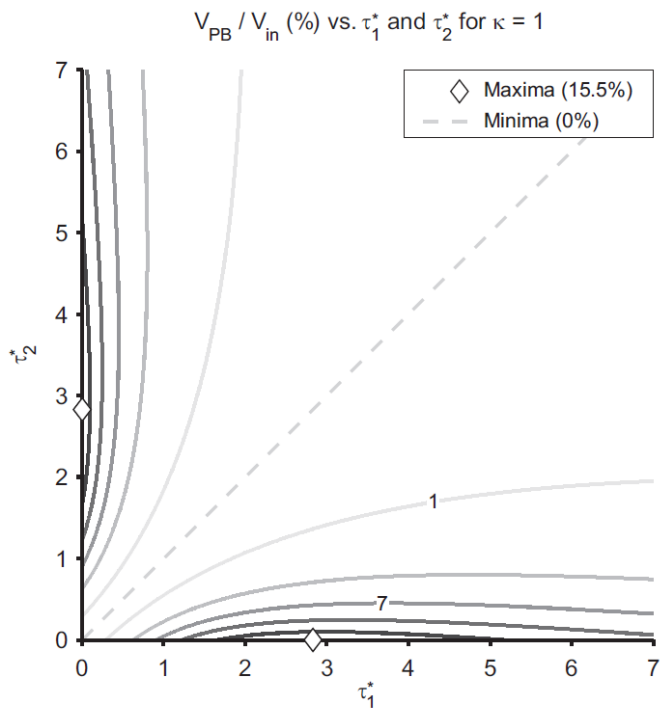

Figure 23: Isocontours marking 3% increments in local relative pendelluft volume as a function of the nondimensional time constants, for κ = 1. The shape of the isocontours shows the steep transition from the maximum at the diamonds (15.5%) to the minimum (zero) on the line of symmetry.

The impedances in Equation [51] can be represented with vectors in the complex plane. The specific elements in the circuit determine the quadrant(s) of this plane that the daughter impedances can be chosen from. A circuit without inertance (i.e. an RC circuit) can only have impedances in the lower right quadrant, while a circuit without compliance effects (i.e. an RL circuit) can only have impedances in the upper right quadrant. When all effects are considered (i.e. a RLC circuit) the daughter impedances can be anywhere in the right half of the complex plane. Equation [51] is maximized when the sum of the impedance magnitudes are large and when the magnitude of the sum of the impedances are small (i.e. the vectors tend to cancel each other out). Geometrical proofs that find the combination of impedance vectors that maximize pendelluft (similar to what is illustrated in Figure 24) result in the following limits for relative pendelluft volume at a bifurcation.

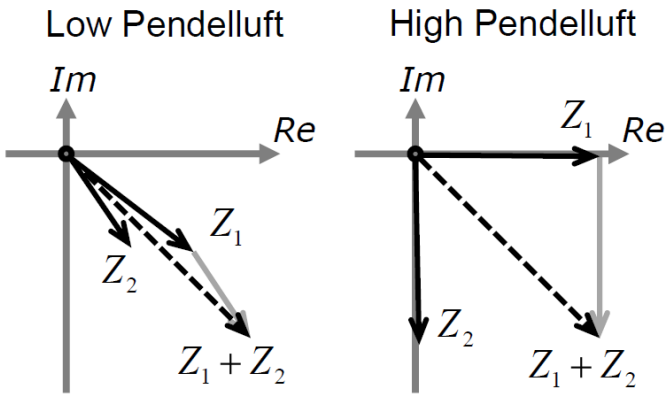

Figure 24: A geometrical description of the combinations of daughter impedances (Z_1 and Z_2) that lead to low and high pendelluft. For RC models of the lung these vectors are confined to the lower right quadrant of the complex plane. Higher pendelluft happens when the impedances diverge and the sum of the daughter magnitudes is considerably larger than the magnitude of their sum.

1. For an RC circuit with a fixed ratio of terminal compliances $\kappa = C_1 / C_2$, where $C_1 \geq C_2$, the maximum pendelluft is achieved when $\tau_1^* = [(\kappa+1)(\kappa+3)]^{1/2}$ and $\tau_2^* = 0$. At this point we have:

$$\max\left|_{\tau_1^*,\tau_2^*}\left(\frac{V_{PB}}{V_{in}}\right) = \sqrt{2\frac{(\kappa+1)}{(\kappa+2)}} - 1\right. \qquad [53]$$

The relationship between the maximum relative pendelluft volume and κ is plotted in Figure 25. The maximum with respect to (τ_1^*, τ_2^*) for any fixed κ occurs when one daughter has vanishingly low compliance or resistance ($\tau_2^* \to 0$). These maxima over (τ_1^*, τ_2^*) increase with κ, and have an asymptotic limit as $\kappa \to \infty$, given by :

$$\max\left|_{\tau_1^*,\tau_2^*,\kappa}\left(\frac{V_{PB}}{V_{in}}\right) = \sqrt{2} - 1 = 0.4142 = 41.4\%\right. \qquad [54]$$

This overall maximum matches Otis et al. [93], and is approached as one daughter resistance decreases and the other daughter compliance increases, such that the magnitudes of the impedances in the two branches are equal (as in Figure 24, High Pendelluft). In this case $\tau_1^* = 1$ ($R_1 = 1/C_2\omega$), $\tau_2^* \to 0$, and $\kappa \to \infty$. If the compliances are equal (κ=1), the maximum over (τ_1^*, τ_2^*) is:

$$\max\left(\frac{V_{PB}}{V_{in}}\right)\Bigg|_{\tau_1^*,\tau_2^*,\kappa=1} = \frac{2\sqrt{3}}{3} - 1 = 0.1548 = 15.5\% \qquad [55]$$

In this case $\tau_2^* \to 0$ and $\tau_1^* = 2\sqrt{2}$. This 15.5% maximum is different than the 5.5% maximum presented in Otis [93], but as the fundamental formulas in that paper are correct, this is most likely a typographical error in [93], rather than an error of substance.

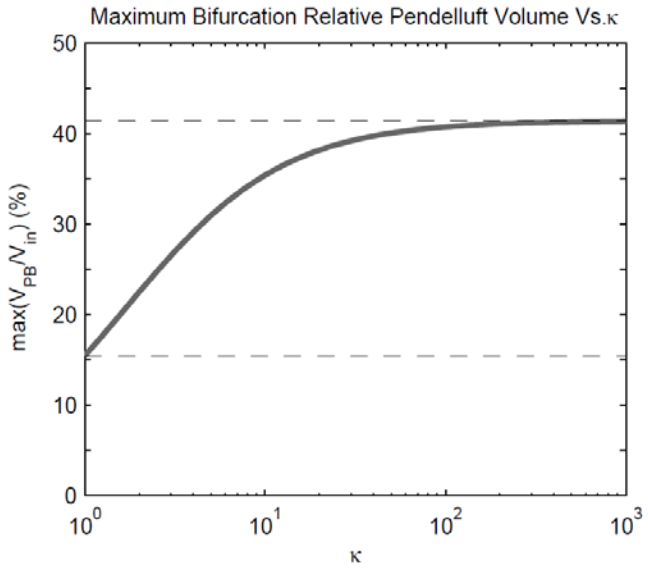

Figure 25: The maximum possible relative pendelluft varies with ratio of the effective compliances of the two daughter pathways. A bifurcation with matched stiffness (κ = 1) gives the lower limit while the upper limit is reached when the path with lower resistance (always subscript 1) has a higher stiffness.

2. RL circuits with resistance and inertance (without capacitance) are not typically relevant for the bronchial tree, but can give insight into the conditions that lead to pendelluft in circuits during high frequency ventilation. These circuits have the same limits as RC circuits presented in the equations and figures above where the dimensionless variables are redefined as $\tau_1^* = R_1 / L_1\omega$, $\tau_2^* = R_2 / L_2\omega$ and $\kappa = L_2 / L_1$. Maxima are found when the daughter with high inertance has low resistance.

3. RLC circuits with resistances, inductances, and capacitances can have unbounded pendelluft. In these cases, pendelluft may oscillate back and forth between the daughters, if the resistances are sufficiently small that the system is underdamped. The characteristic frequency as $R_1 + R_2 \to 0$ is given by $\omega^2 = \left[1/\left(L_1 + L_2\right)\right] * \left[\left(C_1 + C_2\right)/\left(C_1 C_2\right)\right]$ (series inductance, series capacitance).

The limits presented above apply, like the results in the Otis paper, only to pressure or flow-driven inputs at a single frequency. For other waveforms, the pendelluft volume may exceed these values. For example, consider a circuit comprising vanishing resistance in one branch, and unbounded compliance in the other (the case above, for which relative pendelluft may reach 41% if driven at the appropriate single frequency). Driving this with a step change in pressure would instantaneously fill the compliance with the tidal volume followed by the discharge of the compliance through the resistor. During the instantaneous filling no volume is passed through the resistive branch. Subsequently, if an exponential pressure drop matching the pressure inside the

compliance is applied to the parent, the capacitance will discharge entirely through the parallel resistance. Reversing the input pressure would reverse the process. Here the normalized tidal volumes for the compliance daughter, resistance daughter, and the whole circuit are 2, 1 and 1, respectively. Based on equation [47], this yields a relative pendelluft volume of 200%. In contrast, we will shortly show that other non-sinusoidal flows such as the one used in the mechanical ventilation simulation can lead to *lower* pendelluft than a sinusoidal flow at the same frequency.

An Illustrative Example of Pendelluft in the Bronchial Tree was explored using numerical simulations. Both sinusoidal and mechanical ventilation profiles were applied to a simulation of self-organized bronchoconstriction in an airway tree. Pendelluft flow was observed in both the sinusoidal and mechanical profiles at bifurcations within poorly ventilated regions of the lung (Figure 26). Note that the originally constant flow inhalation profile applied to the airway tree during mechanical ventilation is changed to the input ventilation profile of the bifurcation by the frequency dependent dynamics of the airway tree. Table I shows metrics of pendelluft for the two simulations.

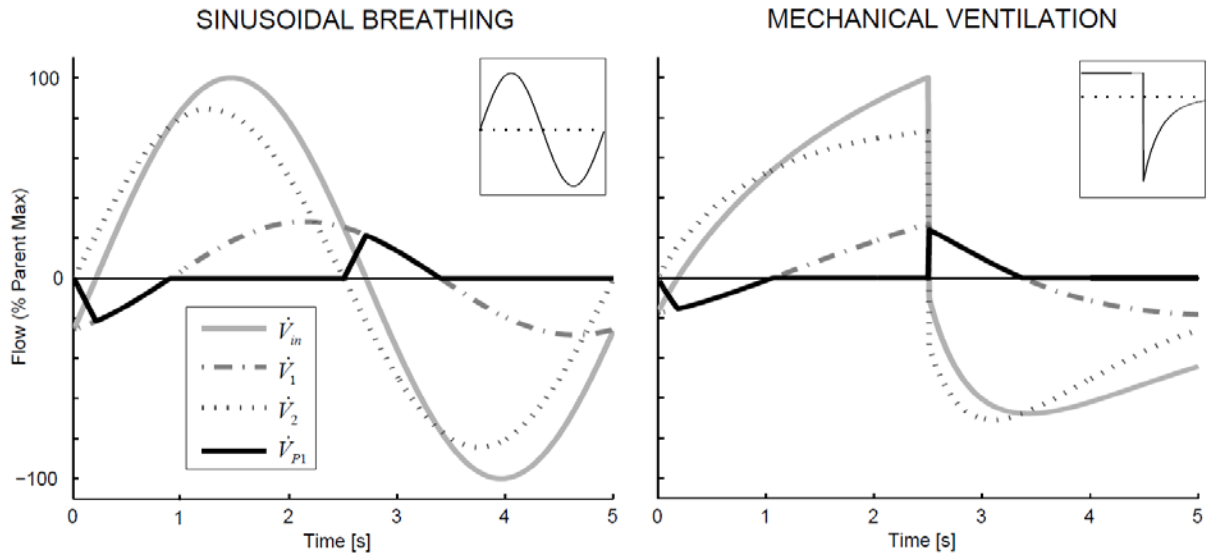

Figure 26: Example of flows at the bifurcation with the highest pendelluft volume (both are at generation 10). The flow profile into the airway tree is shown in the inset pictogram. The flows within the daughters sum to the parent flow. Pendelluft flow begins and ends when one of the flows crosses zero and changes sign.

Table I: Pendelluft simulation results for the two simulations.

	Sinusoidal Ventilation	Mechanical Ventilation
Global Relative Pendelluft Volume (% V_T)	1.57	0.13
Maximum Local Relative Pendelluft Volume (% V_{in})	12.67	13.45
Average Local Relative Pendelluft Volume (% V_{in})	0.25	0.10
Average Fraction of Breathing Cycle in Local Pendelluft (% Total)	3.12	1.80
Fraction of Breathing Cycle With Any Pendelluft (% Total)	78.8	100

Figure 27 shows the distribution of ventilation, relative pendelluft, and aggregate pendelluft volumes throughout the bronchial tree for the sinusoidal and ventilator waveforms. The distribution at each generation of the tree is visualized with a number of boxes matching the number of airways at that generation. The color profile along a vertical line from the top to the bottom represents theoretical streamtubes that go from the most central airway generation of the model to the terminal airways like a bundle of virtual paths. The top panels in Figure 27 show the ventilation pattern during steady state bronchoconstriction for each waveform as a percent of the ventilation the airway would experience in a perfectly symmetric tree (% Uniform V_{in}). Using this normalization allows us to see the smaller volumes in the higher generations. The dark regions indicate poorly ventilated regions that are similar for the two ventilation profiles. The middle panels show the magnitude of relative pendelluft volume at each bifurcation. Observe that regions of high relative pendelluft volume (yellow and red lines) are almost always within the ventilation defects in the top panels. This is where substantial differences in constriction between neighboring pathways exist (Figure 22). Also, there was pendelluft in more central airways for sinusoidal waveform (dark red areas) but not for mechanical ventilation. The lower panels show the distribution and buildup of aggregate pendelluft volume (% Uniform V_{in}). These panels illustrate how pendelluft generated at a bifurcation is redirected to better ventilated regions within the ventilation defect.

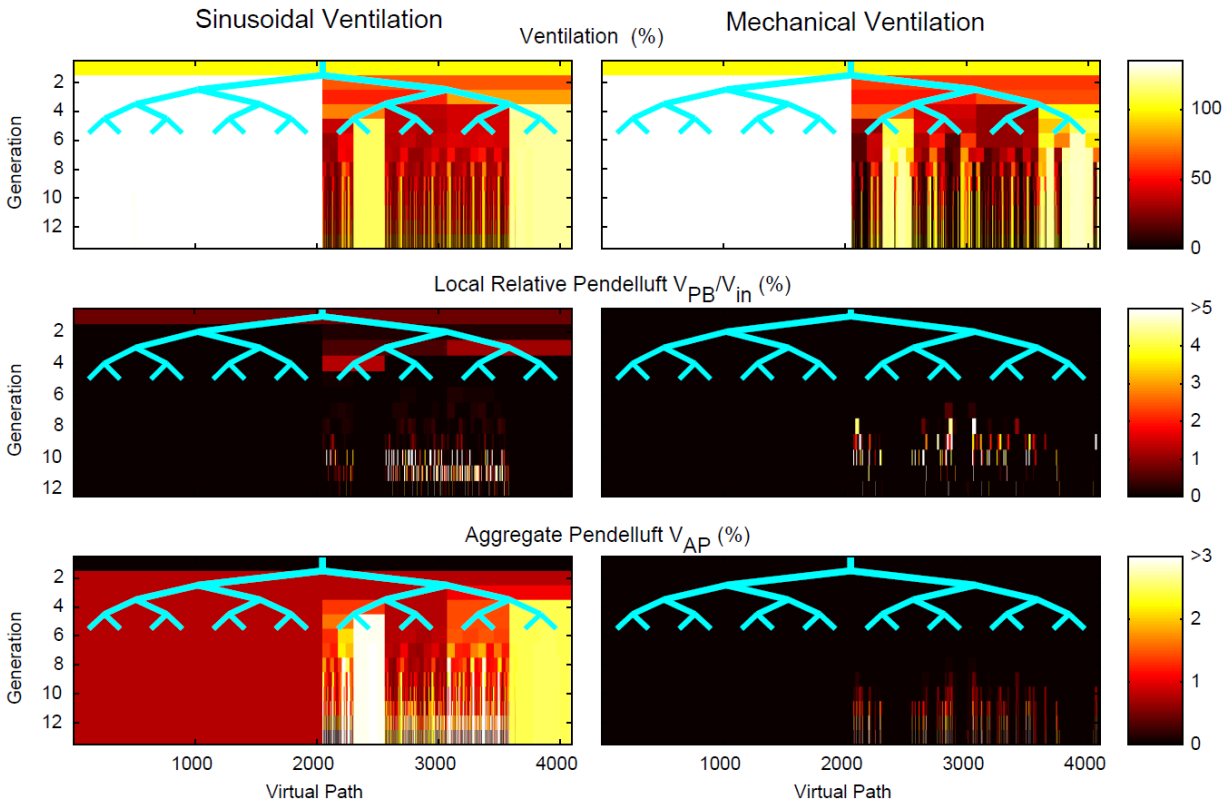

Figure 27: (*Top*) The bronchoconstricted ventilation pattern with darkly colored regions of reduced ventilation as a percent Uniform V_{in}. (*Middle*) High relative pendelluft emerging within ventilation defects is shown with bright colors. (*Bottom*) The regional aggregate pendelluft volume illustrating the diversion to better ventilated regions as a percent Uniform V_{in}.

The frequency dependence of global pendelluft volume in the bronchial tree as a function of the frequency of the driving signal is shown in Figure 28. The maximum total global pendelluft volume for a single frequency sinusoid was 1.75% of the input volume (V_T) at 0.02 Hz. Gas inertia becomes important above about 10 Hz, and creates the second peak with a maximum of 1% at 400 Hz.

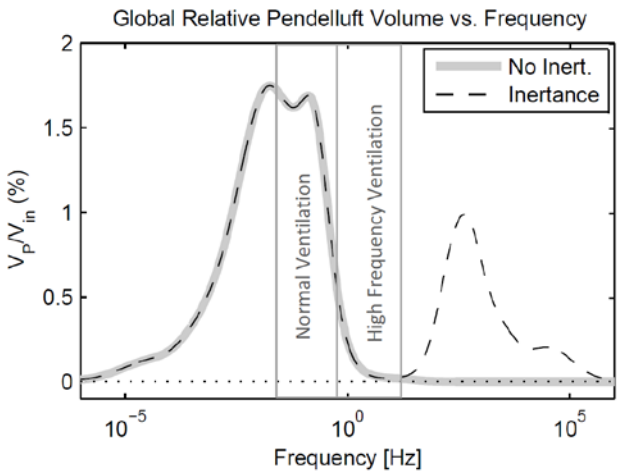

Figure 28: Frequency dependence of global pendelluft volume in a bronchial tree for the example of heterogeneous bronchoconstriction showing the effect of sinusoidal input at different frequencies. Both models of the tree that exclude (No Inert.) or include (Inertance) the effects of the air mass are shown. The physiologically relevant ranges for normal and high frequency ventilation are indicated with vertical gray lines.

Discussion

The Key Findings in this chapter can be separated into analytical and numerical results. In the first portion of this chapter we clarified the definition of pendelluft and generalized this definition to include non-sinusoidal flows as well as to a multigenerational tree. This allowed us to explore local pendelluft at bifurcations, aggregate pendelluft volume that builds up over the bronchial tree, and the global pendelluft volume over the entire tree. We then used analytical tools to identify the limits of pendelluft at a bifurcation for a range of airway models. For a conventional resistance and compliance model of the airway tree driven by a single frequency sinusoid, we found that the limits of possible pendelluft depend on the ratio of compliances of the daughter pathways. When these compliances were equal, the maximum possible pendelluft volume was 15.5% of the bifurcation's tidal volume. (As noted in Results, this is different from the 5.5% presented in Otis [93], which is most likely a typographical error). When these compliances are dissimilar, the maximum pendelluft for a sinusoidal breathing pattern rises to 41%. The difference in the upper limit of pendelluft between the two conditions suggests that pendelluft may be higher in diseases causing heterogeneous changes in compliance such as emphysema. When the effects of inertance are also considered, it is theoretically possible to have any amount of pendelluft. We also introduced a non-sinusoidal waveform that could result in pendelluft volumes that were twice the tidal volume of the bifurcation, even without inertive effects.

In the second portion of this chapter an illustrative example of pendelluft in the bronchial tree was explored using numerical simulations. Both sinusoid and typical mechanical ventilation pjrofiles were applied to an instance of self-organized bronchoconstriction in an airway tree. The main quantitative findings were: 1) a small amount of pendelluft occurs at bifurcations in a realistic model of bronchoconstriction, 2) local pendelluft can be as high as 13% relative to tidal volume flowing through the parent airway and is most commonly found in poorly ventilated regions of the lung due to the increased heterogeneity between parallel pathways (Figure 22) that occurs within ventilation defects during bronchoconstriction [107], and 3) pendelluft volume created at any given bifurcation level is distributed to the better ventilated distal regions.

Lastly, we characterized the frequency dependence of pendelluft in the example and found two separate regions where global pendelluft emerged: the first region happens at lower frequencies and is driven by heterogeneous resistance and compliance. The maximum for this type of pendelluft was less than 2% of the tidal volume and occurs at near normal breathing frequencies. Above 10 Hz a second mode of pendelluft emerges for models that include inertance. The maximum for this kind of pendelluft was 1% of the tidal volume and emerged at frequencies much larger than those used for high frequency ventilation.

Sinusoidal input resulted in greater pendelluft than mechanical ventilation (Figure 27, middle row). The particular frequency chosen for the simulations (12 breaths/min) may have also contributed to higher pendelluft with the sinusoidal waveform since the frequency dependence of global pendelluft volume (Figure 28) showed a maximum near 12 breaths/min. Pendelluft occurred somewhere in the tree during 78.8% (sinusoidal input) or 100% (mechanical ventilation) of the breathing cycle despite its small overall magnitude.

The Contribution of Pendelluft to Overall Gas Transport depends on its magnitude and the composition of the added pendelluft volume. In the bronchoconstriction example, the magnitude of the global pendelluft volume was less than 2% relative to the tidal volume that passed through the central airways. To determine the gas composition of pendelluft flow throughout the airway tree would require modeling the gas transport through the actual volume of the airways for dynamic flow conditions. For example, the gas composition of pendelluft flow at one point of the airway tree could be fresh gas that would have otherwise ended up in the anatomical deadspace, or it could be gas coming from neighboring alveolar units. The small magnitude of the pendelluft volume suggests that even if it were fresh gas, it is unlikely to be an important phenomenon for overall gas exchange. On the other hand, pendelluft that occurs at bifurcations within ventilation

defects (Figure 27) may be important for gas exchange if it could for example increase oxygen delivery in hypoventilated terminal units.

Comparisons With Experimental Studies are limited because it is challenging to experimentally approximate the flow patterns throughout the bronchial tree; our example of bronchoconstriction in asthma clearly showed the complexity of local pendelluft at the distal bifurcations of the bronchial tree and its propagation throughout the generations of the tree. However, comparison with experimental data focusing on the larger airways and proximal bifurcations is possible. Shinozuka et al. [95] measured pendelluft at the carina in an animal model of flail chest. They measured the magnitude of pendelluft volume transferred between the two lungs to be less than 2% of the tidal volume. In flail chest we expect the collapsed lung to be both stiffer (as the chest wall is no longer supporting the lung) and have higher resistance (due to reduced size of the lung). Pendelluft is highest when the stiffer lung has lower resistance, and the findings of a small local pendelluft volume at the carina in flail chest are consistent with the results presented here.

In another experimental study of Pendelluft in dogs with flail chest Harada et. al. found pendelluft volumes exchanged by one of the daughters to be as high as 12.5% of the total volume passing through that branch [94]. This is similar in magnitude to the maximum relative pendelluft observed in the simulations at low frequency (12.6% and 13.5%). It should be noted that Harada et al. defined pendelluft volume as the total, rather than excess, volume passing through the daughter airways when the flows between two connected segments of the lung are in opposing direction. This is potentially confounding, insofar as anything beyond twice the minimum of the absolute values of flow in the daughter branches is passed to or from the parent airway [103].

In a mechanical model of the respiratory system, High et al. (3) found that the largest pendelluft was 275% of the tidal volume when the model was driven with a high frequency, resistances were low, inertances were high, and the compliances were very different. The analytical results for RLC circuit limits presented here match the 'cross-over frequency' at which the highest pendelluft was observed.

Clear asynchronies in parallel filling were apparent when an excised dog lung was driven at high frequencies by Lehr et al. (the 'Disco Lung') [108]. One interpretation of these results rests on the idea of wave propagation, where the gas inertance is coupled to local compliance, resulting in a type of pendelluft closer to underdamped high frequency RLC circuits. These phenomena nevertheless

conform to our general description within the context of inertance dominated branches, with the resulting spatial patterns reflecting the structure of the tree at the segmental or subsegmental bronchial level. Amini and Kaczka included impedances, gas compression and airway wall distention in a computational model of the bronchial tree and found frequency-dependent asynchrony among acinar flows [102] indicating that pendelluft was present.

The pendelluft explored in this chapter does not consider pendelluft that may emerge as the consequence of an unevenly distributed plural pressure. There is recent evidence supporting that this latter form of pendelluft may emerge during mechanical ventilation in the presence of spontaneous effort [98]. Similarly, the beating heart can create local pressure differences that result in pendelluft [106]. In addition, non-linear phenomenon such as recruitment and derecruitment of alveoli and airways can also lead to pressure differences throughout the lung that may lead to pendelluft. For example, the sudden opening of an alveolus will most likely demand air from both parallel pathways (i.e. pendelluft) as well as the serial path from the mouth. While the balance of these volumes might be determined from the mechanical properties of the airway network, these non-linear sources of pendelluft are not characterized by the present chapter.

Limitations of the simulation are related to the model simplifications. The model that we used for our simulation example includes a bronchial tree based on generation 4 to 16 of Weibel's morphometric data for airway length and diameter. It is possible that the 4 more proximal airway generations could influence the pendelluft at certain frequencies and waveforms, but this remains quantitatively unknown. In addition, we have shown analytically (Figure 25) that heterogeneous compliances can nearly triple the relative pendelluft. However, the challenge for numerical simulations is that the results depend on the interplay between the pattern of bronchoconstriction in the airway tree and the pattern of heterogeneity in compliance of the terminal units. For example, a tree could theoretically have a heterogeneity in resistances that spatially matches the heterogeneity in compliances, leading to a uniform distribution of time constants, and little pendelluft.

The diameters and lengths of the airways were derived from an integrative simulation of bronchoconstriction that has been demonstrated to generate ventilation defects similar to those observed in Positron Emission Tomography imaging [1]. It can be assumed that the patterns of clustered constriction of airways that cause the ventilation defects are a reasonable approximation of airway behavior in humans. However, asymmetry in branching of airway within the bronchial tree was not included in that model and may be an additional source of pendelluft volume. Also, the

waveform of the input affects the pattern of bronchoconstriction that emerges in that model due to difference in flow and pressure distributions throughout the airway tree. In order to compare different waveforms under identical conditions, the diameters were fixed for that numerical simulation.

Tissue resistance or tissue hysteresivity, such as that described by the constant phase model [109], was not considered in the numerical simulations. The inclusion of tissue behavior using spatially homogeneous or heterogeneous parameters or impedances would likely increase or decrease pendelluft to some degree depending on the resulting differences in impedances at airway bifurcations. Unfortunately, experimental measurements of hysteresivity are affected by heterogeneity [110] so that estimates of its contribution to pendelluft would rely on assumptions. However, it should be noted that any impedance that can be described for a fixed frequency with a real and complex part can be used in Equation [51] for a single frequency sinusoid.

The presented analysis assumed that the airway walls are rigid and that they do not expand and store additional gas volume. This neglects the notion introduced by Mead of the shunt-capacitance of the airways [111], where the compliance of the airway can become important at high frequencies when the peripheral resistance is high. During high frequency ventilation this effect may improve $C0_2$ elimination in certain circumstances by causing a kind of serial pendelluft [112] As this effect is not modeled in the simulation, it is unclear how neglecting the airway compliance might influence pendelluft, particularly at higher frequencies. Also, it should be noted that the frequency used in high frequency ventilation (up to 900 BPM or 15 Hz [113]), did not create significant inertial pendelluft in the simulation (Figure 28).

In Summary, we generalized the concept of relative pendelluft volume introduced by Otis et al. [93] to include general flow patterns and the entire bronchial tree. We quantified the limits of pendelluft volume at a single bifurcation. Using a numerical example of bronchoconstriction we illustrated that small magnitude pendelluft can emerge in asthma and that pendelluft depends on the breathing profile. While the overall magnitude of pendelluft was small in the example we explored, it was concentrated in poorly ventilated regions of the lung. This preferential site of pendelluft may contribute to local gas exchange, irreversible mixing [105], and aerosol deposition patterns in poorly ventilated regions of the lung.

Grants

Research reported in this chapter was supported by National Heart, Lung, and Blood Institute of the National Institutes of Health under award number R01HL087281.

Disclosures

There are no conflicts of interests to disclose for any of the authors for the present chapter.

Conclusion

Overview

This objective of this thesis was to understand "The Impact of Pathological Ventilation on Aerosol Deposition" and to explore "Imaging, Insight and Interventions" related to this topic. In the first chapter we presented techniques that are critical in determining where in the anatomy the aerosol deposited from a PET-CT image. In the second chapter we introduced a theoretical framework that integrates four measureable and distinct sources of variability in specific deposition among parallel peripheral regions of the lung. We measure these values using PET-CT measurements of aerosol deposition and ventilation in a group of bronchoconstricted asthmatic subjects. In the third chapter of this thesis we investigated whether changing the carrier gas from air to He-O_2 helped homogenize the deposition aerosol. In chapter 4 we used a combination of analytical and numerical tools to evaluate whether or not pendelluft flows emerge in asthma, a mechanism that can have consequences on the aerosol therapy. In this concluding chapter we review the key findings of each of these chapters.

Where Does the Aerosol Go in Asthma?

During an asthma exacerbation, some airways constrict while others dilate leading to differences in ventilation throughout the lung [1, 2]. Asthma exacerbations are often treated with inhaled bronchodilators. What is the terminal destination within the lung of such treatments? What is the effect of the uneven ventilation in determining this? These questions led to the aim of Chapter I in this thesis **to measure the relationship between heterogeneous deposition and ventilation in asthma using PET-CT.**

Chapter I presented a novel methodological approach to evaluate images of aerosol deposition taken with PET-CT cameras. Traditionally, Black-or-White [BW] Regions of Interest [ROIs] are created to cover Anatomical Regions [ARs] segmented from the high-resolution CT. Such ROIs don't usually consider blurring effects due to limited spatial resolution or breathing motion, and do not consider uncertainty in the AR position within the PET image. The new methodology presented in Chapter I [Grayscale] addresses these issues, allows estimates of aerosol deposition within ARs, and expresses the deposition in terms of Tissue Dosing (in the lung periphery) and Inner Surface Concentration (in the larger airways).

Imaging data included a PET deposition image acquired during breathing and two CT scans were acquired during breath holds at different lung volumes. The lungs were segmented into anatomically consistent ARs to allow unbiased comparisons across subjects and across lobes. The

Grayscale method involves defining Voxel Influence Matrices [VIMs] to consider how average activity within each AR influences the measured activity within each voxel. The BW and Grayscale methods were used to analyze aerosol deposition in 14 bronchoconstricted asthmatics.

Grayscale resulted in a closer description of the PET image than BW ($P<0.0001$) and exposed a seven-fold underestimation in measures of specific deposition. The average Tissue Dosing was $2.11x10^{-6}$ Total Lung Dose/mg. The average Inner Surface Concentration was $45x10^{-6}$ Total Lung Dose/mm^2, with the left lower lobe having a lower ISC than lobes of the right lung ($P<0.05$). There was a strong lobar heterogeneity in these measures (COV = 0.3). The Grayscale approach is an improvement over the BW approach and provides a closer description of the PET image. It can be used to characterize heterogeneous concentrations throughout the lung and may be important in translational research and in the evaluation of aerosol delivery systems.

Four main improvements of the proposed methodology over standard methods are presented Chapter I. First, anatomically consistent lobar airways are defined to allow unbiased comparisons between lobes and subjects. Second, subject movement, breathing motion, limited PET resolution, the contribution of small airways and registration inaccuracies are accounted for in the estimation of regional anatomical deposition. Third, the more detailed airway tree imaged at TLC is used to interpret deposition imaged at lower lung volumes. Fourth, specific deposition values were correctly normalized by the airways true volume instead of the conventional ROI volume thus avoiding gross underestimations of central airways specific activity. It was demonstrated that the standard Black or White ROI method substantially underestimated the specific deposition of aerosol in central airways. In contrast, the Grayscale method described the PET image more accurately, correctly assigning deposition to the volume of the AR, and yielded estimates of deposition terms such as tissue dose, TD, and inner surface concentration, ISC. These pharmacologically relevant terms could be important in translational research as well as in evaluation of novel aerosol delivery systems. More generally, the notion of voxel influence matrices, VIMs, represents a paradigm shift in the analysis of radio-tracer localization within the anatomy that could have applications in other imaging modalities.

The work presented in Chapter I allowed us to estimate the activity within anatomical regions in new ways that were only possible with several HRCTs and the novel methods introduced in this thesis. Future work could seek to extend the understanding that is learned from these rich (and expensive) data sets to other imaging modalities in which multiple HRCTs are not possible, practical, or feasible. For example, by stretching VIMs of individual subjects to a common lung bounding hypercube and averaging, a stochastic representation of the VIM emerges[114]. These

stochastic VIMs now describe the *likely* influence of a given AR on each voxel. These stochastic VIMs can be registered to radionuclear images (e.g. PET, SPECT, and scintigraphy) and used to evaluate the deposition and concentration within each of the ARs in pharmacologically relevant terms. In addition, traditional approaches to defining central, intermediate and peripheral regions for scintigraphy images can be augmented by such stochastic VIMs to draw these boundaries that are derived from the average anatomy[114].

What Causes Heterogeneous Aerosol Deposition in Bronchoconstricted Asthmatics?

Variability in peripheral aerosol deposition among lobes, sublobes, or any set of peripheral lung regions, can be traced to four distinct factors: 1) differences in regional ventilation, 2) differences in how the aerosol and air distribute between branches in the series of bifurcations along the pathway feeding the region 3) variability in the amount of the aerosol that escapes the series of airways along that pathway, and 4) variability in the amount of aerosol that reaches the periphery and is not exhaled. The aim of the second chapter of this thesis was **to understand the sources of heterogeneous aerosol deposition in bronchoconstricted asthmatic subjects.**

The PET-CT imaging study introduced in Chapter I of 14 bronchoconstricted asthmatic subjects showed that peripheral aerosol deposition was highly variable among subjects and lobes. The aim of Chapter II was to identify and quantify factors responsible for this variability.

A theoretical framework was formulated to integrate four factors affecting aerosol deposition. These factors were quantified in 12 of the subjects using PET-CT measurements of relative specific deposition sD^*, relative specific ventilation sV^* (measured with dynamic PET or estimated as change in expansion between two static HRCTs), average lobar expansion F_{VOL}, and breathing frequency measured during aerosol inhalation f_N.

We found that the fraction of the variance of sD^* explained by sV^* (0.38), by bifurcation effects (0.38), and by differences in deposition along feeding airways (0.31) were similar in magnitude. We could not directly estimate the contribution of aerosol that was exhaled. Differences in expansion did not explain any fraction of the variability in sD^* among lobes. The dependence of sD^* on sV^* was high in subjects breathing with low f_N , but weakened among those breathing faster. Finally, sD^*/sV^* showed positive dependence on F_{VOL} among low f_N subjects while the dependence was negative among high f_N subjects.

The theoretical framework allowed us to analyze experimentally measured aerosol deposition imaging data. The mechanisms behind the identified effects of f_N and F_{VOL} on aerosol deposition need further study and may have important implications for aerosol therapy in subjects with heterogeneous ventilation.

The theoretical framework and experimental measurements presented in Chapter II may provide physiologically appropriate boundary conditions for numerical CFD models of aerosol deposition in bronchoconstricted asthmatic subjects. In that chapter, we demonstrated that, in the presence of bronchoconstriction, measurements of ventilation that consider dynamic effects need to be considered; the change in lung volume between 2 static HRCT images did not correlate with the deposition pattern among all lobes of all subjects. This observation should help guide future CFD models. In addition, the parsing of the experimental results in terms of the four sources of variability provides a common language to compare CFD and experimental data with; we can now do more than to compare the patterns predicted by numerical models with experimental results, and we can look at whether the *mechanisms* that lead to variability are similar (or different). Thus, the theoretical and experimental work presented in Chapter II both guides and complements future CFD work.

Does He-O_2 Homogenize the Deposition?

During severe bronchoconstriction bronchodilators are sometimes administered in a mixture of 80% helium and 20% oxygen (He-O_2) in an effort reduce the resistance in the central airways and improve delivery of the aerosol to the lung periphery [3-6]. Does He-O_2 lead to a more homogeneous deposition in bronchoconstricted asthmatics? Answering this is the objective of the third chapter of this thesis **to determine if He-O_2 homogenizes the deposition in bronchoconstricted asthmatics.**

The first aim of Chapter III was to obtain detailed 3D data sets of anatomical, physiological and aerosol deposition in bronchoconstricted subjects with asthma that could be used in personalized CFD models. A second aim was to compare results obtained in a group of 10 bronchoconstricted asthmatic subjects inhaling the aerosol while breathing He-O_2 with those from a previously studied similar group of 12 subjects breathing air (Chapter II).

PET-CT imaging was used to generate 3D anatomic maps and lobar values of relative specific deposition sD^*, relative specific ventilation sV^*, lung expansion F_{vol}, along with the breathing frequency during inhalation f_N. The imaging data was analyzed to estimate factors affecting the lobar distribution of sD^* in the He-O_2-group, and these factors were compared to those obtained in the air-group.

We found that the distributions of sD^* and sV^* observed among the air and He-O_2 groups were not statistically different. Although there was a large inter-subject variability in the correlation between $sV^*$and sD^* within both groups, among subjects with uneven sD^*, the correlation was on average higher ($p<0.05$) in the He-O_2 group (0.84+/-0.8) compared with the air-

group (0.55+/-0.28). Higher f_N weakened the correlation in the air group but not in the He-O_2 group and the f_N dependent effect of F_{vol} on sD^*/sV^* seen the air group was not seen in the He-O_2-group.

He-O_2 did not make the distributions of sD^* or sV^* more even among lobes in this group. Further study using these personalized data sets as inputs of realistic CFD models could help yield a clearer understanding of when and for whom He-O_2 nebulization is beneficial.

Does Pendelluft Emerge in Asthma?

The heterogeneous mechanical properties or different regions of the lung in asthma could lead to air and aerosol being passed back and forth between regions of the lung in a process known as pendelluft. The final chapter of this thesis used analytical tools and a numerical model of the bronchoconstricted lung **to access whether or not significant pendelluft airflows emerge in asthma.**

Inhomogeneous inflation or deflation of the lungs can cause dynamic pressure differences between regions and lead to interregional airflows known as pendelluft. Chapter IV first used analytical tools to clarify the theoretical limits of pendelluft at a single bifurcation. It then explored the global and regional pendelluft that may occur throughout the bronchial tree in a realistic example using an in-silico model of bronchoconstriction. The theoretical limits of pendelluft volume exchanged at a local bifurcation driven by sinusoidal breathing range from 15.5% to 41.4% depending on the relative stiffness of the subtended regions. When non-sinusoidal flows are considered, pendelluft can be as high as 200% V_{in}. At frequencies greater than 10Hz the inertia of the air in the airways becomes important and the maximal local pendelluft is theoretically unbounded, even with sinusoidal breathing. In a single illustrative numerical simulation of bronchoconstriction with homogenous compliances the overall magnitude of global pendelluft volume was less than 2% of the tidal volume. Despite the small overall magnitude, pendelluft volume exchange was concentrated in poorly ventilated regions of the lung, including local pendelluft at bifurcations of up to 13% V_{in}. This example suggests that pendelluft may be an important phenomena contributing to regional gas exchange, irreversible mixing, and aerosol deposition patterns inside poorly ventilated regions of the lung. The analytical results support the concept that pendelluft may be more prominent in diseases with significant heterogeneity in both resistance and compliance. However, if the small overall magnitude observed in the *in-silico* simulation is representative of the magnitude of pendelluft that that we can expect in asthma, it is unlikely that it will significantly influence the pattern of aerosol deposition.

A Proposed Intervention for Emphysema

Emphysema affects 18 in every 1000 people [115]. It is a seriously disabling and irreversible disease characterized by loss of lung parenchyma and dynamic airway collapse during exhalation. The collapse of airways together with poor parenchymal tethering forces and loss of elastic recoil work together to limit the flow rate from damaged portions of the lung during exhalation. When parts of the lung cannot properly deflate before the next inspiration begins, they become regions of trapped gas that minimally participate in ventilation [116]. Though there are no known cures for emphysema, it is currently treated by supporting the breathing with anticholinergics, bronchodilators, steroid medication, and supplemental oxygen. New therapies such as stem cells [117], molecules targeting lung regenerations, and pnuemoretractive surfactant [118][4] are actively being developed, some with ambitions of actually curing emphysema. While aerosols could deliver these novel therapies directly to the lung parenchyma, in emphysema the distribution of ventilation throughout the lung is highly heterogeneous usually presenting large areas of gas trapping. As a result, current aerosol therapy would exclusively be delivered to ventilating regions of the lung and miss regions most in need of the therapy.

Aerosol inhalation by emphysematous patients may be improved by applying during exhalation at the mouth high frequency (10-15 Hz) positive pressure pulses. This technique is referred to as "Reverse Pressure Pulses" [RPP]. It has been theorized that in RPP, the pressure waves propagate upstream along the expired airflow to collapsed airways. Using an analog model of a compliant airway, it was demonstrated that the flow through a flow-limited Starling Resister could be enhanced using RPP. The pulses spend their energy to temporarily reopen the airways, allowing the trapped air to escape.

We received a $100K CIMIT Innovation grant to explore 2 goals: 1) to design and build a novel, small proof-of-concept RPP delivery device and 2) to use that device in a limited number of studies to evaluate its efficacy for reducing global and regional hyperinflation, and enhancing ventilation distribution. I have built this device, obtained IRB approval, and hope to begin testing in a group of 10 subjects beginning in January of 2015. It is interesting to note that the ventilation waveform that led to 200% pendelluft in RC circuits, is very similar to the waveform used Reverse Pressure Pulse therapy!

A Closing Clinical Note

In closing, despite other sources of heterogeneity, it is clear that poorly ventilated regions of the lung will generally receive a smaller fraction of the inhaled aerosol than better ventilated

regions. Lower deposition might result in paradoxical effects where an inhaled bronchodilator could aggravate the discrepancy between low and high ventilated regions. More importantly, we could imagine that the presence of persistent ventilation defects, long acting therapies such as corticosteroids might be reinforcing ventilation heterogeneity over time. This work suggests that homogenizing the ventilation (e.g. with sufficient doses of bronchodilator to overcome differences in ventilation) prior to administering long acting therapies may help ameliorate some of these effects. In addition, slow deep breathing during delivery of the inhaled therapy likely enhances deposition in the periphery (as we demonstrated in Chapter II) and can reduce differences in ventilation due to bronchoconstriction. New devices, such as the RPP generator, may open up new ways to deliver therapy to poorly ventilating regions. However, no progress can be made until we recognize that pathological ventilation *can* influence the pattern aerosol deposition.

References

1. Venegas JG, Winkler T, Musch G, Melo MFV, Layfield D, Tgavalekos N, Fischman AJ, Callahan RJ, Bellani G, and Harris RS. Self-organized patchiness in asthma as a prelude to catastrophic shifts. *Nature*. 2005;434:777-782.

2. Anafi RC, Beck KC, and Wilson TA. Impedance, gas mixing, and bimodal ventilation in constricted lungs. *Journal of Applied Physiology*. 2003;94:1003-1011.

3. Hollman G, Shen G, Zeng L, Yngsdal-Krenz R, Perloff W, Zimmerman J, and Strauss R. Helium-oxygen improves clinical asthma scores in children with acute bronchiolitis. *Critical care medicine*. 1998;26:1731-1736.

4. Kass JE and Terregino CA. The Effect of Heliox in Acute Severe AsthmaA Randomized Controlled Trial. *CHEST Journal*. 1999;116:296-300.

5. Manthous CA, Hall JB, Caputo M, Walter J, Klocksieben J, Schmidt G, and Wood L. Heliox improves pulsus paradoxus and peak expiratory flow in nonintubated patients with severe asthma. *American journal of respiratory and critical care medicine*. 1995;151:310-314.

6. Kudukis TM, Manthous CA, Schmidt GA, Hall JB, and Wylam ME. Inhaled helium-oxygen revisited: effect of inhaled helium-oxygen during the treatment of status asthmaticus in children. *The Journal of pediatrics*. 1997;130:217.

7. Greenblatt EE, Winkler T, Harris RS, Kelly VJ, Kone M, and Venegas J. Analysis of Three-Dimensional Aerosol Deposition in Pharmacologically Relevant Terms: Beyond Black or White ROIs. *Journal of aerosol medicine and pulmonary drug delivery*. 2014.

8. Greenblatt EE, Butler JP, Venegas JG, and Winkler T. Pendelluft in the bronchial tree. *Journal of Applied Physiology*. 2014:jap. 00466.02014.

9. Smaldone GC. Deposition patterns of nebulized drugs: is the pattern important? *Journal of aerosol medicine*. 1994;7:25-32.

10. Brown JS, Gerrity TR, and Bennett WD. Effect of ventilation distribution on aerosol bolus dispersion and recovery. *Journal of Applied Physiology*. 1998;85:2112-2117.

11. Svartengren M, Philipson K, Linnman L, and Camner P. Airway resistance and deposition of particles in the lung. *Experimental Lung Research*. 1984;7:257-269.

12. Svartengren m, Anderson m, Bylin g, Philipson k, and Camner p. Regional deposition of 3.6 µm particles in subjects with mild to moderately severe asthma. *Journal of aerosol medicine*. 1990;3:197-207.

13. Robertson HT, Glenny RW, Stanford D, McInnes LM, Luchtel DL, and Covert D. High-resolution maps of regional ventilation utilizing inhaled fluorescent microspheres. *Journal of Applied Physiology*. 1997;82:943-953.

14. Miyawaki S, Tawhai MH, Hoffman EA, and Lin CL. Effect of Carrier Gas Properties on Aerosol Distribution in a CT-based Human Airway Numerical Model. *Annals of biomedical engineering*. 2012:1-13.

15. O'Riordan TG and Smaldone GC. Regional deposition and regional ventilation during inhalation of pentamidine. *CHEST Journal*. 1994;105:396-401.

16. Brown JS, Zeman KL, and Bennett WD. Regional deposition of coarse particles and ventilation distribution in healthy subjects and patients with cystic fibrosis. *Journal of aerosol medicine*. 2001;14:443-454.

17. Trajan M, Logus J, Enns E, and Man S. Relationship between regional ventilation and aerosol deposition in tidal breathing. *Am Rev Respir Dis*. 1984;130:64-70.

18. Darquenne C. Aerosol deposition in health and disease. *Journal of aerosol medicine and pulmonary drug delivery*. 2012;25:140-147.

19. Usmani OS, Biddiscombe MF, and Barnes PJ. Regional lung deposition and bronchodilator response as a function of β2-agonist particle size. *American journal of respiratory and critical care medicine*. 2005;172:1497-1504.
20. Swift DL, Carpin JC, and Mitzner W. Pulmonary penetration and deposition of aerosols in different gases: fluid flow effects. *Annals of Occupational Hygiene*. 1982;26:109-117.
21. Habib DM, Garner SS, and Brandeburg S. Effect of Helium-Oxygen on Delivery of Albuterol in a Pediatric, Volume-Cycled, Ventilated Lung Model. *Pharmacotherapy: The Journal of Human Pharmacology and Drug Therapy*. 1999;19:143-149.
22. Fleming J, Conway J, Majoral C, Tossici-Bolt L, Katz I, Caillibotte G, Perchet D, Pichelin M, Muellinger B, Martonen T, Kroneberg P, and Apiou-Sbirlea G. The use of combined single photon emission computed tomography and X-ray computed tomography to assess the fate of inhaled aerosol. *J Aerosol Med Pulm Drug Deliv*. 2011;24:49-60.
23. Esch JL, Spektor DM, and Lippmann M. Effect of lung airway branching pattern and gas composition on particle deposition. II. Experimental studies in human and canine lungs. *Experimental Lung Research*. 1988;14:321-348.
24. Tai L and Lippmann M. Experimental measurements and empirical modelling of the regional deposition of inhaled particles in humans. *The American Industrial Hygiene Association Journal*. 1980;41:399-409.
25. Grgic B, Finlay W, Burnell P, and Heenan A. In vitro intersubject and intrasubject deposition measurements in realistic mouth–throat geometries. *Journal of Aerosol Science*. 2004;35:1025-1040.
26. Berridge MS, Lee Z, and Heald DL. Pulmonary distribution and kinetics of inhaled [11C]triamcinolone acetonide. *J Nucl Med*. 2000;41:1603-1611.
27. Dolovich MB and Bailey DL. Positron Emission Tomography (PET) for Assessing Aerosol Deposition of Orally Inhaled Drug Products. *Journal of aerosol medicine and pulmonary drug delivery*. 2012;25:52-71.
28. Fleming J, Bailey DL, Chan HK, Conway J, Kuehl PJ, Laube BL, and Newman S. Standardization of Techniques for Using Single-Photon Emission Computed Tomography (SPECT) for Aerosol Deposition Assessment of Orally Inhaled Products. *Journal of aerosol medicine and pulmonary drug delivery*. 2012;25:29-51.
29. Fleming J, Nassim M, Hashish A, Bailey A, Conway J, Holgate S, Halson P, Moore E, and Martonen T. Description of pulmonary deposition of radiolabeled aerosol by airway generation using a conceptual three dimensional model of lung morphology. *Journal of aerosol medicine*. 1995;8:341-356.
30. Newman S, Bennett WD, Biddiscombe M, Devadason SG, Dolovich MB, Fleming J, Haeussermann S, Kietzig C, Kuehl PJ, Laube BL, Sommerer K, Taylor G, Usmani OS, and Zeman KL. Standardization of Techniques for Using Planar (2D) Imaging for Aerosol Deposition Assessment of Orally Inhaled Products. *Journal of aerosol medicine and pulmonary drug delivery*. 2012;25 Suppl 1:S10-28.
31. Venegas J, Winkler T, and Harris RS. Lung Physiology and Aerosol Deposition Imaged with Positron Emission Tomography. *Journal of aerosol medicine and pulmonary drug delivery*. 2013;26:1-8.
32. Berker Y, Goedicke A, Kemerink GJ, Aach T, and Schweizer B. Activity quantification combining conjugate-view planar scintigraphies and SPECT/CT data for patient-specific 3-D dosimetry in radionuclide therapy. *European journal of nuclear medicine and molecular imaging*. 2011;38:2173-2185.
33. Rousset OG, Ma Y, and Evans AC. Correction for partial volume effects in PET: principle and validation. *Journal of Nuclear Medicine*. 1998;39:904-911.

34. Fleming JS, Sauret V, Conway JH, Holgate ST, Bailey AG, and Martonen TB. Evaluation of the accuracy and precision of lung aerosol deposition measurements from single-photon emission computed tomography using simulation. *Journal of aerosol medicine*. 2000;13:187-198.
35. Asthma GIf. Global strategy for asthma management and prevention. *NIH Publication*. 2002.
36. Finlay P, Martin A, Katz I, Vecellio L, Caillibotte G, and Venegas J. Aerosol delivery from a vibrating mesh nebulizer with holding chamber in helium/oxygen versus air. *Journal of aerosol medicine and pulmonary drug delivery.* Vol 26. Mary Ann Liebert Inc 140 Huguenot Street, 3rd Fl, New Rochelle, NY 10801 USA; pp. A20-A20, 2013.
37. Finlay WH. *The mechanics of inhaled pharmaceutical aerosols: an introduction*. Academic Press, 2001.
38. Lipkus AH. A proof of the triangle inequality for the Tanimoto distance. *Journal of Mathematical Chemistry*. 1999;26:263-265.
39. G C. Anovarep: compute the Anova for repeated measures and Holm-Sidak test for multiple comparisons if Anova is positive. 2008

40. Lee S, Wolberg G, Chwa KY, and Shin SY. Image metamorphosis with scattered feature constraints. *Visualization and Computer Graphics, IEEE Transactions on*. 1996;2:337-354.
41. Yin Y, Hoffman EA, Ding K, Reinhardt JM, and Lin CL. A cubic B-spline-based hybrid registration of lung CT images for a dynamic airway geometric model with large deformation. *Physics in medicine and biology*. 2010;56:203.
42. Davis MH, Khotanzad A, Flamig DP, and Harms SE. Elastic body Splines: A physics based approach to coordinate transformation in medical image matching. *Computer-Based Medical Systems, 1995., Proceedings of the Eighth IEEE Symposium on*. IEEE; pp. 81-88, 1995.
43. Wörz S and Rohr K. Physics-based elastic registration using non-radial basis functions and including landmark localization uncertainties. *Computer Vision and Image Understanding*. 2008;111:263-274.
44. Rohr K, Stiehl HS, Sprengel R, Buzug TM, Weese J, and Kuhn M. Landmark-based elastic registration using approximating thin-plate splines. *Medical Imaging, IEEE Transactions on*. 2001;20:526-534.
45. Johnson HJ and Christensen GE. Consistent landmark and intensity-based image registration. *Medical Imaging, IEEE Transactions on*. 2002;21:450-461.
46. Castillo R, Castillo E, Guerra R, Johnson VE, McPhail T, Garg AK, and Guerrero T. A framework for evaluation of deformable image registration spatial accuracy using large landmark point sets. *Physics in medicine and biology*. 2009;54:1849.
47. Murphy K, van Ginneken B, Pluim J, Klein S, and Staring M. Semi-automatic reference standard construction for quantitative evaluation of lung CT registration. *Medical Image Computing and Computer-Assisted Intervention–MICCAI 2008*. 2008:1006-1013.
48. Ding K, Bayouth JE, Buatti JM, Christensen GE, and Reinhardt JM. 4DCT-based measurement of changes in pulmonary function following a course of radiation therapy. *Medical physics*. 2010;37:1261.
49. Milic-Emili J, Henderson J, Dolovich M, Trop D, and Kaneko K. Regional distribution of inspired gas in the lung. *J Appl Physiol*. 1966;21:749-759.
50. Venegas J. Linking ventilation heterogeneity and airway hyperresponsiveness in asthma. *Thorax*. 2007;62:653-654.
51. Lee Z and Berridge MS. PET imaging-based evaluation of aerosol drugs and their delivery devices: nasal and pulmonary studies. *Medical Imaging, IEEE Transactions on*. 2002;21:1324-1331.

52. Fleming JS, Sauret V, Conway JH, and Martonen TB. Validation of the conceptual anatomical model of the lung airway. *Journal of aerosol medicine*. 2004;17:260-269.
53. de Vasconcelos TF, Sapoval B, Andrade JS, Grotberg JB, Hu Y, and Filoche M. Particle capture into the lung made simple? *Journal of Applied Physiology*. 2011;110:1664-1673.
54. Chan TL and Lippmann M. Experimental measurements and empirical modelling of the regional deposition of inhaled particles in humans. *The American Industrial Hygiene Association Journal*. 1980;41:399-409.
55. Kim CS, Hu S, DeWitt P, and Gerrity T. Assessment of regional deposition of inhaled particles in human lungs by serial bolus delivery method. *Journal of Applied Physiology*. 1996;81:2203-2213.
56. Darquenne C, van Ertbruggen C, and Prisk GK. Convective flow dominates aerosol delivery to the lung segments. *Journal of Applied Physiology*. 2011;111:48-54.
57. Katz I, Majoral C, Montesantos S, Dubau C, Texereau J, Caillibotte G, and Pichelin M. Modeling The Influence Of The Gas Mixture On Ventilation And Aerosol Deposition Within Pathological Human Lungs: Helium-Oxygen Vs. Air. *Am J Respir Crit Care Med*. 2014;189:A6276.
58. Darquenne C and Prisk GK. Aerosol deposition in the human respiratory tract breathing air and 80: 20 heliox. *Journal of aerosol medicine*. 2004;17:278-285.
59. Wellman TJ, Winkler T, Costa EL, Musch G, Harris RS, Venegas JG, and Melo MFV. Effect of regional lung inflation on ventilation heterogeneity at different length scales during mechanical ventilation of normal sheep lungs. *Journal of Applied Physiology*. 2012;113:947-957.
60. Wongviriyawong C, Harris RS, Greenblatt E, Winkler T, and Venegas JG. Peripheral resistance: a link between global airflow obstruction and regional ventilation distribution. *Journal of Applied Physiology*. 2013;114:504-514.
61. De Backer JW, Vos WG, Vinchurkar SC, Claes R, Drollmann A, Wulfrank D, Parizel PM, Germonpré P, and De Backer W. Validation of computational fluid dynamics in CT-based airway models with SPECT/CT. *Radiology*. 2010;257:854-862.
62. Brant WE and Helms CA. *Fundamentals of diagnostic radiology*. Lippincott Williams & Wilkins, 2012.
63. Netter FH and Colacino S. *Atlas of human anatomy*. Ciba-Geigy Corporation, 1989.
64. Smaldone GC. Physiological and pathological considerations for aerosol deposition: expiration and models of deposition. *Journal of Aerosol Medicine*. 2000;13:387-391.
65. Cartier A, Malo J, Begin P, Sestier M, and Martin R. Time course of the bronchoconstriction induced by inhaled histamine and methacholine. *Journal of Applied Physiology*. 1983;54:821-826.
66. Mannino F, Sposato B, Ricci A, Grasso D, De Clementi F, and Mariotta S. Induction and recovery phases of methacholine-induced bronchoconstriction using FEV1 according to the degree of bronchial hyperresponsiveness. *Lung*. 2001;179:137-145.
67. Anderson M, Svartengren M, Philipson K, and Camner P. Deposition in man of particles inhaled in air or helium-oxygen at different flow rates. *Journal of Aerosol Medicine*. 1990;3:209-216.
68. Peterson JB, Prisk GK, and Darquenne C. Aerosol deposition in the human lung periphery is increased by reduced-density gas breathing. *Journal of aerosol medicine and pulmonary drug delivery*. 2008;21:159-168.
69. Svartengren M, Anderson M, Philipson K, and Camner P. Human lung deposition of particles suspended in air or in helium/oxygen mixture. *Experimental lung research*. 1989;15:575-585.
70. Katz IM, Martin AR, Muller P-A, Terzibachi K, Feng C-H, Caillibotte G, Sandeau J, and Texereau J. The ventilation distribution of helium–oxygen mixtures and the role of inertial losses in the presence of heterogeneous airway obstructions. *Journal of biomechanics*. 2011;44:1137-1143.

71. Greenblatt EE, Winkler T, Harris RS, Kelly VJ, Kone M, Katz I, Martin A, Caillibotte G, and Venegas J. What Causes Uneven Aerosol Deposition in the Bronchoconstricted Lung? A Quantitative Imaging Study. *Journal of aerosol medicine and pulmonary drug delivery*

2014.

72. Sandeau J, Katz I, Fodil R, Louis B, Apiou-Sbirlea G, Caillibotte G, and Isabey D. CFD simulation of particle deposition in a reconstructed human oral extrathoracic airway for air and helium–oxygen mixtures. *Journal of aerosol science*. 2010;41:281-294.

73. Alcoforado L, Brandão S, Rattes C, Brandão D, Lima V, Ferreira Lima G, Fink JB, and Dornelas de Andrade A. Evaluation of lung function and deposition of aerosolized bronchodilators carried by heliox associated with positive expiratory pressure in stable asthmatics: A randomized clinical trial. *Respiratory medicine*. 2013;107:1178-1185.

74. Piva JP, Barreto SSM, Zelmanovitz F, Amantéa S, and Cox P. Heliox versus oxygen for nebulized aerosol therapy in children with lower airway obstruction. *Pediatric Critical Care Medicine*. 2002;3:6-10.

75. Majoral C, Katz I, Fleming J, Conway J, Collier L, Pichelin M, Tossici-Bolt L, and Caillibotte G. Aerosol deposition in asthmatic subjects breathing helium-oxygen vs. air. *European Respiratory Journal*. 2012;40:P2160.

76. Kim IK and Corcoran T. Recent developments in heliox therapy for asthma and bronchiolitis. *Clinical Pediatric Emergency Medicine*. 2009;10:68-74.

77. Kress JP, Noth I, Gehlbach BK, Barman N, Pohlman AS, Miller A, Morgan S, and Hall JB. The utility of albuterol nebulized with heliox during acute asthma exacerbations. *American journal of respiratory and critical care medicine*. 2002;165:1317-1321.

78. Bag R, Bandi V, Fromm Jr RE, and Guntupalli KK. The effect of heliox-driven bronchodilator aerosol therapy on pulmonary function tests in patients with asthma. *Journal of Asthma*. 2002;39:659-665.

79. Sattonnet P, Plaisance P, Vicaut E, Lecourt L, Adnet F, Goldstein P, Bagou G, Marx J, and Ecollan P. The efficacy of helium-oxygen mixture (65%-35%) in acute asthma exacerbations. *Am J Respir Crit Care Med*. 2003;167:A956.

80. Lee DL, Hsu CW, Lee H, Chang HW, and Huang YCT. Beneficial effects of albuterol therapy driven by heliox versus by oxygen in severe asthma exacerbation. *Academic emergency medicine*. 2005;12:820-827.

81. Kim IK, Phrampus E, Venkataraman S, Pitetti R, Saville A, Corcoran T, Gracely E, Funt N, and Thompson A. Helium/oxygen-driven albuterol nebulization in the treatment of children with moderate to severe asthma exacerbations: a randomized, controlled trial. *Pediatrics*. 2005;116:1127-1133.

82. Henderson SO, Acharya P, Kilaghbian T, Perez J, Korn CS, and Chan LS. Use of heliox-driven nebulizer therapy in the treatment of acute asthma. *Annals of emergency medicine*. 1999;33:141-146.

83. Rose JS, Panacek EA, and Miller P. Prospective randomized trial of heliox-driven continuous nebulizers in the treatment of asthma in the emergency department. *The Journal of emergency medicine*. 2002;22:133-137.

84. Rivera ML, Kim TY, Stewart GM, Minasyan L, and Brown L. Albuterol nebulized in heliox in the initial ED treatment of pediatric asthma: a blinded, randomized controlled trial. *The American journal of emergency medicine*. 2006;24:38-42.

85. Dorfman TA, Shipley ER, Burton JH, Jones P, and Mette SA. Inhaled heliox does not benefit ED patients withmoderate to severe asthma. *The American journal of emergency medicine*. 2000;18:495-497.

86. Corcoran T, Dauber J, Chigier N, and Iacono A. Improving drug delivery from medical nebulizers: the effects of increased nebulizer flow rates and reservoirs. *Journal of aerosol medicine*. 2002;15:271-282.
87. O'Callaghan C, White J, Jackson J, Crosby D, Dougill B, and Bland H. The effects of Heliox on the output and particle-size distribution of salbutamol using jet and vibrating mesh nebulizers. *Journal of Aerosol Medicine*. 2007;20:434-444.
88. Hess DR, Acosta FL, Ritz RH, Kacmarek RM, and Camargo CA. The effect of heliox on nebulizer function using a β-agonist bronchodilator. *CHEST Journal*. 1999;115:184-189.
89. Martin AR, Ang A, Katz IM, Häussermann S, Caillibotte G, and Texereau J. An In Vitro Assessment of Aerosol Delivery Through Patient Breathing Circuits Used with Medical Air or a Helium–Oxygen Mixture. *Journal of aerosol medicine and pulmonary drug delivery*. 2011;24:225-234.
90. Finlay WH. Estimating the type of hygroscopic behavior exhibited by aqueous droplets. *Journal of aerosol medicine*. 1998;11:221-229.
91. Javaheri E, Shemirani FM, Pichelin M, Katz IM, Caillibotte G, Vehring R, and Finlay WH. Deposition modeling of hygroscopic saline aerosols in the human respiratory tract: Comparison between air and helium–oxygen as carrier gases. *Journal of Aerosol Science*. 2013;64:81-93.
92. Katz I, Pichelin M, Montesantos S, Majoral C, Martin A, Conway J, Fleming J, Venegas J, Greenblatt E, and Caillibotte G. Using Helium-Oxygen to Improve Regional Deposition of Inhaled Particles: Mechanical Principles. *Journal of aerosol medicine and pulmonary drug delivery*. 2014;27:71-80.
93. Otis A, Mckerrow C, Bartlett R, Mead J, McIlroy M, Selver-Stone N, and Radford Jr E. Mechanical factors in distribution of pulmonary ventilation. *Journal of Applied Physiology*. 1956;8:427.
94. Harada K, Saoyama N, Izumi K, Hamaguchi N, Sasaki M, and Inoue K. Experimental pendulum air in the flail chest. *The Japanese journal of surgery*. 1983;13:219-226.
95. Shinozuka N, Sato J, Kohchi A, Nishino T, and Mizuguchi T. Pendelluft is not the major contributor to respiratory insufficiency in dogs with flail chest: a mathematical analysis. *Journal of Anesthesia*. 1995;9:252-259.
96. Sala H, Fernandez A, Guardia S, González A, and Rodenstein D. Supramaximal flow in asthmatic patients. *European Respiratory Journal*. 2002;19:1003-1007.
97. Vyshedskiy A and Murphy R. Pendelluft in Chronic Obstructive Lung Disease Measured with Lung Sounds. *Pulmonary medicine*. 2012;2012.
98. Yoshida T, Torsani V, Gomes S, De Santis RR, Beraldo MA, Costa EL, Tucci MR, Zin WA, Kavanagh BP, and Amato MB. Spontaneous effort causes occult pendelluft during mechanical ventilation. *American journal of respiratory and critical care medicine*. 2013;188:1420-1427.
99. High K, Ultman J, and Karl S. Mechanically induced pendelluft flow in a model airway bifurcation during high frequency oscillation. *Journal of biomechanical engineering*. 1991;113:342.
100. Kamm R, Stutsky A, and Drazen J. High-frequency ventilation. *Critical reviews in biomedical engineering*. 1984;9:347.
101. Ultman JS, Shaw RG, Fabiano DC, and Cooke KA. Pendelluft and mixing in a single bifurcation lung model during high-frequency oscillation. *Journal of Applied Physiology*. 1988;65:146-155.
102. Amini R and Kaczka DW. Impact of Ventilation Frequency and Parenchymal Stiffness on Flow and Pressure Distribution in a Canine Lung Model. *Annals of biomedical engineering*. 2013;41:2699-2711.
103. Safonoff I and Emmanuel GE. The effect of pendelluft and dead space on nitrogen clearance: mathematical and experimental models and their application to the study of the distribution of ventilation. *Journal of Clinical Investigation*. 1967;46:1683.
104. Lee WJ, Kawahashi M, and Hirahara H. Experimental analysis of pendelluft flow generated by HFOV in a human airway model. *Physiological measurement*. 2006;27:661.

105. Butler JP and Tsuda A. Logistic trajectory maps and aerosol mixing due to asynchronous flow at airway bifurcations. *Respiratory physiology & neurobiology*. 2005;148:195-206.
106. Thurgood J, Dubsky S, Henon Y, Jesudason E, and Fouras A. Heart-Lung Interactions: A Vital Source Of Gas Mixing Within The Lungs. *Am J Respir Crit Care Med*. 2014;189:A6275.
107. Winkler T and Venegas JG. Complex airway behavior and paradoxical responses to bronchoprovocation. *Journal of Applied Physiology*. 2007;103:655-663.
108. Lehr JL, Butler JP, Westerman PA, Zatz SL, and Drazen JM. Photographic measurement of pleural surface motion during lung oscillation. *Journal of Applied Physiology*. 1985;59:623-633.
109. Hantos Z, Daroczy B, Suki B, Nagy S, and Fredberg J. Input impedance and peripheral inhomogeneity of dog lungs. *J Appl Physiol*. 1992;72:168-178.
110. Bates JH. *Lung mechanics: an inverse modeling approach*. Cambridge University Press, 2009.
111. Mead J. Contribution of compliance of airways to frequency-dependent behavior of lungs. *Journal of Applied Physiology*. 1969;26:670-673.
112. Rossing T, Slutsky A, Ingram R, Kamm R, Shapiro A, and Drazen J. CO2 elimination by high-frequency oscillations in dogs--effects of histamine infusion. *Journal of Applied Physiology*. 1982;53:1256-1262.
113. Butler W, Bohn D, Bryan A, and Froese A. Ventilation by high-frequency oscillation in humans. *Anesthesia & Analgesia*. 1980;59:577-584.
114. Greenblatt E, Alcoforado L, De Andrade AD, and Venegas J. Using Average Anatomical Information To Analyze Scintigraphy Images Of Aerosol Deposition. *Am J Respir Crit Care Med*. 2014;189:A4978.
115. Adams PE, Martinez ME, Vickerie JL, and Kirzinger WK. Summary health statistics for the US population: National Health Interview Survey, 2010. *Vital and health statistics. Series 10, Data from the National Health Survey*. 2011:1-117.
116. Zamel N, Hogg J, and Gelb A. Mechanisms of maximal expiratory flow limitation in clinically unsuspected emphysema and obstruction of the peripheral airways. *The American review of respiratory disease*. 1976;113:337-345.
117. Ishizawa K, Kubo H, Yamada M, Kobayashi S, Numasaki M, Ueda S, Suzuki T, and Sasaki H. Bone marrow-derived cells contribute to lung regeneration after elastase-induced pulmonary emphysema. *FEBS letters*. 2004;556:249-252.
118. Suki B, Lutchen KR, and Ingenito EP. On the progressive nature of emphysema: roles of proteases, inflammation, and mechanical forces. *American journal of respiratory and critical care medicine*. 2003;168:516-521.